

Wissenschaftliche Mitteilungen

**aus dem
Institut für Meteorologie der Universität Leipzig**



ISBN 978-3-9814401-1-9

**Meteorologische Arbeiten (XVIII) und
Jahresbericht 2012 des Instituts für
Meteorologie der Universität Leipzig**

Hrsg.: Armin Raabe

Leipzig 2013

Band 51

Wissenschaftliche Mitteilungen aus dem Institut für Meteorologie der Universität Leipzig Bd. 51

Wissenschaftliche Mitteilungen aus dem Institut für Meteorologie der Universität Leipzig, Band 51

M. Brückner, A. Macke, M. Wendisch Cloud Retrieval using Ship-based Spectral Transmissivity Measurements1
C. Jacobi, M. Ern Gravity waves and vertical shear of zonal wind in the summer mesosphere-lower thermosphere11
T. Fytterer, C. Arras, C. Jacobi Terdiurnal signatures in midlatitude sporadic E layers occurrence rates25
A. Raabe, M. Bender, J. Wickert Final results of the DFG founded project: Development of a tomographic water vapour sounding system based on GNSS data39
M. Schäfer, E. Bierwirth, A. Ehrlich, F. Heyner and M. Wendisch Retrieval of Cirrus Optical Thickness and Assessment of Crystal Shape from Ground-Based Imaging Spectrometry53
M. Wilsdorf, A. Bischoff, A. Ziemann and A. Raabe Studies of sound attenuation depending of the meteorological environmental conditions67
M. Wendisch, D. Rosenow, et al. ACRIDICON-Zugspitze field campaign81
Jahresbericht des Instituts für Meteorologie 201283

Wissenschaftliche Mitteilungen aus dem Institut für Meteorologie der Universität Leipzig Bd. 51

Cloud Retrieval using Ship-based Spectral Transmissivity Measurements

M. Brückner^a, A. Macke^a, M. Wendisch^b

^a*Leibniz Institute for Tropospheric Research (TROPOS), Permoserstr. 15, 04318 Leipzig,
Germany*

^b*Leipzig Institute for Meteorology (LIM), University of Leipzig, Stephanstr. 3, 04103
Leipzig, Germany*

Summary. Within the scope of the OCEANET-Project (autonomous measurement platforms for energy and material exchange between ocean and atmosphere) on board of the research vessel (RV) Polarstern clouds have been investigated over the Atlantic Ocean under different atmospheric conditions and climate zones by active and passive remote sensing. An existing measurement platform, including lidar, microwave radiometer, all sky camera and broadband radiation sensors, has been extended by spectral radiation measurements with the COmpact RAdiation measurements System (CORAS). CORAS measures spectral downward radiances and irradiances in the visible to near-infrared wavelength region. The data were corrected to consider the movements of the ship and with it the misalignment of the sensor plane from earth's horizon. Using observed and modeled spectral transmitted radiances cloud properties such as cloud optical thickness (τ) and effective radius (r_{eff}) were retrieved. The vertical cloud structure with limitations for thick clouds is obtained from lidar and microwave radiometer measurements. The all sky camera provides information on the horizontal cloud variability. Cloud optical thickness and effective radius, will be retrieved by using a plane parallel radiative transfer model and a new spectral 3D retrieval method.

Zusammenfassung. Im Rahmen des OCEANET-Projektes (autonome Messplattform zur Bestimmung des Material- und Energieaustauschs zwischen Ozean und Atmosphäre) wurden Wolken über dem Atlantischen Ozean unter verschiedenen atmosphärischen Bedingungen und Klimazonen an Bord des Forschungsschiffes Polarstern durch aktive und passive Fernerkundung untersucht. Die bereits existierende Messplattform (Lidar, Mikrowellenradiometer, Vollhimmels-Kamera, Standardmeteorologie und breitbandige Strahlung) wurde mit einem Spektrometersystem (CORAS) erweitert. CORAS misst spektrale abwärtsgerichtete Irradianzen und Radianzen im Wellenlängenbereich 350-2000 nm. Die Daten werden in Bezug auf die Schiffsbewegungen, sowie die horizontale Abweichung der Sensorebene lagekorrigiert. Mit beobachteten und modellierten Radianzen werden Wolkenparameter, wie die optische Dicke (τ) und der effektive Radius (r_{eff}) abgeleitet. Die vertikale Wolkenstruktur (mit Beschränkungen für dicke Wolken) wird von Lidar- und Mikrowellenradiometer erhalten. Die

Vollhimmelskamera liefert Informationen über die horizontale Wolkenverteilung. Die Wolkenparameter werden mit einem plan-parallelem Strahlungstransfermodell in Kombination mit einem neuen spektralen 3D Retrieval abgeleitet.

Introduction

To understand the interaction between clouds and solar radiation within the climate system ground-based observations with high temporal and spatial resolution are required. In the framework of the OCEANET-project (autonomous measurement platform for material and energy exchange between ocean and atmosphere) a measurement container was developed which is planned to be operated on freight and research vessels (Macke et al., 2010). The container combines several measurement techniques of passive and active remote sensing applications to provide data of different cloud scenes over ocean in three climate zones in both the northern and southern hemispheres. The measurements reported here were performed during the Atlantic transfers aboard the German research vessel (RV) Polarstern. Spectral radiation measurements were used to obtain cloud microphysical properties such as cloud optical thickness τ and effective radius r_{eff} applying a new spectral 3D cloud retrieval method. Furthermore, the results of different radiative transfer models will be compared with the observations.

Instrumentation

The OCEANET-Atmosphere container consists of several instruments. A microwave radiometer HATPRO (Humidity and Temperature PROfiler) provides atmospheric vertical profiles of temperature, humidity and liquid water path (Zoll, 2012). A full sky imager (Kalisch and Macke, 2008; Kalisch, 2011) determines the cloud coverage and cloud type. For daytime every 15 seconds a picture is taken. Pyrano- and Pyrgoemeter were used to obtain the solar and terrestrial downward broadband irradiance (Macke et al., 2010). A multi wavelength Raman lidar Polly^{XT} (Althausen et al., 2009; Kanitz et al., 2011) measured vertical profiles of the particle extinction coefficient and aerosol microphysical properties. Spectral radiation measurements were performed with the CCompact RAdiation measurement System (CORAS). This instrument consists of two optical inlets to measure downward spectral irradiance and radiance; both inlets were mounted on the roof of the container. The inlets are connected via optical fibers to a system of spectrometers. For measurements in the visible (VIS: 350-1000 nm) and near infrared (NIR) spectral range (950-2200 nm). The spectral resolution is 2-3 nm in VIS and 15 nm in NIR. The OCEANET-container was located on the helicopter deck of RV Polarstern.

Spectral Cloud Retrieval

For ground-based observations the information of transmitted radiances through the atmosphere is used to retrieve cloud optical properties. But the relationship between spectral radiance and optical thickness and effective radius is not as straightforward with transmissivity. On the one hand there is no sensitivity to r_{eff} in the visible range and less in the NIR range. However, transmitted radiance first increases with increasing optical thickness to a value of 5 (depending on solar zenith angle) and then decreases to an asymptotic value which leads to an ambiguous retrieval (not shown here).

The use of the spectral information of optical properties could provide more information on optical thickness and effective radius. By finding the best match between pre-calculated and observed radiances cloud properties are retrieved. With the plane-parallel radiative transfer model package libRadtran (Mayer and Kylling, 2005) the transmitted radiance $I_{\lambda, \text{mod}}^{\downarrow}$ at sea level z_0 is calculated. Further observations made on Polarstern (e.g., radiosonde data, temperature, wind field) were used as an additional model input. The radiative transfer calculations were performed for an ocean surface albedo and a liquid water cloud with different values of optical thickness and effective radius. The optical thickness was varied from 1 to 80 at an interval of 1. The effective radius ranges from 1 μm to 25 μm in steps of 1 μm . The calculations were performed over the full wavelength range of CORAS.

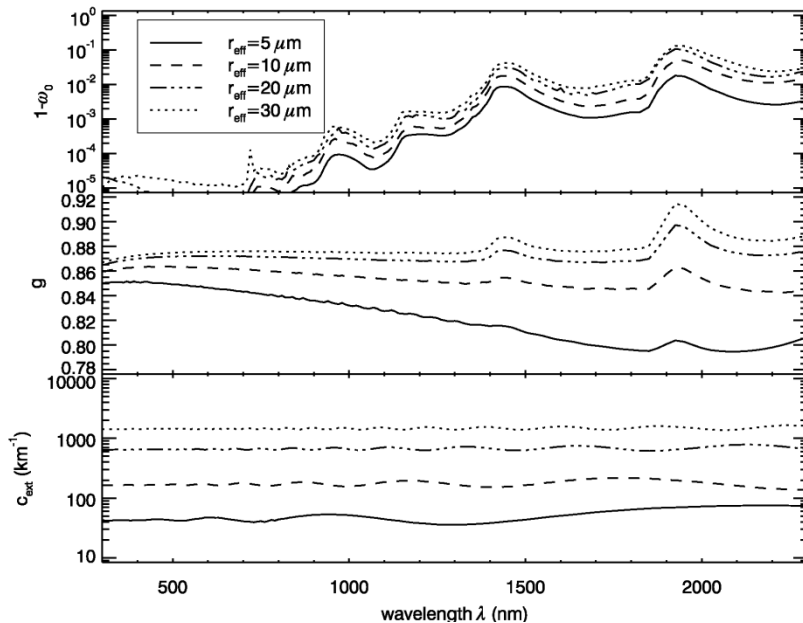


Fig. 1: Coalbedo, asymmetry parameter and extinction coefficient for liquid water droplets from Mie calculations at four different cloud effective radii.

Spectral optical properties of liquid cloud droplets such as single scattering albedo $\tilde{\omega}_0$, extinction coefficient b_{ext} and asymmetry parameter g were calculated for an effective radius ranges from 5 μm to 30 μm in steps of 1 μm using Mie calculations (Mayer and Kylling, 2005) assuming a gamma droplet size distribution. Figure 1 shows the coalbedo ($1 - \tilde{\omega}_0$, measure for absorption), asymmetry parameter (first moment of scattering phase function) and the extinction coefficient over the spectral range at four values of effective radius. As cloud droplet absorption increases, the coalbedo increases with increasing effective radius and varies over several orders of magnitude. According to increased forward scattering with droplet size also asymmetry parameter and extinction coefficient increases. The spectral shapes of these parameters have a direct influence on transmissivity (McBride et al., 2011). With these parameters an input optical property file was modeled for each value of effective radius across the wavelength range.

Furthermore, the spectral transmissivity at sea level z_0 was calculated:

$$T_{\lambda,\text{mod/obs}}^{\downarrow} = \frac{\pi I_{\lambda,\text{mod/obs}}^{\downarrow}(z_0)}{\mu_0 F_{\lambda}^{\downarrow}(z_{\text{TOA}})} \quad 1)$$

where the indices ‘mod’ refers to the model results and ‘obs’ to the observations. To consider the current position of the sun the cosine of solar zenith angle μ_0 is used along the cruise track and the incoming solar irradiance F_{λ}^{\downarrow} at the top of atmosphere (TOA).

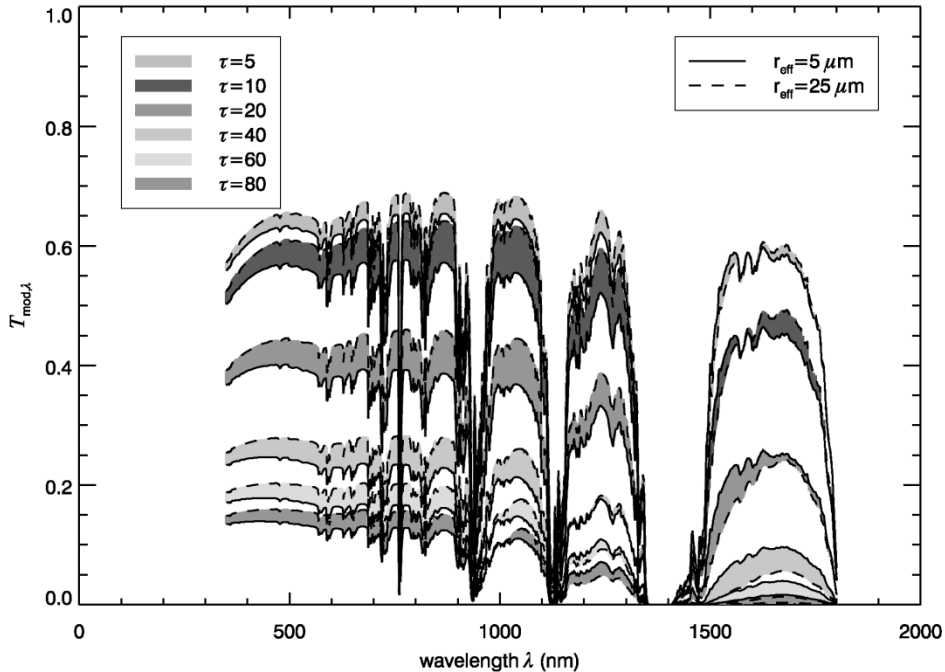


Fig. 2: Modeled spectral transmissivity of a liquid water cloud for different values of effective radius (solid lines for 5 μm , dashed lines for 25 μm) and optical thickness (grey shaded areas) at solar zenith angle of 40° and an ocean surface albedo.

Figure 2 shows the modeled spectral transmissivity for a liquid water cloud with different values of optical thickness and two values of effective radius ($5\mu\text{m}$: solid lines and $25\mu\text{m}$: dashed lines). The shaded areas illustrate constant values of optical thickness. The calculation was performed for a solar zenith angle θ_0 of 40° and an ocean surface albedo. Largest transmissivity occurs at an optical thickness of 5 and decreases with increasing optical thickness. At wavelengths shorter than about 1100 nm the dominant process is scattering. Larger droplets with larger asymmetry parameters results in stronger forward scattering, and thus in larger transmissivity. With increasing effective radius transmissivity decreases because of increasing cloud droplet absorption. The crossover between these opposing effects occurs at wavelength range 1100 nm and 1400 nm depending on the magnitude of cloud droplet absorption. Especially in the NIR range between 1560 nm and 1670 nm the differences between $5\mu\text{m}$ and $25\mu\text{m}$ are largest and results in an enhanced sensitivity to effective radius. Furthermore, absorption bands of different atmospheric gases (O_3 , H_2O and O_2) are represented in the modeled spectral transmissivity.

The new spectral 3D retrieval uses the information of transmissivity or ratios at different wavelengths. These wavelengths have to be chosen outside of bands with strong molecular absorption. By using ratios of transmissivity retrieval errors are reduced. A combination of the ratio of transmissivity at 450 nm to 680 nm $T_{\text{mod},450}/T_{\text{mod},680}$ (dependent on optical thickness), the ratio of transmissivity at 1670 nm to 1560 nm $T_{\text{mod},1670}/T_{\text{mod},1560}$ (dependent on effective radius) and the ratio of transmissivity at 1050 nm to 1250 nm $T_{\text{mod},1050}/T_{\text{mod},1250}$ (mainly dependent on optical thickness and less sensitive to effective radius) provides information on both cloud properties. Figure 3a and 3b shows a 3D look up table for a water cloud with different microphysical properties based on the model results from figure 2. Lines of different effective radius and optical thickness are clearly separated. Furthermore, the retrieval ambiguity is removed. Figure 3b is a zoom into figure 3a for smaller optical thicknesses. Adding the ratio $T_{\text{mod},450}/T_{\text{mod},680}$ provides more sensitivity to optical thickness lower than 5 so that they can be distinguished from larger ones. For smaller optical thickness the proportion of Rayleigh scattering is larger, and thus a typical slope in the VIS range is obvious and provides the information on both microphysical properties. The knee of the surface conforms to the largest values of optical thickness and depends on the solar zenith angle.

To retrieve microphysical properties from observation at time j the best match between the modeled and observed transmissivity is inferred by finding the minimum of a minimum function $f(\tau, r_{\text{eff}})_j$:

$$(\tau_{\text{retrieved}}, r_{\text{eff}_{\text{retrieved}}})_j = \text{MIN}(f(\tau, r_{\text{eff}})_j),$$

with:

$$f(\tau, r_{\text{eff}})_j = \sum_{\lambda=1}^3 (T_{\text{obs}}(\lambda)_j - T_{\text{mod}}(\lambda, \tau, r_{\text{eff}})_j),$$

where

$$\lambda = \frac{450\text{nm}}{680\text{nm}}, \frac{1050\text{nm}}{1250\text{nm}}, \frac{1670\text{nm}}{1560\text{nm}},$$

which is the sum of the difference between observed and all modeled transmissivity at $T_{\text{mod/obs},450}/T_{\text{mod/obs},680}$, the ratio $T_{\text{mod/obs},1670}/T_{\text{mod/obs},1560}$ and the ratio $T_{\text{mod/obs},870}/T_{\text{mod/obs},780}$ for the entire value range of τ and r_{eff} .

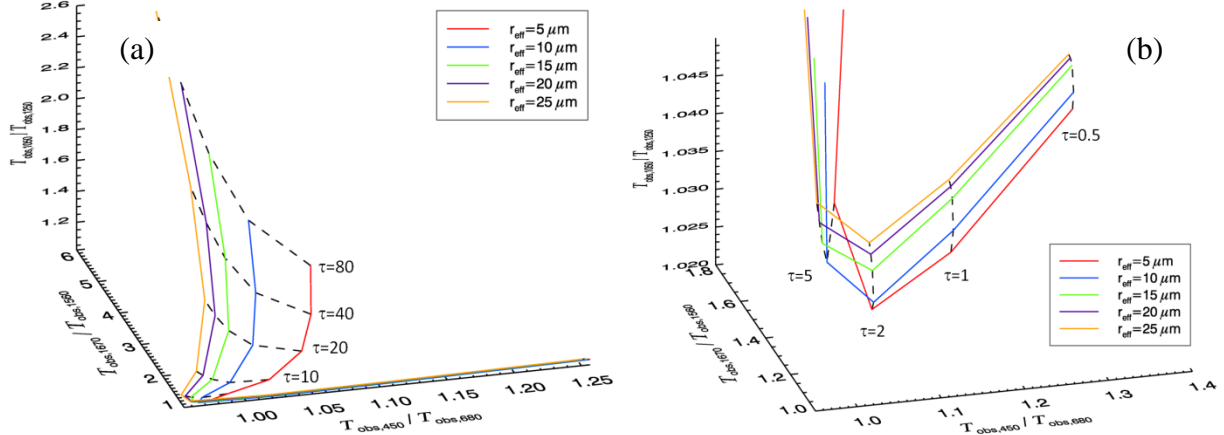


Fig. 3: 3D look up table for water clouds using modeled transmissivity at solar zenith angle of 40° and an ocean surface albedo. Dashed lines represent different values of optical thickness and colored lines different values of effective radius. (a) 3D look up table for optical thickness larger than 5, (b) for optical thickness lower than 5.

Observations over the Atlantic Ocean

During three Atlantic transfer cruises of RV Polarstern (ANT-XXVII/4, ANT-XXVIII/5 and ANT-XXIX/1) data were collected between Cape Town (South Africa) – Bremerhaven (Germany) and Punta Arenas (Chile) – Bremerhaven (Germany), respectively. Cruise plots and details of all three transfers (El Naggar, 2011; Bumke, 2012, Auel, 2013) are shown in figure 4.

The plane-parallel radiative transfer model and Mie calculations applied in this study restricts only to liquid water clouds. For the case study in this paper a time series from ANT-XXVIII/5 on 6 May 2012 from 9:45 to 10:30 UTC was used. During this time, Polarstern was passing the Canary Islands.

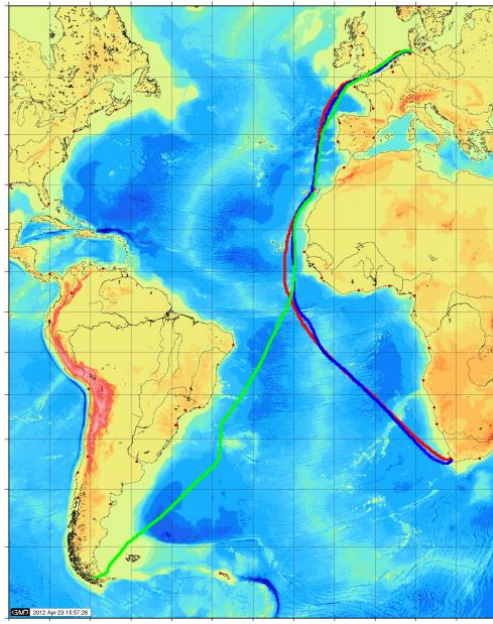


Fig. 4: Cruise plots of ANT-XXVII/4 Cape Town-Bremerhaven April/May 2011 (blue), ANT-XXVIII/5 Punta Arenas-Bremerhaven April/May 2012 (green) and ANT-XXIX/1 Bremerhaven-Cape Town Oct/Nov 2012 (red).

Figure 5 shows the time series of observed ratios of transmissivity. According to (1) $T_{\lambda,\text{obs}}$ were calculated with observed $I_{\lambda,\text{obs}}^{\downarrow}$ from CORAS and the corresponding solar zenith angle $\mu_{0,\text{obs}}$. The shaded time period illustrates a part with thin water clouds and clear sky segments, respectively. Largest values of $T_{\text{obs},450}/T_{\text{obs},680}$ indicates a high ratio of Rayleigh scattering (a) whereas $T_{\text{obs},1670}/T_{\text{obs},1560}$ (b) and $T_{\text{obs},1050}/T_{\text{obs},1250}$ (c) become smallest. Especially sensitivity to r_{eff} decreases and agree with model results. However, both ratios increase when the cloud is getting thicker. The first part is obviously a more inhomogeneous cloud part because of fluctuations in the ratios, whereas the last part is more constant and represents a homogenous cloud scene. The combination of all information of the ratios makes it possible to retrieve τ and r_{eff} from observations.

Figure 6 show the retrievals of optical thickness (a) and effective radius (b) for the case study with the spectral 3D method. Since $T_{\text{obs},1670}/T_{\text{obs},1560}$ has largest sensitivity to r_{eff} it is weighted by normalizing $T_{\text{obs},450}/T_{\text{obs},680}$ and $T_{\text{obs},1050}/T_{\text{obs},1250}$ to $T_{\text{obs},1670}/T_{\text{obs},1560}$. The normalization enhances the sensitivity to effective radius. According to figure 5 three cloud parts are obvious. In the beginning optical thickness increases from 13 to a constant value of around 20 except of some thicker parts. As shown in figure 5b, c effective radius varies from 5 μm to 30 μm because of larger ratios in the NIR wavelength range. The spread of the r_{eff} range represents an inhomogeneous water cloud. The gradual transition to thinner cloud parts is good to see in the optical thickness retrieval, however effective radius decrease rapidly. Mean values of τ and r_{eff} are about 1.5 and 2.3, respectively. As

the cloud is getting thicker both increase again, where the transition is good to see in both retrievals. Inhomogeneities in optical thickness are obvious. Regarding the effective radius the cloud is more homogeneous in comparison to the first part. Due to the weighting of $T_{\text{obs},1670}/T_{\text{obs},1560}$ temporary inhomogeneities can be retrieved.

Furthermore, it is planned to enhance the sensitivity to effective radius with a higher resolution of modeled transmissivity.

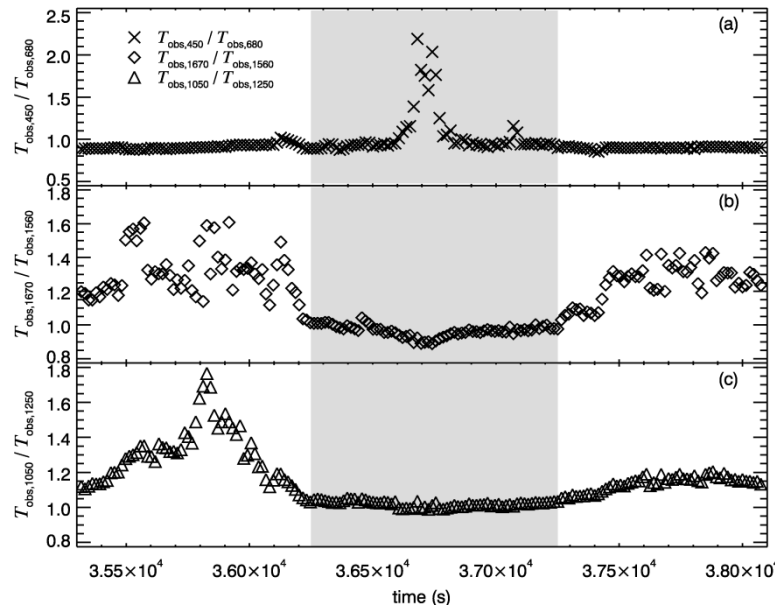


Fig. 5: Time series observations of transmissivity ratios $T_{\text{obs},450}/T_{\text{obs},680}$ (a), $T_{\text{obs},1670}/T_{\text{obs},1560}$ (b) and $T_{\text{obs},1050}/T_{\text{obs},1250}$ (c) on 6 May 2012 from 9:45-10:30 UTC.

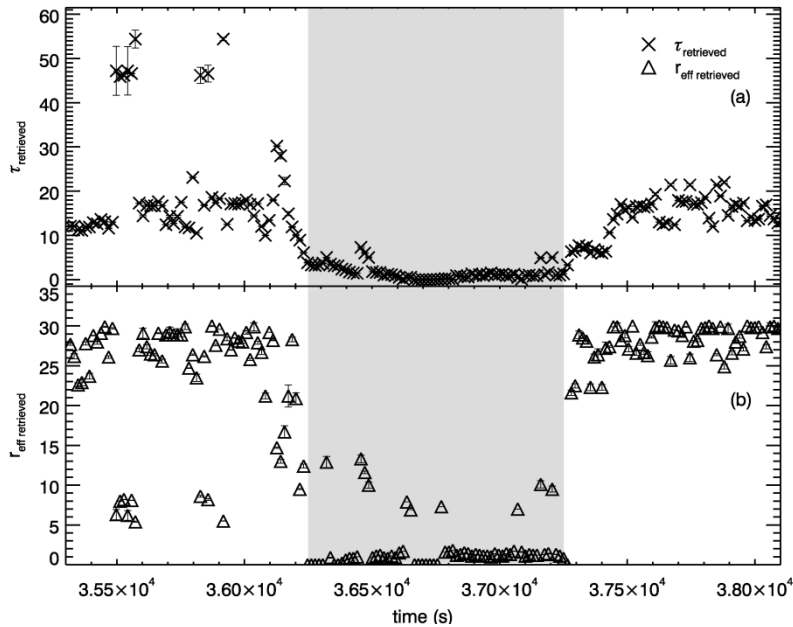


Fig. 6: Time series plots of CORAS retrievals of optical thickness and effective radius on 6 May 2012 from 9:45-10:30 UTC.

Summary and Outlook

This paper introduces a new spectral 3D cloud retrieval to obtain cloud optical thickness and effective radius from ship-based spectral transmissivity measurements. The measurements of spectral radiation were performed in the scope of the OCEANET project during the Atlantic Ocean transfers of RV Polarstern. The spectral information of transmitted radiance is used to obtain the spectral transmissivity at the surface. Several ratios of transmissivity at certain wavelengths (450 nm to 680 nm, 1670 nm to 1560 nm, 1050 nm to 1250 nm) were calculated to retrieve cloud microphysical properties using a minimum function of these three ratios.

It is planned to compare the retrieval results with observations from the microwave radiometer aboard RV Polarstern. Using the retrieved τ and r_{eff} the liquid water path (LWP) is calculated. Furthermore, focus of the research will be to consider different cloud patterns such as broken cloud situations and dusty cloud scenes.

Acknowledgments

The authors thank the scientist and crew from the RV Polarstern and the Alfred Wegener Institute for Polar and Marine Research (AWI) for their permanent support and the opportunity to perform measurements during the Atlantic transfer cruises ANT-XXVII/4, ANT-XXVIII/5 and ANT-XXIX/1.

References

- Althausen, D., Engelmann, R., Baars, H., Heese, B., Ansmann, A., Müller, D., and Komppula, M., 2009: Portable Raman lidar PollyXT for automated profiling of aerosol backscatter, extinction, and depolarization, *J. Atmos. Oceanic Techno.* 26, 2366–2378, doi:10.1175/2009JTECHA1304.1.
- Auel, H., 2013: The Expedition of the Research Vessel "Polarstern" to the Antarctic in 2012 (ANT-XXIX/1), *Reports on Polar and Marine Research*, Vol. 658 (in preparation).
- Bumke, K., 2012: The Expedition of the Research Vessel "Polarstern" to the Antarctic in 2012 (ANT-XXVIII/5), *Reports on Polar and Marine Research*, Vol. 654.
- El Naggar, S., 2011: The Expedition of the Research Vessel "Polarstern" to the Antarctic in 2011 (ANT-XXVII/4), *Reports on Polar and Marine Research*, Vol. 639.
- Kalisch, J. and Macke, A., 2008: Estimation of the total cloud cover with high temporal resolution and parameterization of short-term fluctuations of sea surface insulation, *Meteorol. Z.* 17, 603-611.
- Kalisch, J., 2011: Der Einfluss von Wolken auf den Strahlungsantrieb der Erde, Ph.D. Thesis, Leibniz Institute for Ocean Research IFM-GEOMAR, Kiel.
- Kanitz, T., Seifert, P., Ansmann, A., Engelmann, R., Althausen, D., Cassicia, C., and Rohwer, E.G., 2011: Contrasting the impact of aerosol at northern and southern midlatitudes on heterogeneous ice formation, *Geophys. Res. Lett.* 38, L17802, doi:10.1029/2011GL048532..

- Macke, A., Kalisch, J., Zoll, Y., and Bumke, K., 2010: Radiative effects of the cloudy atmosphere from ground and satellite based observations, EPJ Web of Conferences 9, 83-94.
- Mayer, B. and Kylling, A., 2005: Technical note: The libRadtran software package for radiative transfer calculations – description and example of use, *Atmos. Chem. Phys.* 5, 1855-1877.
- McBride, P.J., Schmidt, K.S., Pilewskie, P., Kittelman, A.S., and Wolfe, D.E., 2011: A Spectral method for retrieving cloud optical thickness and effective radius from surface-based transmittance measurements, *Atmos. Chem. Phys.* 11, 7235–7252.
- Zoll, Y., 2012: Bestimmung des Flüssigwasserpades auf See mit Hilfe der passiven Mikrowellenradiometrie, Ph.D. Thesis, Christian-Albrechts-University of Kiel.

Gravity waves and vertical shear of zonal wind in the summer mesosphere-lower thermosphere

C. Jacobi and M. Ern

Summary

Gravity wave amplitudes and momentum fluxes derived from SABER temperature measurements are analysed together with Collm meteor radar zonal winds. The momentum flux (MF) divergence derived from the SABER temperatures shows a maximum that is found at greater altitudes during solar minimum than during solar maximum. Therefore, the zonal mean wind and wind shear profiles are shifted upwards then, leading to a modulation of the otherwise negative correlation between solar cycle and mesosphere/lower thermosphere winds.

Zusammenfassung

Amplituden von Schwerewellen und zugehörigen Impulsflüsse werden zusammen mit Windmessungen des Meteorradiars Collm analysiert. Die Impulsflussdivergenz, abgeleitet aus SABER-Temperaturprofilen, hat ein Maximum welches im solaren Minimum nach oben verschoben ist. Dadurch werden auch die Vertikalprofile des Zonalwindes und der Windscherung nach oben verschoben, wodurch die ansonsten negative Sonnenfleckenzzyklusabhängigkeit des zonalen Windes in der Mesosphäre/unteren Thermosphäre im solaren Minimum umgekehrt wird.

1 Introduction

The mesosphere-lower thermosphere (MLT) region is characterised by the interaction between gravity waves (GW) and the mean wind. During recent years, there has been considerable interest in the interannual and long-term variability of both mean winds and GW (e.g., Hoffmann et al., 2011; Jacobi et al., 2006, 2011, 2012) in order to detect long-term trends and a possible decadal (solar cycle) variation and to investigate coupling processes between mean winds and GW. While Hoffmann et al. (2011) essentially detected a positive long-term trend in MLT GW, Jacobi et al. (2006, 2011) found a strong solar cycle variation in summer GW proxies and mean winds. However, they also found a more complicated behaviour, so that during solar minimum the otherwise negative solar cycle effect on the mean wind is reversed.

Jacobi et al. (2011, 2012) had used LF winds measured at Collm (reference point is 52°N, 15°E near 90 km). The dataset and analysis procedure is described in Jacobi et al. (2012) for the prevailing wind and in Jacobi et al. (2006) for the GW proxies. Fig. 1 presents a height-time cross-section of GW proxies, being defined here as the squared difference between consecutive half-hourly mean LF winds provided that the reference height between these values does not change. Maximum GW variances are found in summer in the upper mesosphere. The known winter maximum is not visible, which may be due to the short periods (about 1 hr) the LF GW proxy is representative for.

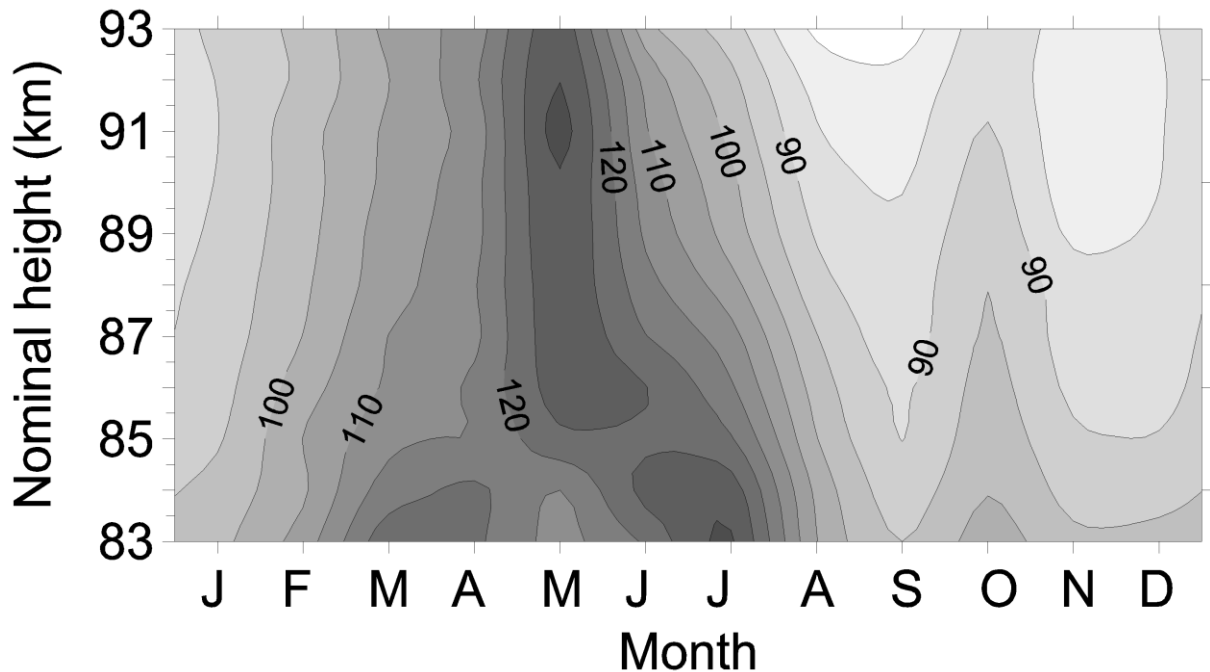


Figure 1: 1984-2007 mean GW variance proxy, calculated from the sum of differences between consecutive half-hourly mean zonal and meridional winds measured by the LF D1 method at Collm.

Generally, the summer circulation is more stable than the winter one, and the interannual variability in summer is smaller than in winter, when planetary waves and stratospheric warmings may lead to significant effects in the MLT circulation on a monthly time scale. During summer, day-to-day variability may be caused by the quasi 2-day wave (e.g., Muller and Nelson, 1978) and a QBO effect on the MLT mean wind. However, while the former should cancel out if longer time intervals of one month or a full season are considered, the latter has been found to be insignificant during summer (Jacobi et al., 1996). Therefore, the analysis of the summer circulation is recommended if primarily GW effects on the MLT mean circulation are to be analysed.

Time series of summer (June–August, hereafter JJA) mean zonal prevailing winds at about 90 km and GW proxies (again, the sum of the squared zonal (U'^2) and meridional (V'^2) half-hourly mean wind deviations are used) at the same altitude are presented in Fig. 2, together with the F10.7 index, i.e. the solar radio flux at 2800 MHz given in sfu ($1 \text{ sfu} = 10^{-22} \text{ Wm}^{-2}\text{Hz}^{-1}$), as a solar activity proxy. Note that the height of 90 km for the winds and GW proxy has been calculated from the measured virtual LF reflection heights using an empirical formula that has been derived from winter vertical tidal phase profiles (Jacobi, 2011), so that there is a possible (and to a certain degree unknown) uncertainty of this value. Fig. 2 is very similar to another one presented by Jacobi et al. (2011, their Fig. 2), but there mean winds not decomposed into prevailing winds and tides have been shown and the sunspot number was presented instead of F10.7. However, the results are similar: there is a clear tendency for increasing GW activity during solar maximum, while the solar cycle effect of the prevailing wind is negative, i.e. there is a tendency for stronger eastward winds in the

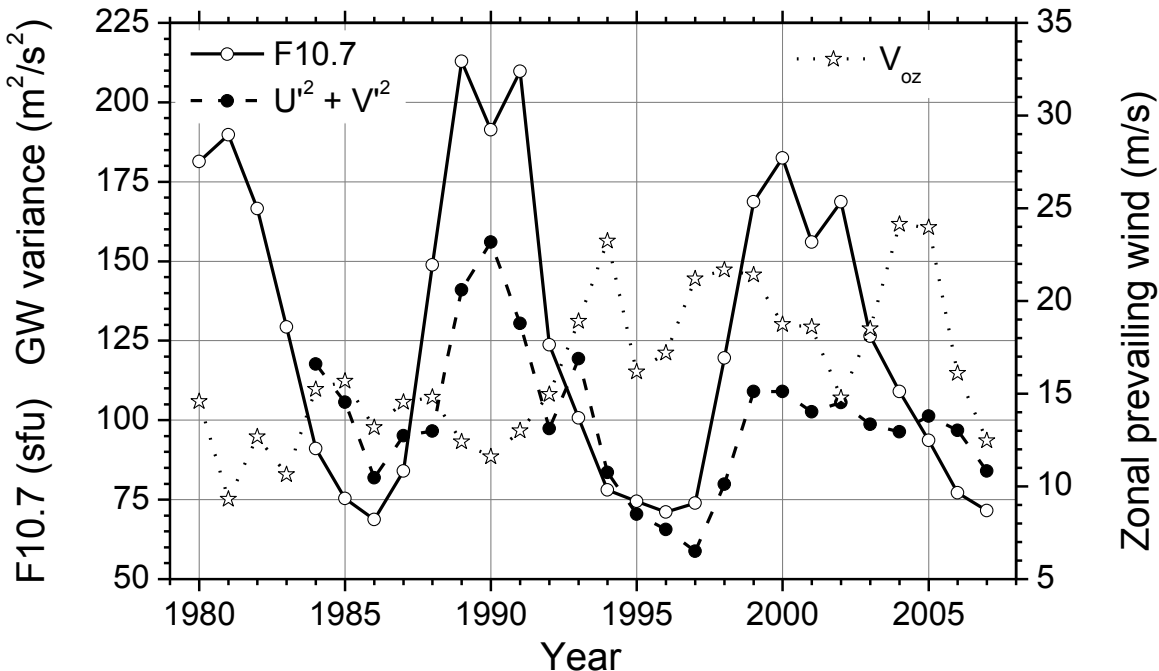


Figure 2: Time series of June-August mean zonal prevailing winds (open stars, Jacobi et al., 2012) and GW variance (solid circles) over Collm at approximately 90 km altitude, as derived from LF wind measurements. F10.7 is added as open circles.

mesosphere during solar maximum. The latter can be explained by stronger mean circulation forcing of the middle atmosphere during solar maximum, leading to a stronger mesospheric wind jet then. This in turn may influence the filter characteristics of the wind jet, leading to larger GW amplitudes if the mean wind is stronger. The described tendencies can also be seen in the Juliusruh, Rügen, medium frequency radar wind data presented by Keuer et al. (2007) and also in Hoffman et al. (2011), but there the focus was laid on long-term trends.

There are, however, deviations from this simple picture, in particular an increase of GW amplitudes shortly after the solar maximum (in 1993 and, less pronounced, in 2005 in Fig. 2), and above all a reversal of the solar cycle–mean wind connection during solar minimum, so that in 1986, 1995/96 and after 2005 the prevailing winds decrease again. To get more insight into this behaviour, data from the extreme solar minimum 2008/2009 are required, as well as winds and GW analyses at different altitudes.

Since the LF measurements have been terminated after 2007, and since their vertical resolution is limited, in this study we apply the Collm VHF meteor radar winds since 2005 together with GW analyses from SABER temperature measurements, and analyse the interannual variability of zonal mean wind and GW amplitudes and momentum fluxes (MF).

2 Measurements and data analysis

Collm meteor radar zonal winds

The SKiYMET meteor radar located at Collm, Germany (51.3°N , 13°E) has been in operation nearly continuously since July 2004, and JJA means of the years 2005-2012 are used here. The radar measurements are described in Jacobi (2011, and references therein). The height interval is divided into six non-overlapping height gates, centred at about 82, 85, 88, 91, 94 and 97 km. Zonal prevailing winds are calculated applying least-squares fitting of mean winds and tidal variations on one month of half-hourly horizontal winds.

GW variances and momentum fluxes can also be derived from fitting 2-hourly mean of these data to the individual radial winds (Hocking, 2005; Placke et al., 2011). However, there is a considerable amount of uncertainty in these analyses, and the height resolution is limited, so that they are only briefly presented here to substantiate the results.

SABER GW analyses

GW amplitudes are calculated from SABER temperature profiles. Before, planetary waves have been removed from the profiles as described in Ern et al. (2011), while tides have been analysed as stationary planetary-scale structure for ascending and descending nodes. Subtracting these average local background temperatures T from the measurements we obtain altitude profiles of residual temperatures that are dominated by GWs. Squared temperature amplitudes \hat{T} have been calculated from the residual temperatures in a 10 km sliding vertical window at 1 km step, and using the data within a window of 10° in latitude (centred at 45°N) and 30° in longitude (centred at 10°E).

Following Ern et al. (2004), GW momentum fluxes MF (i.e. without information on the direction) are calculated via:

$$MF = \frac{\rho}{2} \frac{k}{m} \left(\frac{g}{N} \right)^2 \left(\frac{\hat{T}}{T} \right)^2, \quad (1)$$

where ρ is the density of the background atmosphere, g is the acceleration due to gravity, N is the buoyancy frequency, k the horizontal and m the vertical wavenumber of the GW. The horizontal wavenumber has been obtained from profile pairs along the measurement track (Ern et al., 2004; 2011).

3 Results

In Figs. 3-5 prevailing winds as measured by the Collm radar are presented. JJA mean zonal prevailing winds at different altitudes are shown in Fig. 3 (left panel). The data are updated from Jacobi et al. (2011). In the lower part of the figure, F10.7 solar radio fluxes are added. One can see that, at least for lower altitudes considered, the earlier LF results are reproduced: if the years 2008 and 2009 are disregarded, a negative correlation with the solar flux is indicated, i.e. the mesospheric easterlies are stronger

during solar maximum. Keuer et al. (2007) also reported a negative solar cycle dependence of summer zonal winds. However, in Fig. 3 during the deep solar minimum this behaviour reverses. The interannual variability also confirms measurements presented by Hoffmann et al. (2011, their Fig. 3) at 80-84 km. They also found maximum winds in 2007, weaker winds in 2008/2009, and again stronger ones in 2010.

The mean winds at lower and upper heights are anticorrelated, i.e. if the mean wind is weaker (westward) at 82 km the lower thermosphere maximum is weaker (eastward), too (Figure 4, left panel). This is also seen if the mean winds are compared with the vertical shear of zonal wind (Figure 3, right panel). During years with weaker winds, especially in 2007, the wind shear values at most heights are smaller, too.

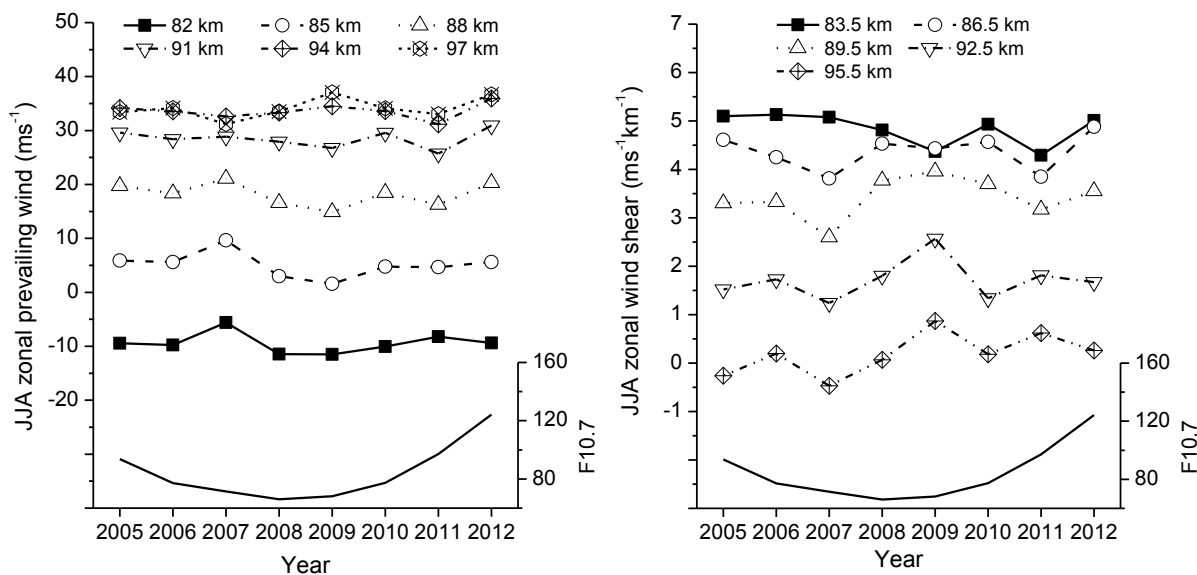


Figure 3: Time series of June-August (JJA) mean zonal prevailing wind (left panel) and vertical shear of zonal wind (right panel) as measured by the Collm meteor radar. Seasonal mean F10.7 values are added in the lower part of the respective panels.

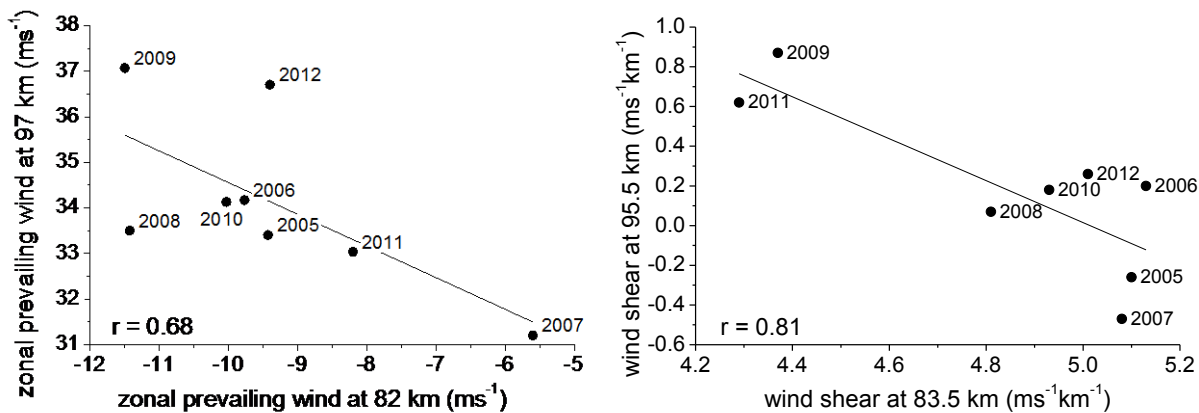


Figure 4: June-August mean zonal prevailing wind (left panel) and vertical shear of zonal wind (right panel) at the uppermost level vs. the respective parameters at the lowermost level as measured by the Collm meteor radar 2005-2012.

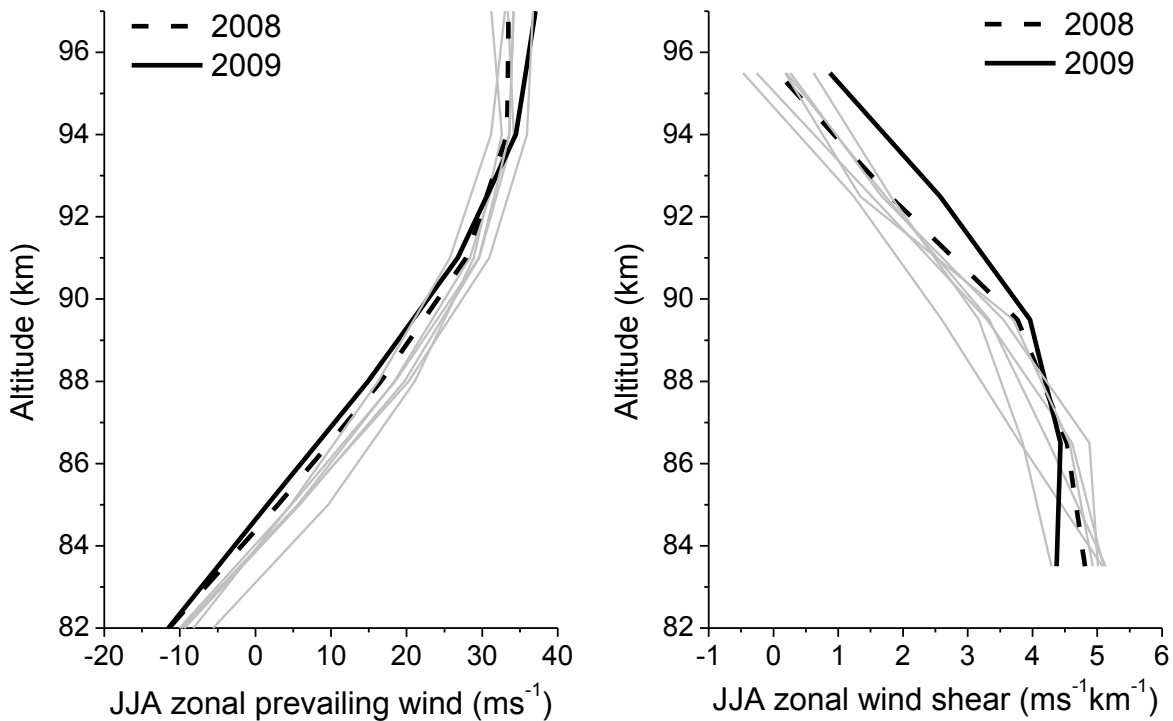


Figure 5: Profiles of June-August mean zonal prevailing wind (left panel) and vertical shear of zonal wind (right panel) as measured by the Collm meteor radar 2005-2012. The years 2008 and 2009 are highlighted.

However, the interannual variability of the wind shear also changes with height, so that wind shear variability at lower and higher altitudes is mainly anticorrelated (Figure 4, right panel). E.g., in 2006 the wind shear in the mesosphere (at 83.5 km) is comparatively strong. If we assume that the shear is due to GW MF divergence this would mean that at greater altitudes MF may have a tendency towards smaller values, which also implies smaller possible MF divergence there. On the contrary, in 2009 the wind shear at lower MLT heights is small, which may be explained by weaker MF divergence. Then at greater altitudes the stronger MF fluxes and MF divergence will lead to stronger wind shear then.

In Figure 5, vertical profiles of zonal mean wind and wind shear are shown. The profiles for the years 2008 and 2009, taken during the extreme solar minimum, are highlighted. They show a tendency of being shifted upward w.r.t. to the other years both in the mean wind and the wind shear profile.

The SABER squared temperature amplitudes at several heights are presented in Fig. 6. The LF variances 2002-2007 are added as solid circles/solid line to show that their interannual variability reasonably well qualitatively reproduces the temperature amplitude variability at about 90-95 km. For comparison, also JJA mean GW wind variances at 91 km as measured by the Collm radar are added (solid circles, dashed line). They also show a similar interannual variability. The SABER amplitudes at 90-100 km show a similar tendency to what has been described for the LF GW proxies already:

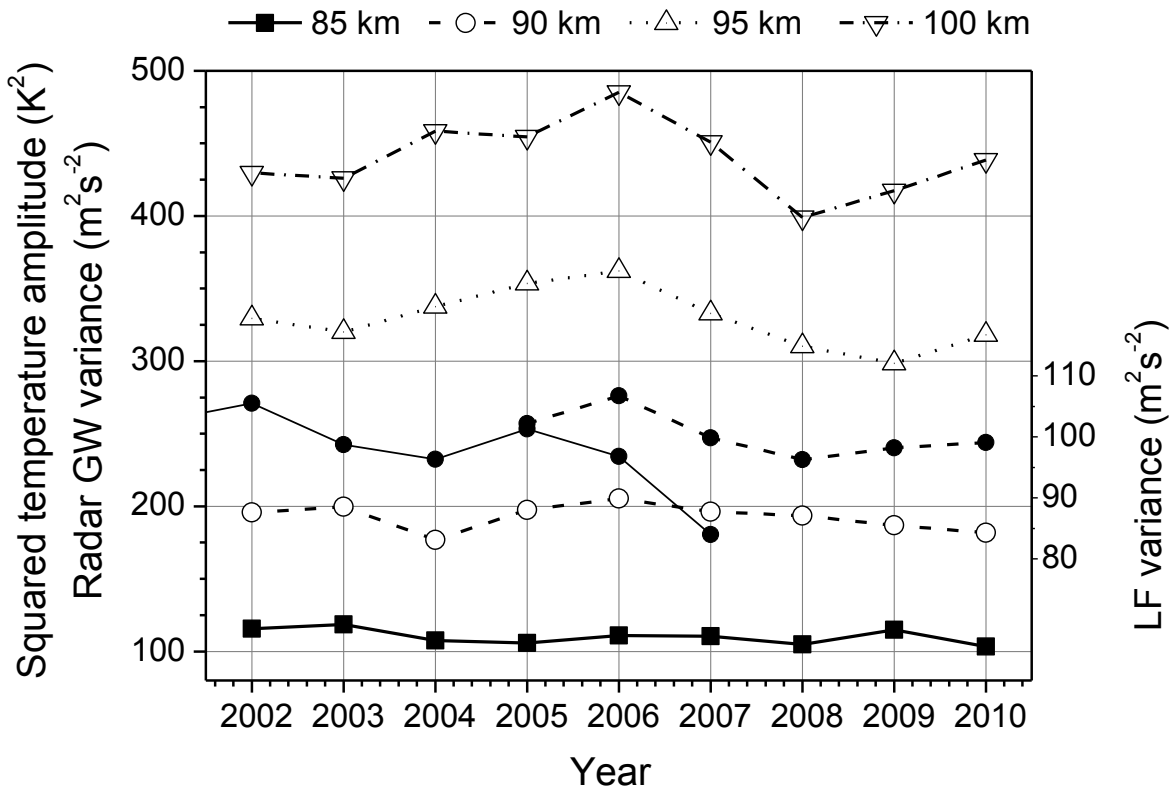


Figure 6: SABER 10°E squared temperature amplitudes 2002-2010 (solid squares, open circles, up and down open triangles) at different altitudes. LF variances at approx. 90 km from Fig. 2 (solid circles, solid lines) and GW variances from the Collm meteor radar (taken from Jacobi et al., 2011, updated from Placke et al., 2011) are added. A fixed value of $150 \text{ m}^2 \text{s}^{-2}$ has been subtracted from the meteor radar GW variances.

after the solar maximum GW amplitudes tend to decrease, but during the descending phase of the solar cycle they increase again, before they minimise during the solar minimum.

Vertical profiles of SABER temperature amplitudes and their vertical gradients are shown in Fig. 7. Again, the years 2008 and 2009 are highlighted. It can be seen that above 90 km the amplitudes are small during solar minimum while between 80 and 85 km they are comparable with the other years, or even larger. This is reflected in the small vertical gradients above 85-95 km. These indicate stronger GW forcing of the mean flow, and connected with that stronger wind shear at these heights and stronger westerly winds in the lower thermosphere, as can be seen in Figure 3. This connection is illustrated in Fig. 8, where the vertical shear of zonal wind at about 90 km is plotted vs. the squared SABER temperature amplitude gradient at 90 km. Note, however, that in 2007 the mesospheric easterly winds were particularly weak, connected with small wind shear values. These are, however, connected with only moderately large GW amplitude increase with altitude.

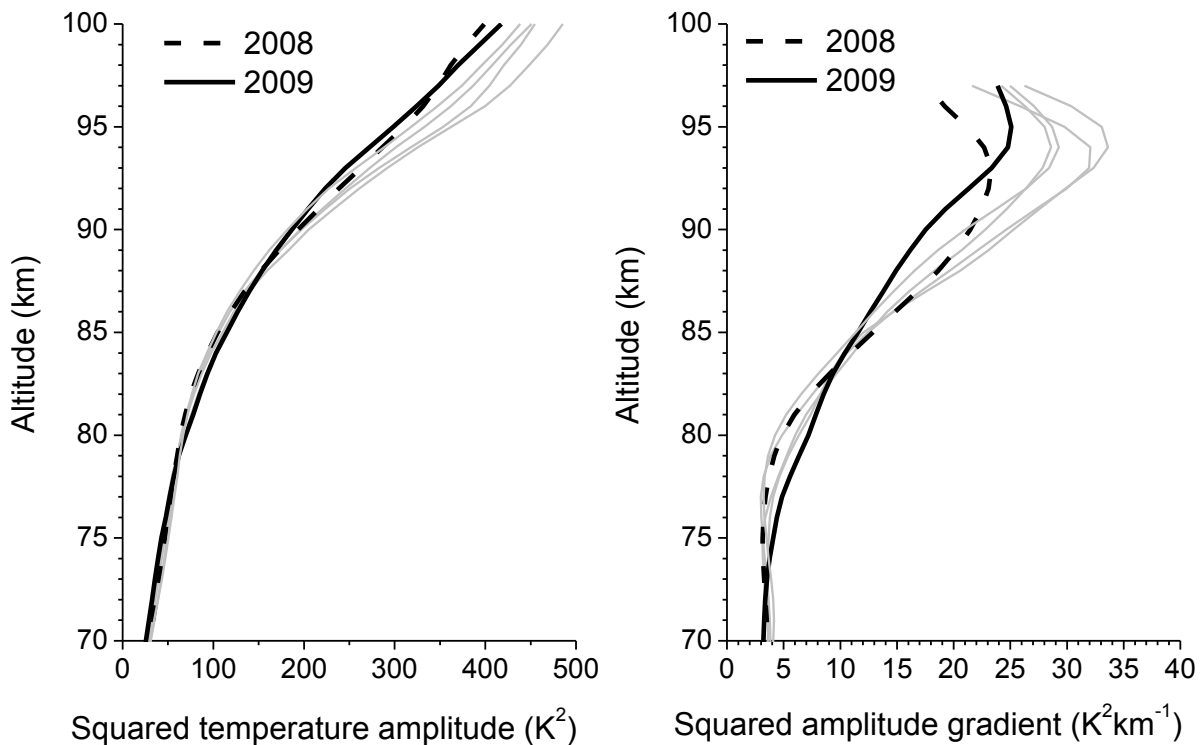


Figure 7: SABER 10°E squared temperature amplitudes (left panel) and vertical amplitude gradient (right panel).

Temperature amplitudes as shown in Figs 6-8 are useful because they can be compared with the LF or meteor radar wind variances in order to qualitatively validate the conclusions drawn from the latter. A more direct parameter to investigate GW-mean flow interaction, however, is the GW MF. Fig. 9 shows SABER MF time series at different altitudes. At mesospheric heights MF is broadly connected with the solar cycle, and decreases after the solar maximum, with the exception of the described increase during the descending part of the solar cycle. At greater altitudes, this behaviour partly reverses, so that there are large MF values especially in 2009. However, the interannual variability in general is more complicated and cannot easily be interpreted.

An even more suitable parameter is the MF divergence, which is shown in Fig. 10. MF divergence is usually weak in the mesosphere and thermosphere, and maximises at an altitude of 82-84 km. The peak height decreases with solar activity, so that the MF divergence, and therefore the main region where GW interact with the mean flow, is about 2 km higher during solar minimum than during solar maximum. This results in an anticorrelation of MF divergence taken slightly below and above the peak (Figure 11). The upward shift of the MF divergence profile during solar minimum may explain the upward shift of wind and wind shear profiles shown in Fig.5.

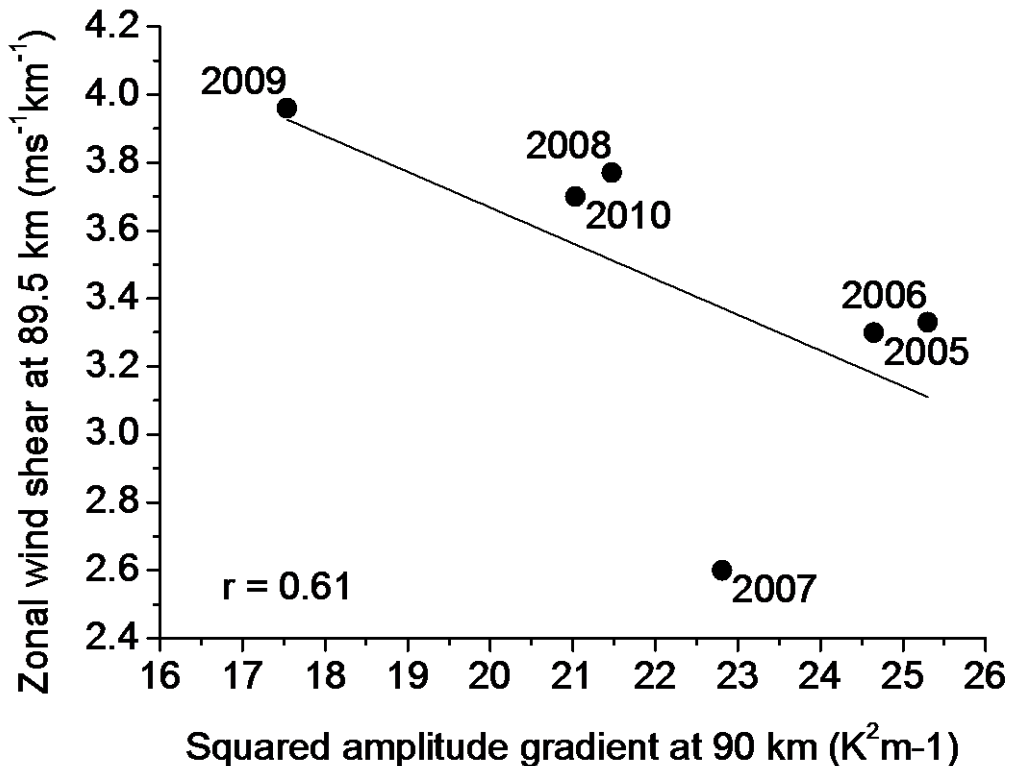


Figure 8: SABER squared temperature amplitude gradient at 90 km vs. vertical shear of zonal wind.

4 Discussion

As can be seen from Figs 2 and 6, GW amplitudes are modulated with the solar cycle so that large amplitudes are found during solar maximum. This behaviour changes and partly reverses during the descending phase of the solar cycle. The corresponding MF time series in Figure 9 clearly show this for the upper mesosphere. Concerning GW mean flow interaction, there is, at least during the time interval 2002-2010, a possible solar cycle modulation of the height of the peak MF divergence (Fig. 10). During solar maximum, when mesospheric MF are largest, they tend to decrease at lower altitudes (MF divergence peak already at 82 km) than during solar minimum (at about 84 km).

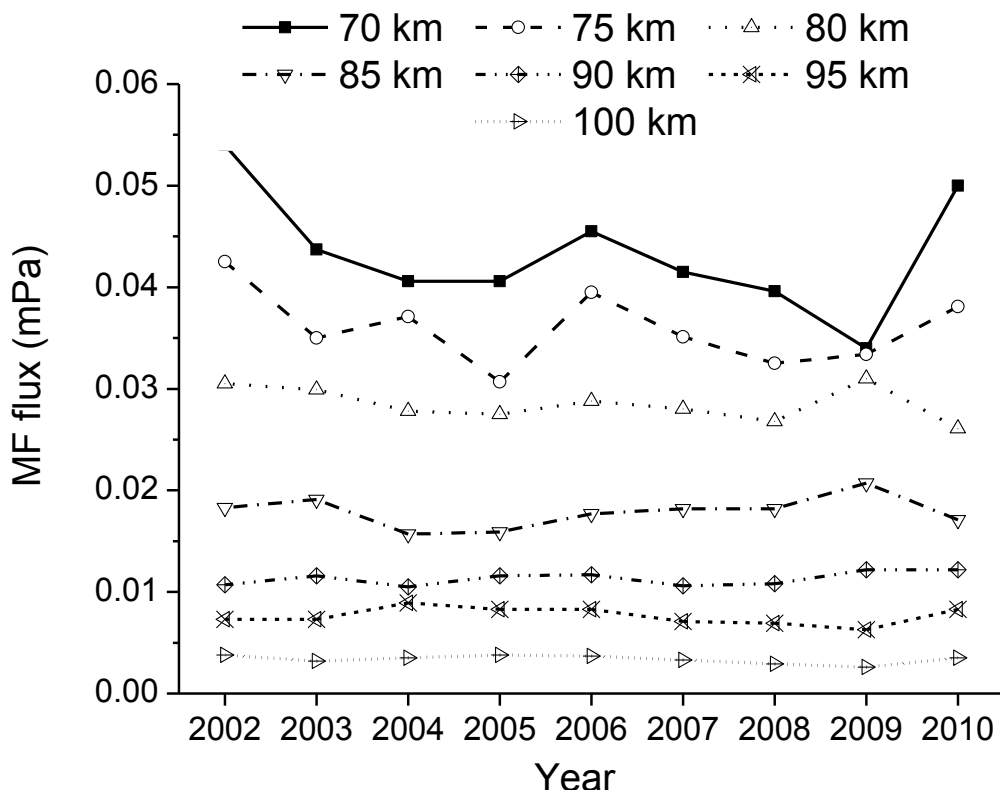


Figure 9: Time series of SABER MF at 10°E and at different altitudes.

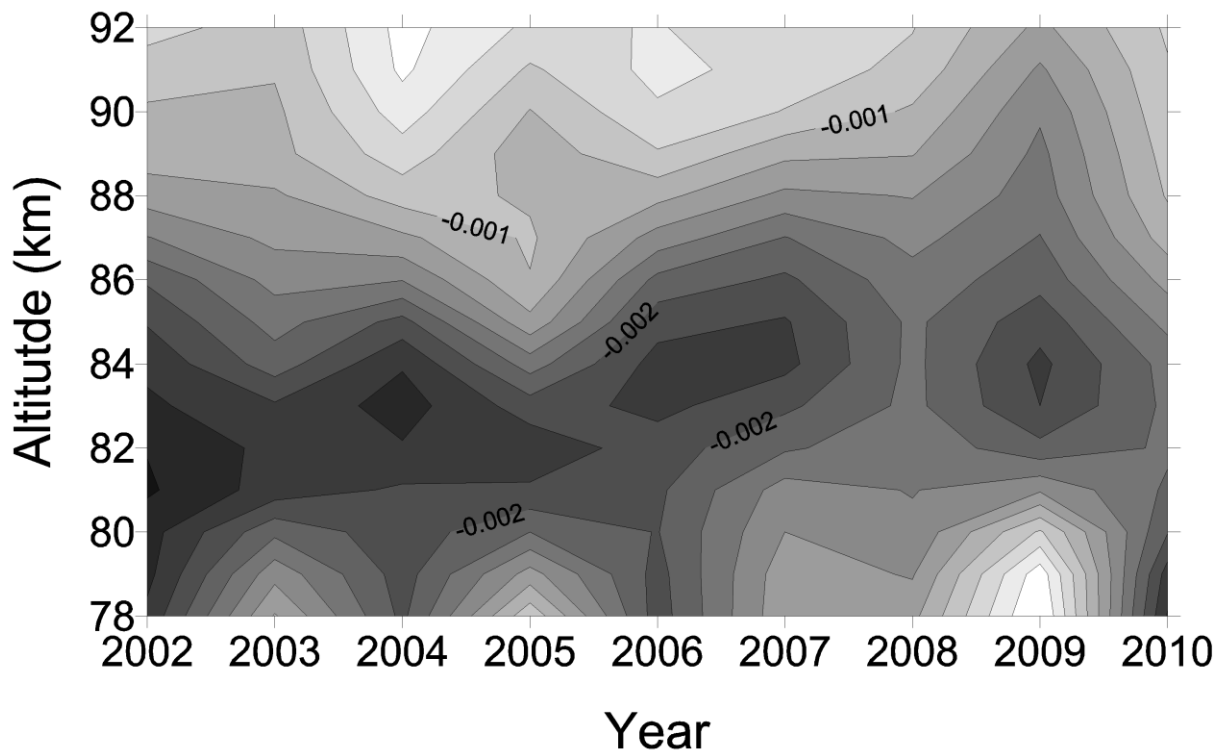


Figure 10: SABER MF divergence at 10°E.

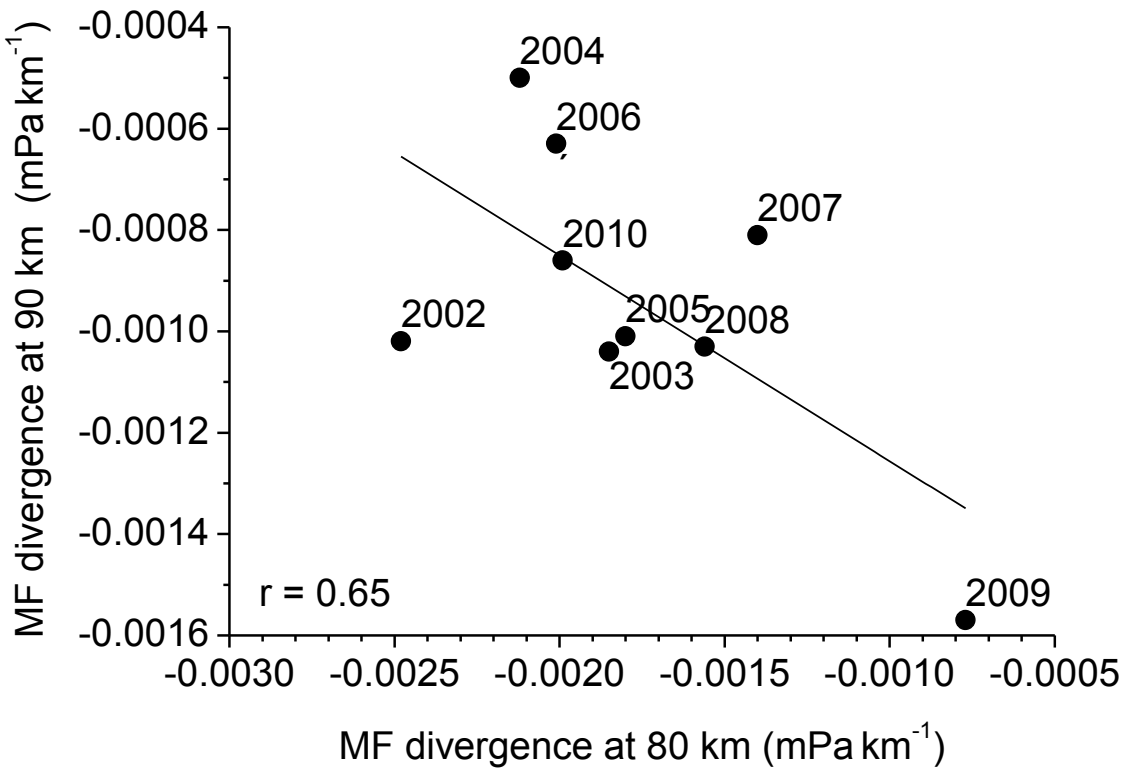


Figure 11: SABER MF divergence at 10°E at 90 km altitude vs. the respective values at 80 km.

A possible general picture thus is that the mesospheric zonal wind jet tends to be stronger during solar maximum (e.g., Schmidt et al., 2006). This may, assuming that GW are saturated and therefore the amplitudes are proportional to the intrinsic phase speed, lead to larger GW amplitudes then. However, GW seem to break earlier (at lower altitudes, as seen in Fig. 10) during solar maximum than during solar minimum. Therefore, the measured GW amplitude variability observed in the MLT probably results from a mixture of at least two processes. The first one is due to the larger/smaller GW amplitudes in the mesosphere during solar maximum/minimum. The second is the weaker MF divergence in the mesosphere during solar minimum, which in the MLT may counteract the first effect. A superposition of both may explain that MLT GW amplitudes are strong during solar maximum (due to the first effect) and during years of moderately low solar flux, when the second effect may be more effective, before during solar minimum the first effect again may take over.

The interannual variation of the MF divergence may explain part of the observed behaviour of winds. Comparing Figs. 3 and 10 we see that (except for the year 2007) there is a tendency for a decrease of both MF divergence and vertical shear of zonal wind at 83.5 km (the lowermost level where we have radar wind shear) until 2009, and then again an increase. At greater altitudes, we have the opposite behaviour in both parameters.

The year 2007 is, regarding the radar winds in Figs. 3-5, different from other ones. In the upper mesosphere the zonal wind values were weak. This was connected with a weak mesospheric jet, which also has been found by Hoffmann et al. (2011, their Fig. 3). However, this behaviour different from other years is not reflected in a similarly strong change of GW amplitudes or MF, and the reason is unclear. Obviously, there are other possible sources of MLT wind and GW variability than a pure solar cycle modulation, e.g. changes of GW sources and other variations of the mesospheric circulation.

5 Conclusions

We have analysed summer zonal mean MLT winds over Collm together with GW analyses from SABER from 2002-2010 to get more insight into the sources of interannual wind variability. MLT GW MF are stronger during solar maximum than during solar minimum, and there is a secondary maximum during the descending phase of the solar cycle. This confirms earlier results from LF measurements, and a comparison of LF wind variances with SABER squared temperature amplitudes show very good qualitative agreement.

The variability of GW in the course of a solar cycle may be partly explained by a superposition of a solar cycle in the mesospheric wind jet that leads to larger GW amplitudes during solar maximum, and an upward shift of the region of maximum GW-mean flow interaction during solar minimum. This upward shift may be explained by the fact that small-amplitude GW generally tend to break at lower altitudes than large-amplitude GW. This upward shift may also explain the upward shift of the observed wind and wind shear profiles during solar minimum, leading to a reversal of the (otherwise negative) solar cycle effect in zonal winds then.

The effects outlined here are clearly not the only sources of variability in MLT GW and winds. Examples are the large MF values in 2006, probably due to a strong mesospheric jet, or the very weak winds, both mesospheric eastward and lower thermospheric westward, in 2007. In a further study we shall analyse mesospheric winds derived from SABER temperatures as well.

The results presented here are based on local radar data and satellite data from a $30^\circ \times 10^\circ$ longitude/latitude window. An interesting question is also, whether the solar cycle effect is as well visible in zonal mean data, or whether the effects are of local nature. Radar MLT mean winds taken at different longitudes (Canada, Central Europe, and Eastern Europe) partly showed strong differences at the decadal time scale (Jacobi et al., 2012). This should also be addressed in a future study.

Acknowledgements

SABER data were provided by GATS Inc. Many thanks also go to the teams of the SABER instruments for all their effort to create the excellent data sets. F10.7 solar radio flux data have been provided by NGDC through ftp access on ftp://ftp.ngdc.noaa.gov/STP/SOLAR_DATA/.

References

- Ern, M., Preusse, P., Alexander, M.J., Warner, C.D., 2004: Absolute values of gravity wave momentum flux derived from satellite data. *J. Geophys. Res.*, 109, D20103, doi:10.1029/2004JD004752.
- Ern, M., Preusse, P., Gille, J.C., Hepplewhite, C.L., Mlynczak, M.G., Russell III, J.M., Riese, M., 2011: Implications for atmospheric dynamics derived from global observations of gravity wave momentum flux in stratosphere and mesosphere. *J. Geophys. Res.* 116, D19107, doi:10.1029/2011JD015821.
- Hocking, W.K., 2005: A new approach to momentum flux determinations using SKi-YMET meteor radars. *Ann. Geophys.* 23, 2433–2439.
- Hoffmann, P., Rapp, M., Singer, W., Keuer, D., 2011: Trends of mesospheric gravity waves at northern middle latitudes during summer. *J. Geophys. Res.* 116, D00P08, doi:10.1029/2011JD015717.
- Jacobi, Ch., 2011: Meteor radar measurements of mean winds and tides over Collm (51.3°N, 13°E) and comparison with LF drift measurements 2005-2007. *Adv. Radio Sci.* 9, 335-341.
- Jacobi, Ch., Schminder, R., Kürschner, D., 1996: On the influence of the stratospheric quasi-biennial oscillation on the mesopause zonal wind over Central Europe. *Meteorol. Zeitschrift*, N.F. 5, 318-323.
- Jacobi, Ch., Gavrilov, N.M., Kürschner, D., Fröhlich, K., 2006: Gravity wave climatology and trends in the mesosphere/lower thermosphere region deduced from low-frequency drift measurements 1984-2003 (52.1°N, 13.2°E). *J. Atmos. Solar-Terr. Phys.* 68, 1913-1923.
- Jacobi, Ch., Hoffmann, P., Placke, M., Stober, G., 2011: Some anomalies of mesosphere/lower thermosphere parameters during the recent solar minimum. *Adv. Radio Sci.* 9, 343-348.
- Jacobi, Ch., Hoffmann, P., Liu, R.Q., Merzlyakov, E.G., Portnyagin, Yu.I., Manson, A.H., Meek, C.E., 2012: Long-term trends, their changes, and interannual variability of Northern Hemisphere midlatitude MLT winds. *J. Atmos. Solar-Terr. Phys.*, 75-76, 81-91, doi:10.1016/j.jastp.2011.03.016.
- Keuer, D., Hoffmann, P., Singer, W., Bremer, J., 2007: Long-term variations of the mesospheric wind field at mid-latitudes. *Ann. Geophys.*, 25, 1779–1790.

Muller H.G., Nelson L., 1978: A travelling quasi 2-day wave in the meteor region. *J. Atmos. Terr. Phys.*, 40, 761- 766.

Placke, M., Stober, G., Jacobi, Ch., 2011: Gravity wave momentum fluxes in the MLT—Part I: Seasonal variation at Collm (51.3°N, 13.0°E). *J. Atmos. Solar–Terr. Phys.*, 73, 904-910, doi:10.1016/j.jastp.2010.07.012.

Schmidt, H., Brasseur, G.P., Charron, M. , Manzini, E., Giorgetta, M.A., Diehl, T., Fomichev, V.I., Kinnison, D., Marsh, D., Walters, S., 2006: The HAMMONIA chemistry climate model: Sensitivity of the mesopause region to the 11-year solar cycle and CO₂ doubling. *J. Climate*, 19, 3903-3931.

Addresses of Authors

Christoph Jacobi, Institut für Meteorologie, Universität Leipzig, Stephanstr. 3, 04103 Leipzig.

Manfred Ern: Forschungszentrum Jülich GmbH, Institut für Energie- und Klimaforschung, IEK-7: Stratosphäre, 52425 Jülich.

Terdiurnal signatures in midlatitude sporadic E layers occurrence rates

T. Fytterer, C. Arras, and C. Jacobi

Summary

Global Positioning System radio occultation measurements by the FORMOsa SATellite mission-3/Constellation Observing System for Meteorology, Ionosphere and Climate satellites were used to analyse the behaviour of the signature of the terdiurnal tide in sporadic E (E_s) layers at midlatitudes (43°N – 63°N). According to theory, the occurrence of E_s is expected when the vertical zonal wind shear, which is mainly owing to solar tides, is negative. 4-year means, based on 3-monthly running mean zonal means from December 2006 - November 2010, were constructed for the terdiurnal oscillation in the occurrence frequency of E_s . Comparison of the results with VHF meteor radar observations of the terdiurnal tide and the 8-hr oscillation in the vertical zonal wind shear at Collm, Germany (51.3°N , 13°E) shows a clear correspondence between the 8-hr E_s and wind shear signature.

Zusammenfassung

Radiookultationsmessungen auf der Basis von GPS-Messungen der FORMOsa SATellite mission-3/Constellation Observing System for Meteorology, Ionosphere and Climate-Satelliten wurden verwendet, um die Signatur der 8-stündigen Gezeiten in den Auftrittsraten von sporadischen E (E_s)-Schichten zu analysieren. Nach der allgemein anerkannten Windscherungstheorie treten E_s -Schichten im Bereich negativer vertikaler Windscherung auf, welche in der unteren Thermosphäre hauptsächlich durch solare Gezeiten hervorgerufen werden. Speziell werden hier 4-jährige Mittelwerte saisonal gemittelter Auftrittsraten untersucht um die 8-stündige Signatur zu finden. Ein Vergleich mit Radarmessungen des Windes über Collm zeigt, dass die saisonale und tägliche Variabilität der 8-stündigen Komponente der E_s -Raten sehr gut mit derjenigen der gemessenen Windscherung übereinstimmt.

1 Introduction

The wind fields of the mesosphere/lower thermosphere (MLT) are strongly influenced by atmospheric solar tides. These are global waves with periods of a solar day and its subharmonics and are therefore named diurnal tide (DT), semidiurnal tide (SDT), terdiurnal tide (TDT), etc. The tides are excited by absorption of solar radiation in the lower atmospheric layers (troposphere, stratosphere) and partly by wave-wave interactions (Teitelbaum et al., 1989). The wind amplitudes are small (on the order of few cm/s) near the region of forcing, but increase significantly with height due to the decreasing air density. They maximise in the MLT at midlatitudes (Hagan et al., 1995). At these altitudes, the tides are the most dominant dynamical feature. The amplitudes are of the order of the magnitude of the mean wind and exceed those of planetary or gravity waves. Therefore, solar tides play an important role in the global circulation

and a more accurate knowledge would result in a better understanding of the dynamics in the MLT. At midlatitudes, the strongest tide is the SDT, but in October the TDT also reaches significant amplitudes of 10 m/s and more (Fytterer and Jacobi, 2011). Thus, and since the climatology of the TDT is less intensely investigated than that of the DT and SDT so far, the TDT should be considered for further investigations of the global dynamics.

Sporadic E (E_S) layers are thin clouds of enhanced electron density, at midlatitudes primarily occurring in summer. They generally form in the upper MLT (90 – 120 km), which is equivalent to the lower ionospheric E region. According to wind shear theory (Whitehead, 1961) the forming process of E_S is influenced by Earth's magnetic field, the ion concentration and the vertical wind shear as well. Neglecting diffusion, the vertical velocity of the neutral gas and the electric force, the vertical ion velocity w_{Ion} can be written as:

$$w_{Ion} = \frac{r \cdot \cos I}{1 + r^2} U - \frac{\cos I \cdot \sin I}{1 + r^2} V, \quad (1)$$

where U and V are the zonal and meridional wind component of the neutral gas, while I is the inclination of the Earth's magnetic field. The parameter $r = (v_{Ion/N} \cdot m_{Ion})/(e \cdot B_0)$ includes the ion-neutral gas collision frequency $v_{Ion/N}$, the ion mass m_{Ion} , the elementary charge e and the total intensity B_0 of the Earth's magnetic field. Note that for deriving Eq. 1 Cartesian coordinates were used (x , y and z point eastward, northward and upward, respectively), which differs from the usual notations in literature. Considering that $r \gg 1$ at atmospheric regions below ~115 km (Bishop et al., 2003), the zonal wind component is significantly more efficient in causing a vertical plasma motion than the meridional wind component.

Furthermore, the formation of E_S requires negative vertical wind shear (Eq. 1), whose main source are the solar tides, partly providing larger vertical wind gradients than the background wind. Considering wind shear theory thus tidal-like structures are expected in E_S . Recent studies have shown from phase comparison of the SDT wind shear and E_S signature that the latter are most likely caused by the SDT (Arras et al., 2009). Therefore, it appears also promising to search for a relation between the TDT and terdiurnal oscillations in E_S .

In the following we analyse the terdiurnal signature in VHF meteor radar winds and wind shear over Collm, Germany. The seasonal cycle of these amplitudes will be compared against the TDT signature in E_S obtained from Global Positioning System (GPS) radio occultation (RO) measurements by the FORMOsa SATellite mission-3/Constellation Observing System for Meteorology, Ionosphere and Climate (FORMOSAT-3/COSMIC). TDT phases as seen in E_S and wind shear will be compared as well.

2 Measurements and data analysis

The GPS RO technique is used here to analyse the behaviour of E_S . The method bases on radio links between Low-Earth Orbiting (LEO) satellites and GPS satellites. We

use FORMOSAT-3/COSMIC measurements, assuring global coverage as well as a high vertical resolution. Due to the low Earth orbits of the FORMOSAT-3/COSMIC satellites, the GPS satellites are nearly fixed with respect to them and are observed as setting or rising objects. During this occultation the GPS signal is modified according to the atmospheric refraction index, containing information about air temperature, air pressure, water vapour content and electron density. The first three parameters are mainly tropospheric disturbances and are negligible in the ionosphere. As a result one occultation provides a complete vertical profile of the electron density. By analysing the signal-to-noise ratio (SNR), it is possible to extract an E_s signature from the background noise (Wu et al., 2005).

The disturbances of the signal are caused by divergence/convergence of the radio wave, leading to a decreased/increased intensity of the received signal. For analysis, first the SNR is normalised by dividing the measured SNR by the respective mean SNR. In the next step a band pass filter is used, only accepting disturbances smaller than 5 km in height range to account for the thin structure of E_s layers. Furthermore, the standard deviation of the normalised SNR is calculated for each height interval covering a sliding window of 2.5 km. Since E_s cause sharp gradients in the electron density within a few kilometres, the fluctuations have to be strong and show a sharp vertical gradient. Consequently, the standard deviation of the normalised SNR should exceed the empirically found threshold of 0.2 and rises above 0.14 between two adjacent intervals to be accepted as an E_s signature. Note that if the standard deviation rises above the limit 0.2 in more than 5 intervals, the profile is excluded from further investigations to avoid similar disturbances from other sources (Arras, 2010). The height of maximum deviation from the mean profile is regarded as the approximate altitude of the E_s . Assuming spherical geometry the E_s is located where the radio wave is most refracted (the tangent point), whose exact coordinates are calculated, using at least four GPS satellites.

The six FORMOSAT-3/COSMIC satellites are operating since summer 2006, but this study only considers zonal mean values from December 2006 – November 2010. Therefore, the ROs of every longitude in the latitude range 43°N – 63°N are used, with the mean latitude of the occultations within this interval at 51°N . The time interval includes 3 months and the reference month was taken as the second one of the interval, i.e. as the centre of the interval.

As can be seen in Fig. 1, the available data are nearly uniformly distributed among seasons, with about 10000 per month (30000 per season). Lower sample rates only occur in 2010, because satellites were out of contact or some new firmware was tested (CDAAC Team, 2012). But for constructing the climatology a sufficient amount of data still remains. To give an overview of the general characteristics of the detected E_s , Fig. 2 shows the seasonal cycles of the total number of E_s (upper panel) and of the occurrence frequency (lower panel). The latter one is the number of detected E_s divided by the respective number of ROs and finally multiplied by the factor 1000 for more handy values. Averages over a sliding height interval of 11 km, shifted by 1 km, were calculated and the reference height was taken as the centre of the interval. The above mentioned time and vertical height intervals are used in every following plot

concerning E_S , unless explicitly stated. The behaviour of E_S number and occurrence frequency is quite similar, due to the equally distributed RO in the course of a year. In general, E_S rates maximise around 105 km. In summer, more than 4500 E_S per season and 11 km interval were detected. The respective occurrence frequency reaches values above 0.14. This seasonal cycle is caused by the variations of the meteor rates (see, e.g., Haldoupis et al., 2007, their Fig. 3), in combination with the dynamics in the MLT. Significantly lower E_S rates are observed below 90 km and above 115 km, as well as from December until April.

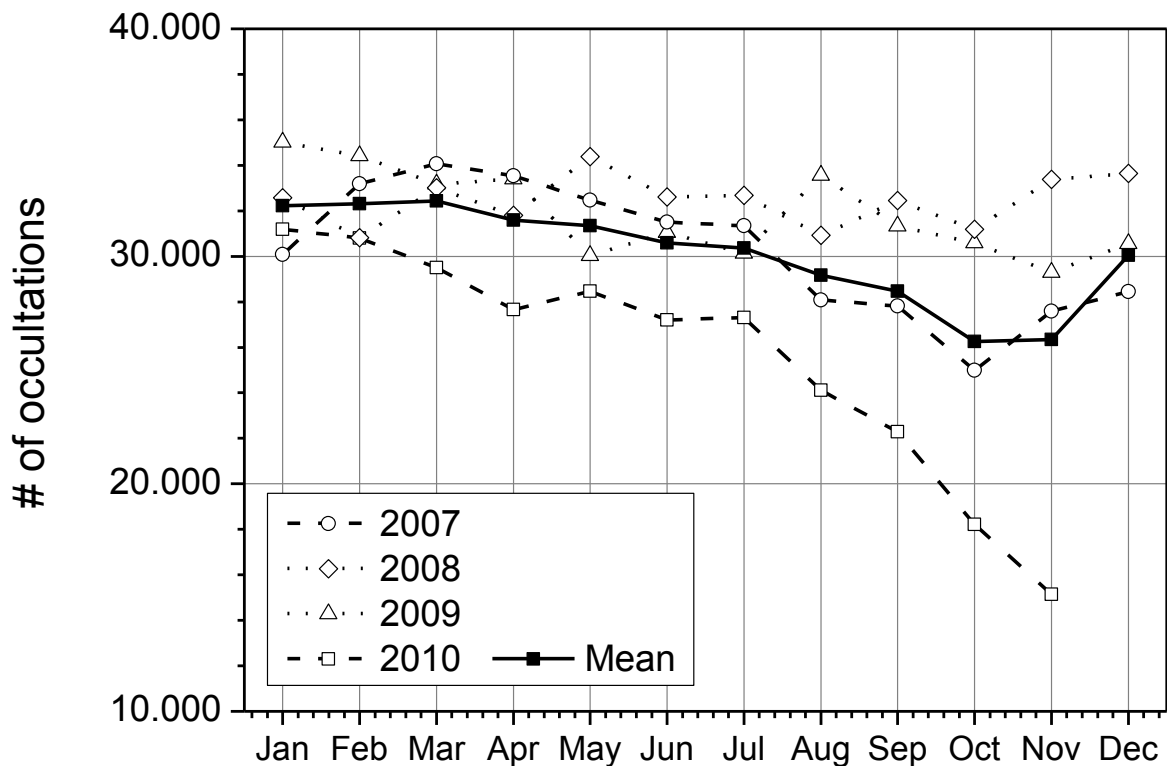


Figure 1: 3-monthly numbers of radio occultations in the latitude range $43^{\circ}\text{N} - 63^{\circ}\text{N}$ measured by the FORMOSAT-3/COSMIC satellites. The reference month represents the centre of the respective time interval. The 4-year mean (solid curve) also includes the data for December 2006, which is not shown in the figure.

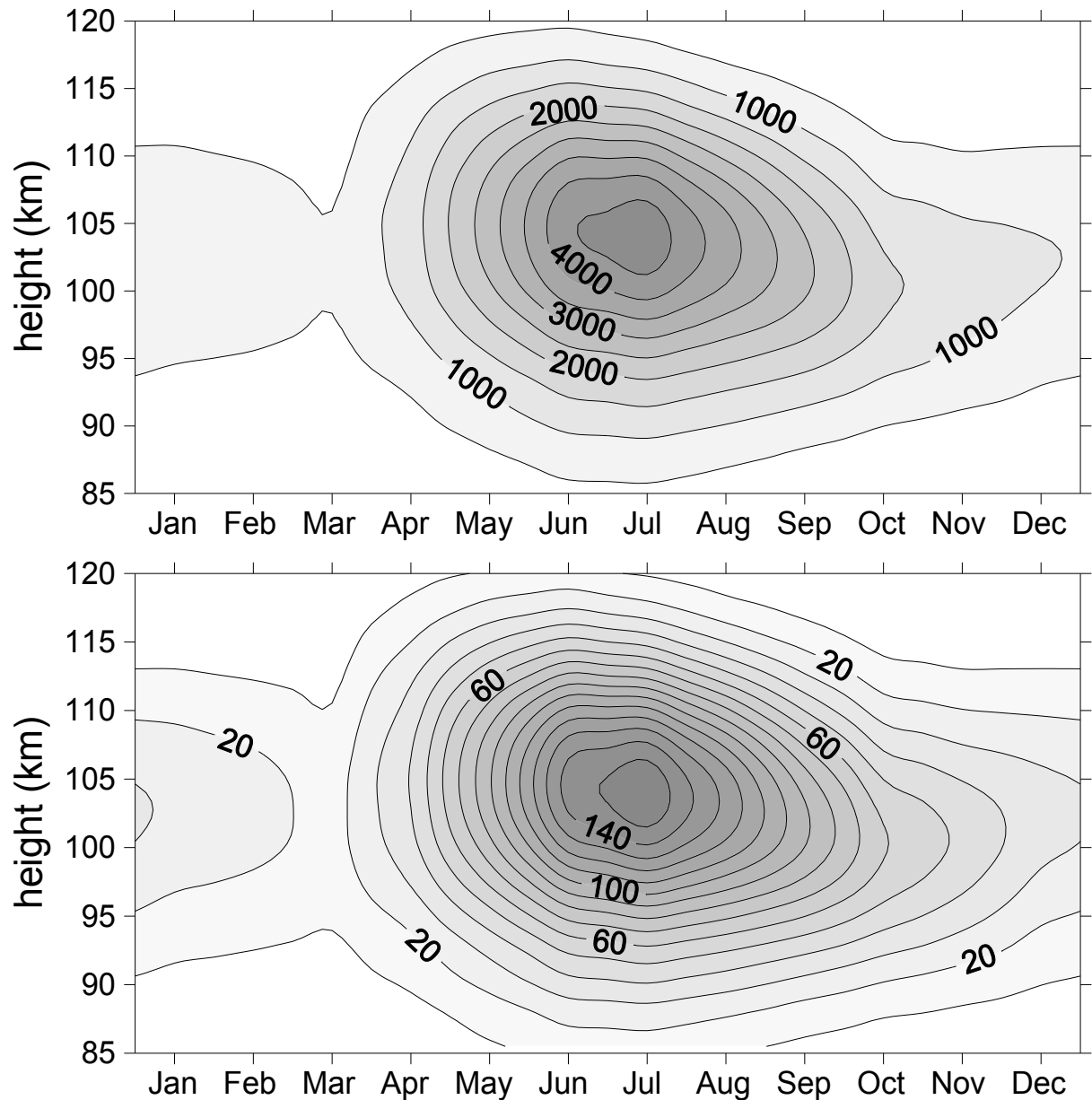


Figure 2: Seasonal cycle of the total number of sporadic E layers (upper panel) and the occurrence frequency (in 1/1000, lower panel) in the latitude range $43^{\circ}\text{N} - 63^{\circ}\text{N}$ as derived from FORMOSAT-3/COSMIC measurements. Shown are 4-year averages calculated from 3-monthly running mean zonal means using data from November 2006 – December 2010 with the respective height interval covering a sliding window of 11 km width, shifted by 1 km.

The SKiYMET meteor radar located at Collm, Germany ($51.3^{\circ}\text{N}, 13^{\circ}\text{E}$) has been in operation nearly continuously since July 2004 and the 7-year dataset from August 2004 – July 2011 is used here for analysing the vertical wind shear and the TDT. The radar is operated at 36.2 MHz with a pulse repetition frequency of 2144 Hz, a peak power of 6 kW and a pulse length of 2 km. The emitted VHF radio wave is scattered

by ionised meteor trails. The detection array includes five antennas forming an asymmetric cross to act as an interferometer. This constellation allows, in combination with range measurements, the calculation of the position of the detected meteor trail. The meteor rates vary strongly in time and space, peaking in summer and slightly below 90 km, respectively (Fig. 3). The investigated height interval is divided into six non-overlapping height gates, binned at 82, 85, 88, 91, 94 and 98 km. Note that the real mean meteor height in the uppermost gate is only 97 km due to the decreasing meteor rates with altitude (Jacobi, 2012). The radial wind velocity is obtained from the Doppler phase progression with time at each receiver. Horizontal half-hourly mean winds are calculated through projecting these mean winds on the individual radial winds and minimizing the squared differences. An outlier rejection is added (Hocking et al., 2001). Half-hourly wind shears are calculated from the difference of the winds at two adjacent height gates.

Monthly mean winds and tidal (8, 12, 24 hr) amplitudes and phases are calculated using a multiple regression analysis of the half-hourly mean winds as well as the wind shears. The procedure is described in detail in Jacobi (2012). Three-monthly running means are calculated using vector averaging for the phases and arithmetic averaging for the amplitudes.

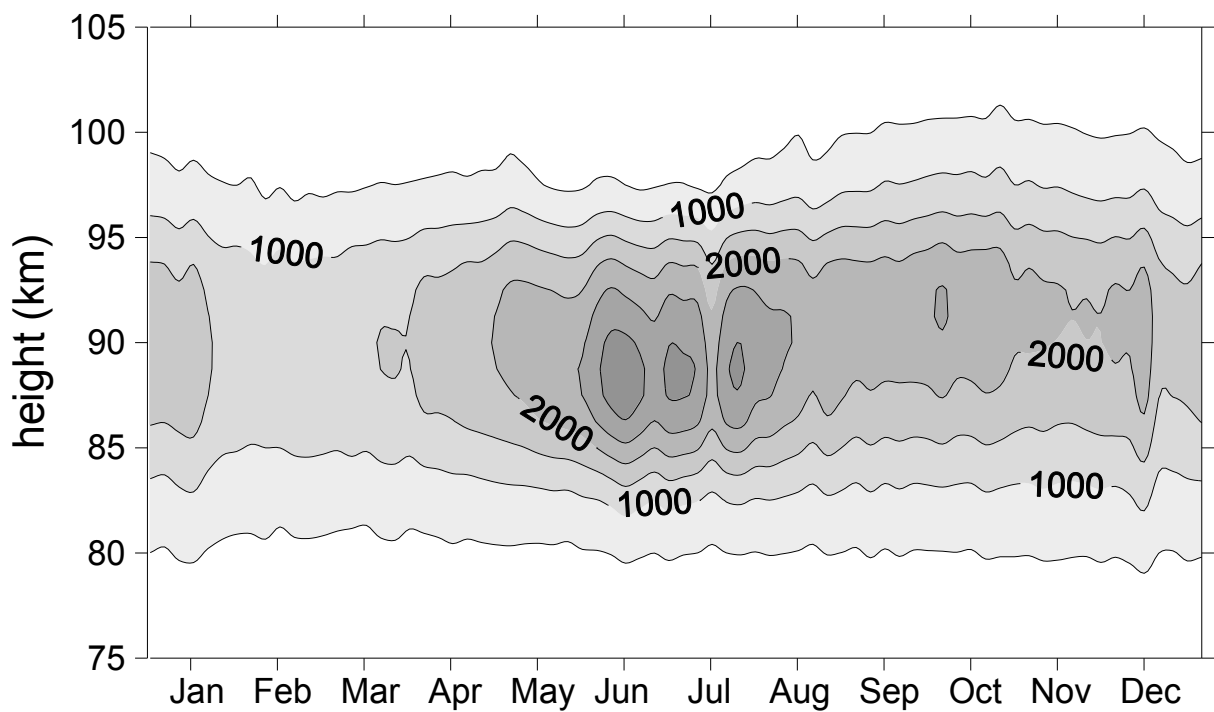


Figure 3: Height-time cross-section of 2005–2010 mean meteor count rates per day and per 5 km interval as measured by the meteor radar at Collm.

3 Results

To investigate the structure of the E_s rates in more detail, the terdiurnal oscillation was extracted from the occurrence frequency (referred here as 8-hr E_s) by using the same kind of multiple regression analysis as has been applied for the winds, but on the E_s data from each longitude, which had been sorted according to local time, while the time resolution was set to 1 hr. Previously performed frequency-wave number analyses (not shown here) have ensured that the westward migrating component is the dominant oscillation in 8-hr E_s . Each fit includes the occurrence rates during 3 months. This analysis applied for 12 data windows centred at each month of the year. The height interval covers a sliding window of 11 km, which is shifted by 1 km.

To introduce the analysis and to visualize the 8-hr oscillation in E_s , as an example, Fig. 4 (left panel) shows the 3-monthly mean hourly occurrence rates and modelled values derived through least-squares fitting of a mean, 8-hr, 12-hr, and 24-hr component (dashed line). The used harmonic fit matches well with the observed occurrence rates, indicating that no further significant oscillations are present in the diurnal cycle of the E_s rates. However, the terdiurnal wave signature is hardly visible, because the 24-hr and 12-hr waves are dominating. Therefore, the harmonic analysis was repeated here without considering an 8-hr component (solid line in Figure 4a), and the residuals are plotted in Figure 4b. Now the terdiurnal signature is clearly visible. Note that the shown fit of an 8-hr oscillation in Figure 4b provides nearly identical coefficients than the same harmonic fit applied for the original occurrence rates.

Using ionosonde measurements from July 2006 to June 2007 over Tehran, Iran (35.4°N , 51.2°E), Karami et al. (2012) also investigated 8-hr signatures in E_s . They found terdiurnal variations in the E_s critical frequency ($f_0 E_s$) in spring and summer and in the E_s virtual height ($h' E_s$) in summer and winter, respectively. This also indicates that the terdiurnal tide-like oscillation in E_s as seen by GPS RO has a physical reason and is not a mere mathematical artefact.

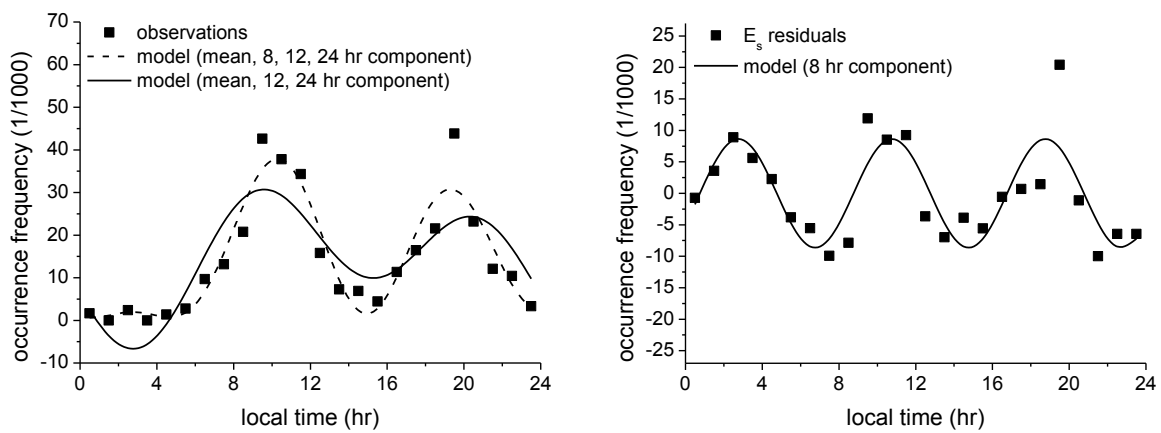


Figure 4: Comparison of the measured occurrence rates with the fitting results at ~ 112.5 km during October 2010 for a latitude range from $43^\circ\text{N} - 63^\circ\text{N}$ (left panel). The right panel shows the residuals from a fit that includes the 12 and 24-hr component and the results of fitting an 8-hr component on these.

The seasonal cycle of the amplitude of the 8-hr E_s signature, given in Fig. 5, reveals nearly no activity below 90 km and in winter, while the maximum occurs around 105 km during summer, reaching values above 0.022. The corresponding occurrence rate is about $\sim 140/1000$, revealing that 22/140 (~15%) of the E_s variability is caused by the 8-hr E_s . In contrast to the occurrence rates, a secondary maximum is visible in late autumn ($>10/1000$), where the 8-hr E_s influence increased to 10/40 (25%). This indicates at least one additional 8-hr signature source. Considering wind shear theory, the influence of the TDT is suggested, because the TDT reaches maximum amplitudes in autumn (Fytterer and Jacobi, 2011).

The observed seasonal behaviour is in good agreement with the results presented by Haldoupis and Pancheva (2006), who investigated terdiurnal tide-like oscillations in f_0E_s observed by the ionosonde at Rome (41.9°N, 12.5°E). Their analysed data included the years 1980 – 1991, but only the months May – October. However, the seasonal characteristics of the 8-hr E_s amplitude are strongly related to the behaviour of the occurrence frequency (Fig. 2, lower panel) and the dominating maximum in summer might be due to the higher E_s mean rates, which generally cause larger absolute fluctuations. Therefore, the influence of the background E_s activity cannot be neglected and has to be taken into account in further analysis.

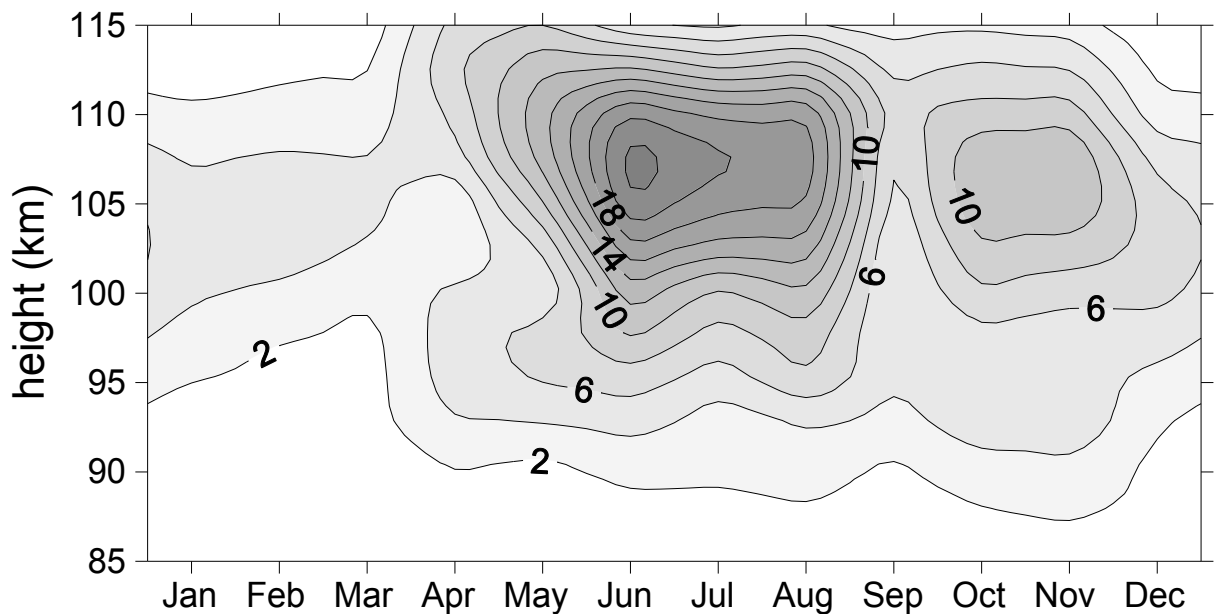


Figure 5: Amplitude (given in 1/1000) of the 8-hr oscillation within the occurrence frequency of the sporadic E layers.

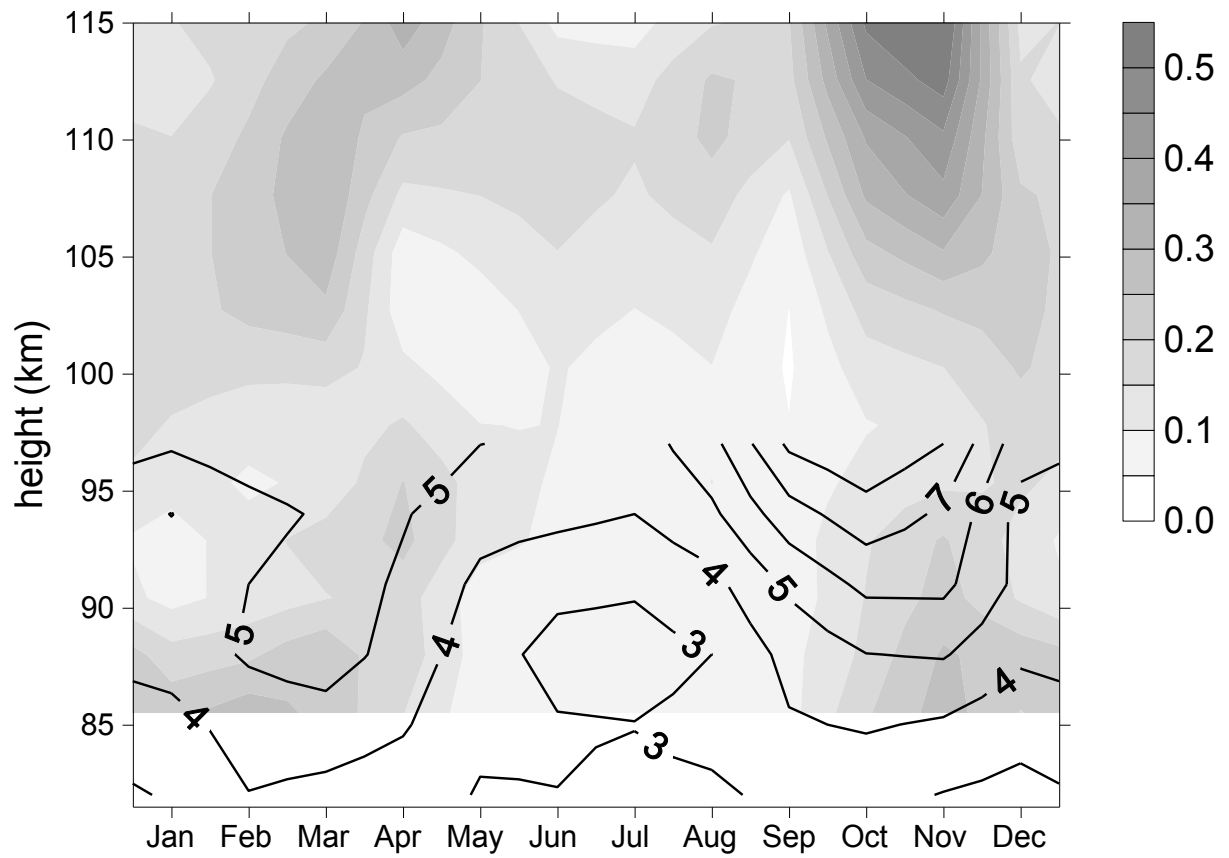


Figure 6: Normalised amplitude of the 8-hr oscillation within the E_s occurrence frequency (grey shading). Isolines show the amplitude (m/s) of the terdiurnal zonal wind tide, measured by the meteor radar at Collm, using the data from August 2004 – July 2011.

The amplitudes of the 8-hr E_s were normalised by dividing them through the respective 3-monthly mean zonal mean E_s occurrence rates. The results are presented in Fig. 6 (grey shading) and were compared with the amplitude of the TDT as observed by meteor radar (isolines). The obtained normalised amplitudes do not show maximum values in summer any more, confirming wind shear theory as 8-hr signature source. The largest values are seen in October and November, reaching amplitudes of ~ 0.5 between 110 km and 115 km. Also evident is a secondary maximum in spring, which is weaker by a factor of 2. This seasonal cycle closely correlates with the one of the wind TDT at lower heights, where the amplitudes are also small during summer ($\sim 3 - 4$ m/s) and maximise in October (~ 8 m/s) and March (~ 5 m/s), respectively. Note that the TDT wind amplitudes generally increase with height, while the 8-hr E_s amplitude decreases between 90 km and 100 km, in particular during equinoxes. This may be due to the low E_s rates (see Fig. 2) and the weak absolute amplitudes (Fig. 5), which means that small fluctuations can result in strong relative variations. This behaviour is not seen in summer. Furthermore, the maxima in both seasonal cycles are slightly shifted in time. However, a full agreement cannot be expected, due to the different observed height intervals.

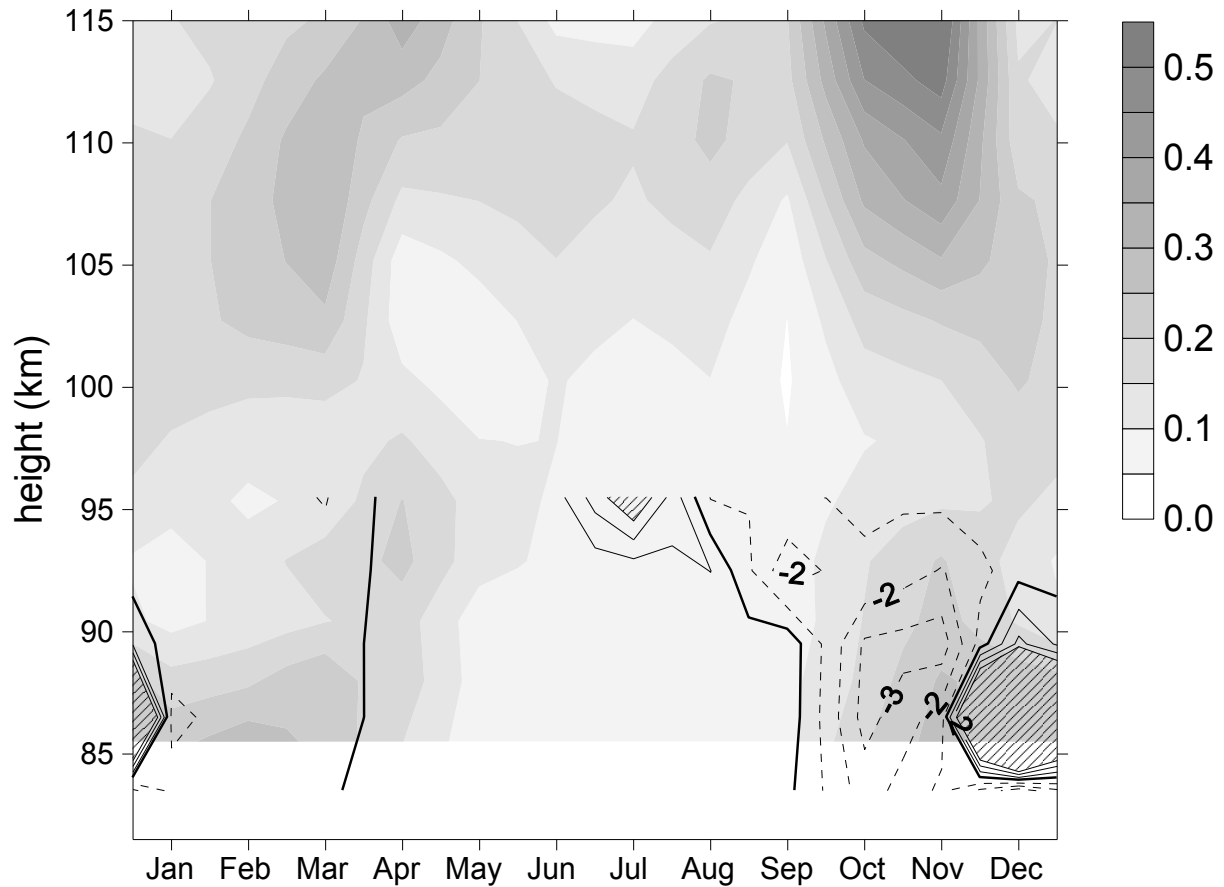


Figure 7: Normalised amplitude of the 8-hr oscillation within the occurrence frequency of the sporadic E layers (grey shading). The isolines show the normalised amplitude of the 8-hr oscillation in the vertical wind shear, as measured by the meteor radar at Collm, using the data from August 2004 – July 2011. The zero wind shear line is highlighted and negative shear values are marked as dashed isolines.

Assuming that E_s are formed by the wind shear mechanism, the 8-hr oscillation in the vertical wind shear (referred to as 8-hr shear here) was calculated and subsequently normalised by dividing the 8-hr shear amplitude by the respective mean shear. In Fig. 7, the normalised 8-hr shear is compared with the normalised 8-hr E_s amplitude. Note that the mean shear is sometimes very low, which leads to large normalised values (dashed areas), which should not be over-interpreted. Large negative values, which are observed in autumn (~ -3), imply a negative mean shear together with comparatively large 8-hr shear amplitudes. In general, negative normalised amplitudes dominate from September through March, while positive ones are present in summer and late spring. This correlates with the seasonal behaviour of normalised 8-hr E_s as well as the amplitude of the TDT. Note that the result corresponds to the wind shear theory, because during positive mean wind shear, tides can still provide a negative shear gradient.

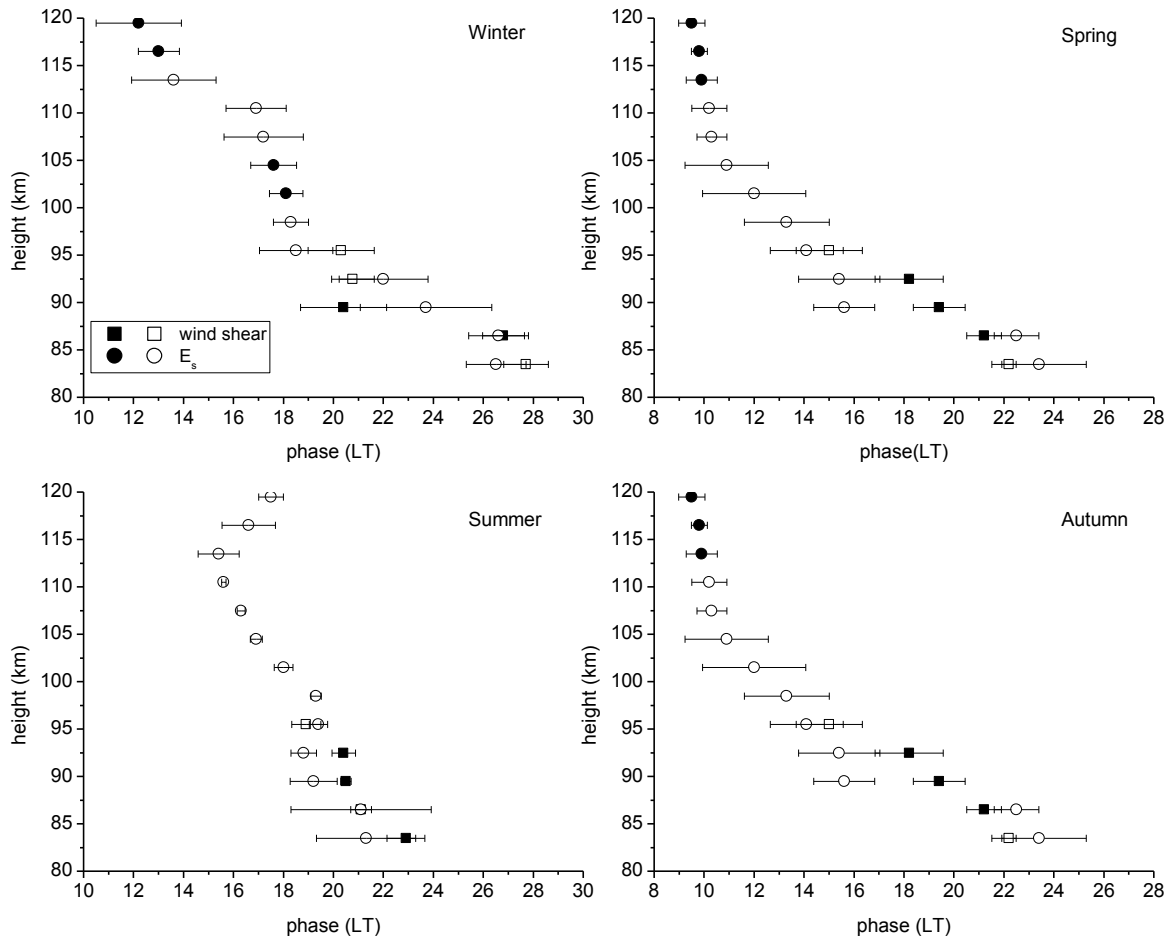


Figure 8: Phases of the 8-hr oscillations in the zonal vertical wind shear (squares) and the sporadic E layers (circles) for each season, based on 3-monthly running means from January 2007 – October 2010. Solid symbols indicate significant amplitudes according to a t-test. The error bars indicate the standard deviation of the individual seasonal mean values.

To further confirm the relation between the wind shear and the occurrence rates of E_S, Fig. 8 shows the phases of the 8-hr wind shear (squares) and the 8-hr E_S (circles). Note that the latter one is defined as the local time of maximum E_S probability, while the 8-hr shear phase is given as the time of maximum negative wind shear. The seasonal means from 2007 – 2010 were vector averaged and the standard deviation (shown as error bars) was calculated from the 4 years of seasonal mean data, thereby indicating interannual variability. This was carried out for each 7 km height interval, using a 3 km overlap. The reference height was taken as the centre of the interval. Significant phases (solid symbols) of the 8-hr shear generally occur between 86.5 km and 92.5 km, except for winter. In summer and autumn, also the lowest or uppermost gates, respectively, show significant values. In contrast to that, the 8-hr E_S phases reveal only a few significant values, which were observed around 113 km in spring and slightly above 100 km during winter. However, in autumn, significant values are al-

ways present in the height interval 100 – 113 km, suggesting the influence of the wind shear TDT on E_s .

Generally, the 8-hr E_s phases show the descent of the E_s layer with time. This is according to theory (Haldoupis et al., 2006), where E_s layers follow the phase velocity of the tides, but this is the case only above 100 km. In lower regions they slow down, due to the increasing ion-neutral gas collision frequency. A tendency for this can be seen in spring and summer, where the E_s phase is slightly bent around 100 km. A bending in autumn and winter is also weakly indicated, but it is, as is seen by the large error bars, not a regular feature. There are two reasons for these observations. On the one hand the GPS RO technique is not able to track a single E_s . Consequently, fine-scale characteristics like the bending can only be seen in spring and summer, when a sufficient amount of E_s data is available. Furthermore, at lower altitudes (<100 km) some phase shifts occur, e.g., in autumn 2010 at ~90 km (not shown here), or generally in spring at ~90-95 km resulting in strong differences with respect to the expected values. Note that those described phase shifts are evident in E_s and wind shear data.

The vertical wavelength of the 8-hr shear is short during spring (excluding the uppermost gate) and summer, but significantly longer during autumn and winter. This correlates with the behaviour of the TDT phases. However, the vertical wavelength of the TDT in E_s or wind shear is also dependent of the amplitude change with height therefore cannot be directly compared with the wind amplitude phase gradient.

Although the majority of measured 8-hr E_s amplitudes are insignificant, the general correspondence between the phases of 8-hr shear and 8-hr E_s gives additional confidence that we observed a real phenomenon and not an artefact. The closest agreement between the phase profiles is seen in summer, although the TDT activity is low. In contrast, during autumn the agreement is less strong, while the TDT amplitudes are large. In spring and summer, an overlapping between the phase profiles was observed, and the extrapolated 8-hr shear phases fit well with the 8-hr E_s phases in higher altitudes. Again, this is caused by the decreasing E_s rates below 100 km and the fact that the E_s phases are less strongly determined by the phases of the tides in these regions. Lower E_s rates are also a reason for the phase shifts in some altitudes.

4 Conclusions

The terdiurnal oscillations in the occurrence frequency of E_s were analysed based on the measurements of the FORMOSAT-3/COSMIC satellites. The performed GPS RO technique does not allow tracking of a single E_s , but information about the seasonal characteristics are available. Therefore, the 3-monthly running mean zonal means from December 2006 – November 2010 were used for constructing 4-year means. After removing the effect of the background E_s activity, we found that the seasonal cycle of the normalised amplitude of the 8-hr E_s is marked by two maxima during spring and autumn, while the latter one is dominating. This agrees well with the seasonal behaviour of the 8-hr amplitudes in wind and wind shear, which gives a strong indication for close physical connection between E_s and the TDT. We could also show that the 8-hr shear phases match the 8-hr E_s phases, which is the case especially when the E_s rates

are high. Therefore, the 8-hr E_S is also forced or at least significantly influenced by dynamics. Furthermore the clearest signature of the 8-hr shear is observed in autumn, correlating with the stronger TDT activity.

These qualitative correlations between the 8-hr signatures in E_S and wind/wind shear were not expected, because the 8-hr E_S oscillations based on zonal means, while the radar measurements of the wind field over Collm are affected by local phenomena. Therefore the results indicate that, according to wind shear theory, besides the well-known influence of the SDT also the TDT plays a role in the diurnal and seasonal cycle of E_S.

Acknowledgements

This study was supported by Deutsche Forschungsgemeinschaft under grant JA 836/22-1. We acknowledge UCAR (Boulder, U.S.) and NSPO (Taiwan) for the free provision of FORMOSAT-3/COSMIC data and related support. We also thank Falk Kaiser, Leipzig, for maintaining the radar measurements.

References

- Arras, C., 2010: A global survey of sporadic E layers based on GPS Radio occultations by CHAMP, GRACE and FORMOSAT-3 / COSMIC. PhD thesis, University of Leipzig, 127 p.
- Arras, C., Jacobi, C., Wickert, J., 2009: Semidiurnal tidal signatures in sporadic E occurrence rates derived from GPS radio occultation measurements at higher midlatitudes. *Ann. Geophys.*, 27, 2555–2563.
- Bishop, R.L., Earle, G.D., 2003: Metallic ion transport associated with midlatitude intermediate layer development. *J. Geophys. Res.*, 108, A11019, doi:10.1029/2002JA009411.
- CDAAC Team, 2012: <http://cdaac-www.cosmic.ucar.edu/cdaac/status.html>, last access: 26 June 2012.
- Fytterer, T., Jacobi, C., 2011: Climatology of the 8-hour tide over Collm (51.3°N, 13°E). *Rep. Inst. Meteorol. Univ. Leipzig*, 48, 23-32.
- Hagan, M.E., Forbes, J.M., Vial, J., 1995: On modeling migrating solar tides. *Geophys. Res. Lett.*, 22, 893–896.
- Haldoupis, C., Pancheva, D., 2006: Terdiurnal tidelike variability in sporadic E layers. *J. Geophys. Res.*, 111, A07303, doi:10.1029/2005JA011522.
- Haldoupis, C., Meek, C., Christakis, N., Pancheva, D., Bourdillon, A., 2006: Ionogram height-time-intensity observations of descending sporadic E layers at mid-latitude. *J. Atmos. Sol.-Terr. Phys.*, 68, 539-557, doi:10.1016/j.jastp.2005.03.020.

Haldoupis, C., Pancheva, D., Singer, W., Meek, C., MacDougall, J., 2007: An explanation for the seasonal dependence of midlatitude sporadic E Layers. *J. Geophys. Res.*, 112, A06315, doi:10.1029/2007JA012322.

Hocking, W.K., Fuller, B., Vandepoer, B., 2001: Real-time determination of meteor-related parameters utilizing modern digital technology. *J. Atmos. Sol.-Terr. Phys.*, 63, 155–169.

Jacobi, Ch., 2012: 6 year mean prevailing winds and tides measured by VHF meteor radar over Collm (51.3°N, 13.0°E). *J. Atmos. Sol.-Terr. Phys.*, 78-79, 8-18, doi:10.1016/j.jastp.2011.04.010.

Karami, K., Ghader, S., Bidokhti, A.A., Joghataei, M., Neyestani, A., Mohammadbadi, A., 2012: Planetary and tidal wave-type oscillations in the ionospheric sporadic E layers over Tehran region. *J. Geophys. Res.*, 117, A04313, doi:10.1029/2011JA017466.

Teitelbaum, H., Vial, F., Manson, A.H., Giraldez, R., Massabeuf, M., 1989: Non-linear interactions between the diurnal and semidiurnal tides: terdiurnal and diurnal secondary waves. *J. Atmos. Sol.-Terr. Phys.*, 51, 627–634.

Whitehead, J., 1961: The formation of the sporadic E layer in the temperate zones. *J. Atmos. Terr. Phys.*, 20, 49–58.

Wu, D.L., Ao, C.O., Hajj, G.A., de la Torre Juarez, M., Mannucci, A.J., 2005: Sporadic E morphology from GPS-CHAMP radio occultation. *J. Geophys. Res.*, 110, A01306, doi: 10.1029/2004JA010701.

Addresses of Authors

Tilo Fytterer: Now at Karlsruhe Institute of Technology, Institute for Meteorology and Climate Research

Christina Arras: German Research Centre for Geosciences GFZ, Potsdam, Department Geodesy & Remote Sensing, Telegrafenberg, 14473 Potsdam

Christoph Jacobi: Institute for Meteorology, Universität Leipzig, Stephanstr. 3, 04103 Leipzig

Final results of the DFG funded project “Development of a tomographic water vapour sounding system based on GNSS data”

Armin Raabe¹, Michael Bender², Jens Wickert²,

- 1) LIM Leipziger Institut für Meteorologie Univ. Leipzig Stephanstr. 3, 04103 Leipzig
2) Helmholtz Zentrum Potsdam GFZ, Telegrafenberg, 14473 Potsdam

Summary:

Since 2008 a group of scientists of the Leipzig Institute of Meteorology (LIM) and the German Research Centre for Geosciences Potsdam (GFZ) develops a method to derive water vapour profiles out of continuously available GNSS data (Global Navigation Satellite System).

The aim of this project - supported by the Deutsche Forschungsgemeinschaft (DFG) - was to develop a processing system with related scientific algorithms, which uses data of regional GNSS ground networks to derive 3D water vapour distributions above these stations. This systems use the line of sight water vapour information from each ground station to every GNSS satellite in view (slants) as basis of a 3D tomographic reconstruction.

At this time these reconstructions are based on GNSS data of about 330 German or near Germany located groundstations. This leads to a horizontal resolution of the reconstructed 3D water vapour field up to 40km and a vertical resolution of about 0.5km from the upper part of troposphere down to the atmospheric boundary layer (1km height).

Zusammenfassung:

Seit 2008 befasst sich eine Arbeitsgruppe von Wissenschaftlern am LIM und dem GFZ in Potsdam im Rahmen eines DFG-geförderten Projektes mit der Ableitung von dreidimensionalen Wasserdampfverteilungen in der Atmosphäre aus Beobachtungsdaten regionaler GNSS-Bodennetze (Globale NavigationsSatellitenSysteme). Die Wasserdampfverteilungen können aus der atmosphärischen Information entlang der Sichtlinien zwischen den Bodenstationen und den sichtbaren GNSS-Satelliten (sogenannte Slants) berechnet werden. Diese zahlreichen Sichtlinien ermöglichen eine tomographische Verarbeitung der Daten. Der entwickelte tomographische Algorithmus nutzt derzeit bis zu 330 deutsche und nahe Deutschland gelegene GNSS-Stationen, was eine horizontale Auflösung der resultierenden 3D-Felder von 40km und einer vertikalen Auflösung von 0,5km bis hinab zur atmosphärischen Grenzschicht (bis 1 km über dem Boden) ermöglicht.

1. Introduction

1.1. Motivation

The Global Positioning System (GPS) has nowadays many applications used in daily life. An increasing number of GPS applications requires dense networks of GPS ground receivers all over the world and induced the development of the European Galileo programme, the Chinese Compass programme as well as the renewal of the Russian GLONASS. Precise positioning applications of these GNSSs (Global Navigation Satellite Systems) require atmosphere corrections in order to remove the impact of the lower atmosphere and especially the water vapour on the GPS signal and the position. These corrections contain valuable information on the atmospheric state and are the basic input for several applications of theGNSS meteorology or GNSS atmosphere sounding.

The GNSS water vapour tomography makes use of the atmosphere corrections applied to each individual transmitter—receiver link (slant). Each signal path from a GPS satellite to a ground receiver “scans” a different part of the atmosphere and provides information integrated along the signal path. A very large number of such observations can be used to reconstruct the atmospheric state by means of tomographic techniques.

This project was started to set up a continuously running GPS based water vapour sounding system for Germany. Currently, about 270 German and 60 other GPS stations provide ~1.2 millions of observations per day, each covering a different region of the atmosphere. Humidity fields with a spatial resolution of about 40 km horizontally and several hundred meters vertically can be reconstructed from these observations every 15-30 minutes. The tomography system is now in a semi-operational state and can run in near real-time as part of the GPS processing system or be used to reconstruct user defined periods of time with various parameters. GPS slant delays are operationally available since 2007 and this large data set was used to obtain a large number of humidity fields which cover Germany and parts of adjacent countries. The results were validated using independent observations such as radiosonde profiles, the line of sight integrated water vapour observed by water vapour radiometers and analyses of numerical weather models.

1.2 Initial questions and objectives

GNSS observations provide information on the spatial distribution of water vapour in the atmosphere. Such information is essential for high resolution numerical weather models, now-casting or hydrological applications but can currently not be provided by any existing observation system. Therefore, several attempts have recently been made to reconstruct spatially resolved humidity fields from GNSS slant delay data by means of the GNSS tomography. Within this project a GNSS tomography system for Germany was developed which completes the existing GNSS processing system at the GFZ. Utilizing the operationally available slant observations of about 330 stations it was investigated if the quality of the slant data and the information provided by this kind of observations, i.e. quantities integrated along the signal paths, is sufficient to obtain reliable spatially resolved humidity fields for Germany. These questions are

closely related to the mathematics of inverse problems as an ill-posed inverse problem needs to be solved.

The first part of this project was related to GNSS data processing and quality assessment. The GNSS slant data are estimated by a rather complicated processing chain which provides no reliable error estimates (Gendt et. al, 2004). Validation with independent observation, e.g. from water vapour radiometers or analyses of numerical weather models, was therefore an important task.

In the second part the tomography software was extended in order to combine the slant delays with additional observations and to compare several reconstruction techniques. A large number of tomographic reconstructions with various combinations of parameters was carried out in order to investigate their impact on the results: Initialization, combinations of input data, the reconstruction algorithm, the spatial resolution of the grid, the temporal resolution, etc., can change the results considerably, especially as an inverse problem is solved which is very sensitive to small variations in the input data and the parameters.

The third task was to estimate the quality of the reconstructed humidity fields and to provide error estimates. This was done by comparing the results with radiosonde profiles and model analyses. Complementary information on the inversion quality could be obtained from the resolution matrix which provides a mathematical tool for validation. Reliable tools for quantifying the reconstruction quality would have been required to answer the questions in the previous paragraph.

Altogether, the potential of a future operational GNSS tomography system was to be assessed.

2. Results

2.1. GNSS data processing

The operational GNSS processing system running at the GFZ provides hourly files of zenith total delays (ZTD), the integrated water vapour (IWV), slant total delays (STDs) and other geodetic and meteorological products. An additional tool developed in the first phase of this project separates the slant hydrostatic delay (SHD) and the slant wet delay (SWD) and is also running operationally (Bender et. al, 2010)

Currently, about 330 stations are processed in near real-time (NRT), ~270 of them are located in Germany. These stations provide more than 1000 ZTD/IWV observations and 50000 – 60000 STD/SWD observations per hour. During this project 5 years (2007-2011) of NRT GPS data were processed and are now available for tomographic studies.

In parallel to this project the COPS data reprocessing was finished. The COPS/GOP GPS reprocessing covered the whole year 2007 and is up to now the largest dataset available, containing data from about 450 French and German stations including the densified network in the COPS region. (COPS, Convective and Orographically-induced Precipitation Study and its GOP (Global Observation Period) is reported in Crewell, et al 2008, see also <https://www.uni-hohenheim.de/cops/>)

The EPOS (Earth Parameter and Orbit Determination System) GNSS processing system is used at the GFZ. EPOS was developed at the GFZ and is continuously updated. The major improvements were described in the progress report (Ge et al., 2005). The quality of the meteorological EPOS products is operationally monitored

within the E-GVAP-project (EUMETNET GPS Water Vapour Programme). Comparisons with other processing centers and the HIRLAM weather model (<http://www.hirlam.org>) can be found on the E-GVAP webpage: <http://egvap.dmi.dk>.

2.2. Validation of slant delays

The validation of slant delays, i.e. the signal delay along the path from the GPS satellite to the GPS receiver, is a demanding task as very little observations are available: Most observation systems are not aligned to a certain GPS satellite and do not provide slant delays. It is therefore necessary to interpolate or project the available observations on the satellite-receiver axis and to convert between different physical quantities. This has been done in the water vapour radiometer (WVR) validation studies.

Another approach is to use analyses of numerical weather models which provide all information necessary to compute the different contributions to the slant delays:

Of the moisture (Slant Wet Delays, SWD)

Of the hydrostatic dry atmosphere (Slant Hydrostatic Delay, SHD)

Or to the sum of these (Slant Total Delay, STD).

However, the signal path through the model field is not known but must be estimated from the refractivity field between the satellite and receiver position. First studies with COSMO fields (Bender et al., 2008) showed that the slant delays are systematically overestimated at lower elevations if a straight path is assumed. The real bended signal path can be estimated by using Fermat's Principle, e.g. using a variational approach. Such a raytracer (Zus et al., 2012) was applied to ECMWF analyses of several years and used to estimate a huge amount of slant delays for the German GPS stations (Brecht et al., 2011). For COSMO (Consortium for Small-scale Modeling) see <http://www.cosmo-model.org>.

2.3. Validation using water vapour radiometers

A WVR with satellite tracking capabilities was acquired by the GFZ in order to obtain WVR observations exactly along the satellite-receiver axes. The radiometer is now available but, unfortunately, it was not possible to take a sufficient number of observations and to analyse the data before the end of this project.

Therefore, the analysis of the COPS observations provided by the University of Cologne was used.

In the first part of the project (Progress Report, 2009) GPS and WVR observations were compared only if they coincide both in time and direction, i.e. azimuth and elevation. With these criteria only between ~4000 and ~10000 SWV observations could be compared within three months, i.e. 30-100 observations per day at different elevations. Another approach was therefore chosen which utilizes the information provided by the continuous radiometer hemisphere scans. Assuming that the atmosphere does not change significantly within the 10 minutes required to perform a full hemisphere scan the WVR observations can be interpolated on the GPS SIWV (Slant Integrated Water Vapour). Using a linear interpolation within observations neighbored in time, azimuth and elevation, about 230000 SIWV observations could be compared which is approximately 50 % of all GPS observations available. This large

data set was analysed in order to identify possible deficiencies in the GPS slant processing strategy. The GPS and WVR data agree in general very well: Regarding all data a bias of 0.4 kg m^{-2} was found indicating that the WVR detects somewhat more humidity than GPS. The standard deviation is 1.9 kg m^{-2} , increasing from 1.3 kg m^{-2} near the zenith up to 3.0 kg m^{-2} at lower elevations between 14.4° and 25.2° . The relative difference is almost constant with a slightly falling trend at lower elevations. Regarding the uncertainties due to the STD→SIWV conversion and the interpolation of the WVR data which add to the original STD observation error this indicates that the quality of the GPS observations is increasing with decreasing elevations.

The comparison described above was repeated for different methods to separate the SWD from the STD in order to find the best strategy. It turned out that the method suggested by Runge et al. 1996 leads to the best agreement for the whole period.

In further studies the correlation of the GPS-WVR differences with the atmospheric humidity and atmospheric gradients as detected by the WVR azimuth scans was investigated. No such correlations could be found. However, the time series of GPS and WVR observations show periods of nearly identical observations followed by periods of large and almost constant differences. So far no correlations with pressure, temperature or relative humidity could be found and further investigations would be required.

2.4. Validation using weather model analyses

The European Centre for Medium-Range Weather Forecasts (ECMWF) provides model analyses every 6 hours at 0, 6, 12, 18 UTC. Four years (2007-2010) of these analyses were used to validate the corresponding STD observations from the German GPS stations. A raytracer was used to estimate the bended signal path through the model atmosphere for each observed STD (Zus et al., 2012) and the model STD was computed by integrating the refractivity along this curve. The differences between the observed and model STDs were analysed in various ways: Statistics for each whole year, seasonal statistics, day-night comparisons, daily and monthly statistics, etc., were computed. A typical result for the month August is shown in Fig. 2. The bias between model and observations is small and almost independent from the elevation, the standard deviation σ increases with decreasing elevations but the relative σ is almost constant. The latter is a very important result for the GPS tomography: The error per unit length or the error per grid cell is almost constant if the relative σ is not varying with elevation and the uncertainty of the tomographic reconstruction is not affected by using STDs at low elevations. The absolute numbers of the bias and σ vary somewhat for different months or days but in general model and observations agree very well (Zus et al., 2012, Deng et al., 2011).

These results also indicate that the assimilation of STDs into numerical weather models could have a positive impact on weather forecasts. Especially slants at low elevations should provide information on the vertical humidity structure.

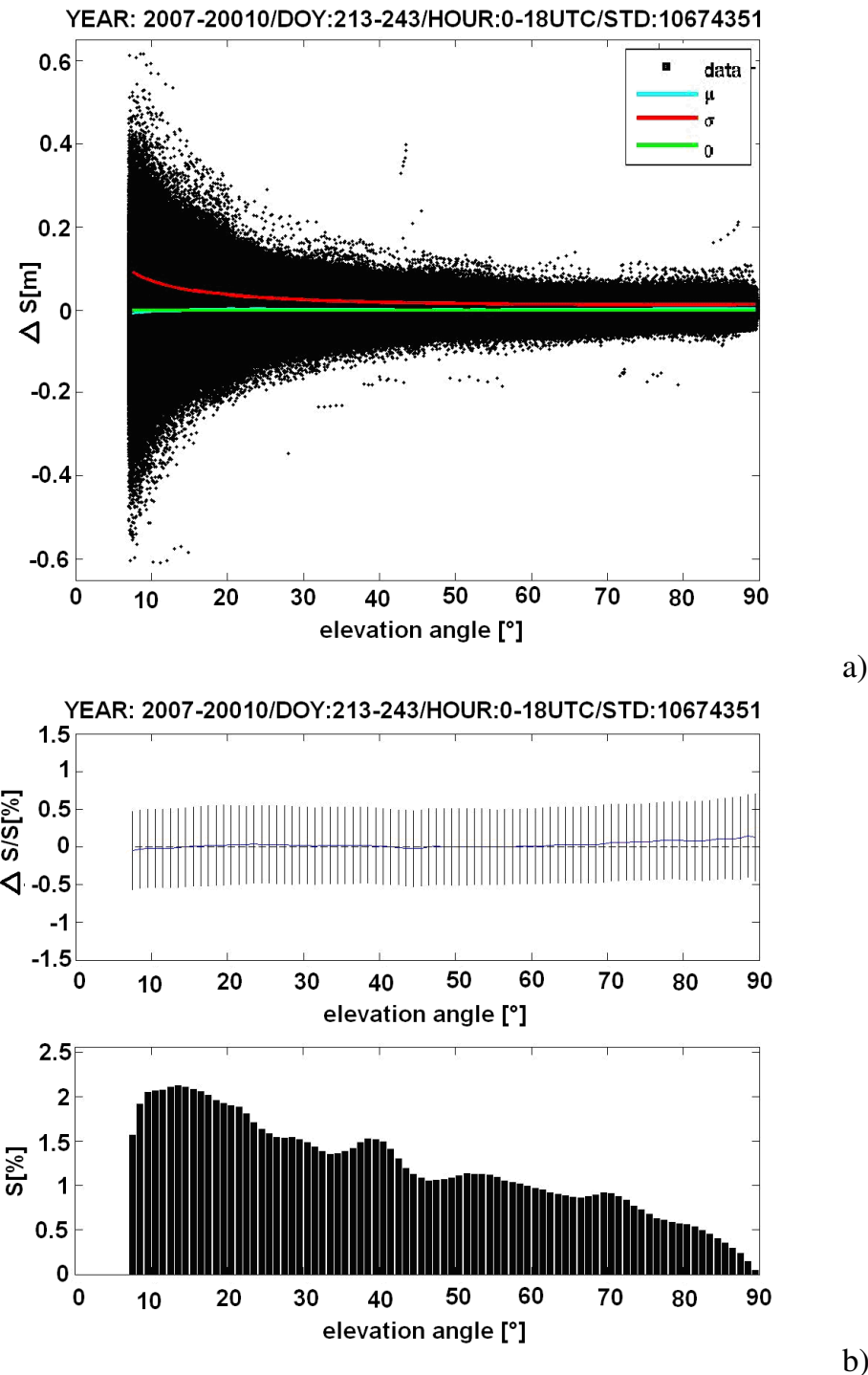


Fig. 1: Differences between observed and computed STDs for the month August in the years 2007-2010. The absolute STD differences in meters for about $10 \cdot 10^6$ slants observed within the 4 months (a) show an almost constant bias for all elevations and a standard deviation increasing from ~ 10 mm near the zenith up to ~ 80 mm at an elevation of 7° . The relative standard deviation in % (b, top) is almost constant 0.5 % at all elevations. The GPS satellite constellation leads to very few STDs near the zenith but an increasing number of observations at lower elevations (b, bottom).

2.5. Tomography

During this project a quasi-operational GPS tomography system was developed and tested (Bender et al., 2011). The tomography system was designed to reconstruct spatially resolved fields of the refractivity N , the wet refractivity N_{wet} (shown also in Fig. 2) or the absolute humidity from a large number of STDs, SWDs or SIWVs, respectively. The numerical solution requires a spatial grid which can be adapted to dimensions of the GPS network and defines the spatial resolution of the reconstruction. Several techniques were implemented to solve the ill-posed inverse problem: Several modifications of the algebraic reconstruction techniques (ART) are available to solve the large set of linear equations iteratively, e.g. MART, DART, SIRT (Subbaro et al., 1997). A damped weighted least-squares solution (Tarantola, 2005) was implemented which is basically matrix algebra but is complicated by the large sparse matrices which have to be inverted. A third option is a Kalman filter. Additional observations can be used to stabilize the inversion: Point observations such as synoptic data, profiles provided e. g. from water vapour radiometers or radiosondes or integrated observations like WVR-SIWV data or GPS-IWV data. The tomography can be initialized in different ways: Simple exponential profiles, standard atmospheres, horizontally interpolated and vertically extrapolated synoptic data (Troller et al., 2006), COSMO analyses/forecasts or the previous inverted field can be loaded. The tomography software was supplemented with several tools for visualizing the STD data entering the tomography and the reconstructed humidity fields, for monitoring the reconstruction process and for simulating STD data based on satellite orbits, station coordinates and fields provided by numerical weather models (COSMO, ECMWF).

The above mentioned reconstruction techniques can be used with different parameters: The initialization, different combinations of input data, the reconstruction algorithm, the spatial resolution of the grid, the temporal resolution, etc., was varied systematically. A large number of reconstructions was carried out for the subsequent validation studies. One set of reconstructions was based on a limited number of reference data and epochs resulting in one humidity field for each parameter set. These humidity fields should be rather similar and can easily be compared. Another set was computed for long time series up to one month consisting of 700 – 3000 single fields. These data were used to investigate the temporal variations of the reconstruction quality and to test the behavior of a future operational tomography system. The results were investigated carefully: After a first visual inspection a validation with radiosonde (RS) profiles was started.

Almost all results belong to two categories:

- 1) The inversion process is divergent and the results are obviously useless.
- 2) The inversion converges and leads to reasonable humidity fields with some artifacts.

Unfortunately, no results were found which were clearly superior. In the 2. case it was very difficult to quantify the reconstruction quality of the whole 3D fields. Lots of different parameters lead to results of comparable quality and it was almost impossible to identify an optimal combination of parameters. A simulation study (Bender et al., 2011) was started in order to eliminate the impact of observation errors and to have a reference field for the validation. Furthermore, GLONASS and Galileo observations

were also simulated for investigating the impact of additional GNSS. Even with the reference field being available it was difficult to estimate the reconstruction quality. A different approach was to compute the resolution matrix which provides more insight to the inversion process. The approximate data resolution matrix (influence matrix, hat matrix) could be computed from the intermediate results of the ART algorithms. This matrix describes the impact of individual observations on the result. Some influence matrix properties could be computed, e.g. the global observation influence which describes the impact of the observations with respect to the background impact (background = initialization). It was found that the impact of the observations is between 80% and 90%. More interesting would be the model resolution matrix which describes how a hypothetical true state is mapped to the estimated state by the kernel matrix. The estimated state parameters are a weighted function of the true state parameters and the model resolution matrix describes what can be expected in an ideal case if a certain kernel matrix is given. To compute the model resolution matrix the generalized inverse is required. Unfortunately, this is not computed by the inversion algorithms and approximate solutions are required. It turned out that this task is equally demanding as the inversion itself. Attempts were made to obtain approximate solutions but the results were rather instable and much more work would be required to finish this task.

2.6. Validation of tomographically reconstructed humidity fields

The validation of tomographically reconstructed humidity fields with independent observations is not only required to estimate the errors of the results: To decide which set of parameters leads to the best tomographic reconstruction it is necessary to quantify the quality of different results. Therefore a set of radiosonde (RS) profiles observed by the 12 operational German RS stations in 2007 was compared with the corresponding tomographically reconstructed profiles. Tomographic reconstructions were generated for each day of the year at 0:00 UTC and 12:00 UTC in order to provide tomographically reconstructed data for each RS profile. As the spatial grid used by the tomography had a rather small horizontal resolution of 30 – 50 km the grid columns were interpolated to the RS station coordinates. In total two sets of 6803 profiles at 12 stations were available for the comparison. The details of the validation study can be found in Shangguan, et al., 2013.

2.6. Complexity of quality assessment

After a first analysis of different comparisons it turned out that the quality of the humidity fields could not be quantified in a consistent manner. A standard statistical analysis providing, e.g., mean differences and their standard deviations, leads to rather meaningless results. These quantities look rather promising if a sufficiently large number of profiles are compared but they are not really significant if the observations are taken from profiles which do not represent the real vertical structure of the atmosphere. The same is true for error estimates computed for specific altitude intervals.

It was therefore necessary to compare entire profiles instead of isolated observations at different altitudes. Several parameters were defined to identify similar profiles and to quantify the degree of similarity. With this strategy it was possible to identify a subset of rather similar profiles and another subset of obviously deviating profiles. Unfortunately, there remains a majority of profiles which show sequences of good agreement together with severe discrepancies. A visual inspection of the profiles shows at least two types of problems:

- 1) The tomography tries to modify the initial profiles in order to minimize the discrepancies but the STD observations are insufficient to finish this process. The result is a combination of the initial profile and partial distortions by the observations.
- 2) Another class of profiles shows rather strong artifacts at different altitudes leading to unreliable profiles.

Both problems are related to the sparse observations which are used to solve an ill-posed inverse problem. To summarize, it was not possible to develop a validation tool which was sensitive and reliable enough to distinguish between tomographic reconstructions obtained with different parameter sets.

First tests with profiles or horizontal layers taken from numerical weather models (COSMO, ECMWF) lead to similar or even more severe problems as more observations were available. It was therefore decided to concentrate on the RS validation study.

Detailed results of the quality assessment with RS observations are given in Shangguan et al., 2013. To summarize, the results of this validation study show that the tomographic inversion is able to provide reliable profiles with some minor artifacts as long as sufficient STD observations are available. In cases of insufficient observations the results become unpredictable and are in many cases worse than the initial profiles. It must be pointed out that the observations regarded here as „sufficient“ are in general not anywhere near the quality usually required by tomographic methods. In general each voxel must be observed from a wide angular range but in case of GPS tomography even the best profiles are based on very incomplete data with lots of empty voxels and other voxels observed only from very few narrow angles.

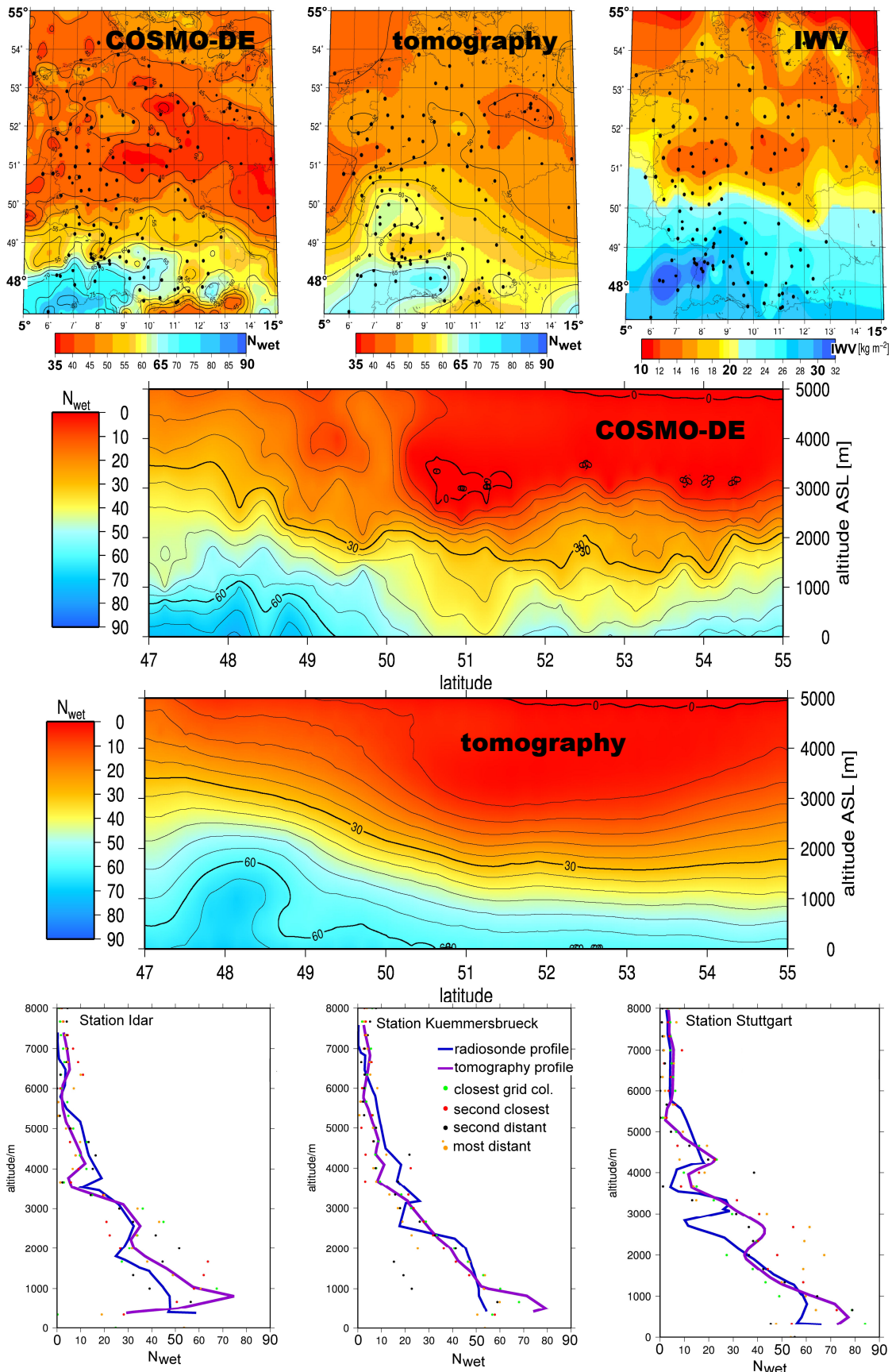


Fig. 2: 8.7.2007, 12:00 UTC – Results of the tomographic reconstruction (using N_{wet}), horizontal layer at 676 m (top), vertical slice (center) and comparison with radiosonde profiles (bottom). COSMO-DE fields and radiosonde profiles are shown.

Regarding the rather limited number of observations which already leads to profiles of good quality the results of this study are very promising. These results are based on parts of the humidity fields which are really a result of the tomography. Regions with no observations or very few STD data were separated and not used in the validation study. The criteria defining regions with almost no observations, regions of insufficient data and regions of presumably sufficient data can later be extended to confidence parameters which can be provided together with the tomographically reconstructed humidity fields.

3. Outlook

The results of this project demonstrate that slant total delays (STDs) provided by GNSS processing systems contain valuable information about the spatial water vapour distribution in the atmosphere. The realized STD validation studies show that GNSS STDs and similar observations from other observation systems correspond within the errors of both systems. However, regarding specific stations or special periods of time there are also discrepancies and the processing of STDs could be improved.

The validation showed that the GPS observations present sufficient information to reconstruct 3D humidity fields of good quality as long as all parts of the atmosphere are “scanned” by GPS signal paths. Currently, this is the case only for limited regions and periods. The number and distribution of GPS observations does not yet cover all parts of Germany at all times. Rather large unobserved regions affect the quality of the results and more stations and satellites would be required by an operational GPS tomography system.

The number of satellites is already increasing as GLONASS, Compass and Galileo will soon be available. Beyond that attempts must be made to densify the GNSS networks as the resolution of the reconstructed humidity fields is limited by the interstation distances.

The validation of the tomographically reconstructed humidity fields shows that the currently available STD data and inversion algorithms are not yet sufficient to guarantee stable and reliable results. None of the techniques so far used in the field of GNSS tomography leads to superior results. Equally important as the reconstruction algorithm is the exact form of the forward operator. The results could be improved by replacing a simple operator based on voxels of constant refractivity by a smoothing operator which interpolates the refractivity on the signal path. The smoothing operator does not only lead to better humidity fields but has also a stabilizing effect on the whole inversion procedure.

The reasons for the somewhat ambiguous results are obvious: A visualization of the slant paths in the atmosphere clearly shows that there are at all times large parts of the atmosphere which are not covered by any observations. For geometrical reasons this is especially true for parts of the lower atmosphere up to altitudes of ~3 km. The basic requirements of a stable tomographic reconstruction are therefore not satisfied and the quality shows considerable temporal and spatial variations. Under these conditions the results are surprisingly good.

To improve the results two different strategies should be followed:

- 1) More data are required which cover all parts of the atmosphere more homogeneously.
- 2) Advanced adaptive inversion strategies need to be developed which can deal with the highly variable GNSS observations.

More GNSS satellites will be available in near future: GLONASS observations are already available, Compass and Galileo observations will follow in the next 5 years, leading to more than 100 GNSS satellites. However, more dense GNSS networks would also be required, especially to improve the situation in the lower part of the atmosphere but also to increase the resolution of the reconstructed fields which is limited to approximately the mean station distance. Within this project the data available from existing geodetic stations were utilized. In order to obtain nationwide 3D humidity fields with a quality comparable to existing humidity profilers or radiosondes efforts must be made to extend the GNSS networks for meteorological applications. This could lead to a unique humidity observation system with a much higher spatial resolution than any existing system and with real-time capabilities.

Advanced inversion strategies to retrieve optimal information from the available STD data and to provide reliable error estimates need to be developed in cooperation with mathematicians specialized on inverse problems. Adaptive techniques have been proposed which transform the given inverse problem into an optimal form which can be solved in the best way.

List of publications resulting from this project

Behrendt, A., et al., 2011: Observation of convection initiation processes with a suite of state-of-the-art research instruments during COPS IOP 8b, *Quarterly Journal of the Royal Meteorological Society*, Vol. 137, 81-100

Bender, M., Dick, G., Wickert, J., Schmidt, T., Song, S., Gendt, G., Ge, M., and M. Rothacher, 2008: Validation of GPS Slant Delays using Water Vapour Radiometers and Weather Models, *Meteorologische Zeitschrift*, 17(6): 807-812

Bender, M., G. Dick, G., Wickert, J., Ramatschi, M., Ge, M., Gendt, G., Rothacher, M., Raabe, A., and G. Tetzlaff, 2009: Estimates of the information provided by GPS slant data observed in Germany regarding tomographic applications, *Journal of Geophysical Research*, 114: Doi06303

Bender, M., Stosius, R., Zus, F., Dick, G., Wickert, J., and A. Raabe, 2011: GNSS water vapour tomography – Expected improvements by combining GPS, GLONASS and Galileo observations, *Advances in Space Research*, Vol. 47, No. 5, 886-897

Bender, M., Dick, G., Ge, M., Deng, Z., Wickert, J., Kahle, H.-G., Raabe, A. and G. Tetzlaff, 2010: Development of a GNSS Water Vapor Tomography System Using Algebraic Reconstruction Techniques, *Advances in Space Research*, Vol. 47, No. 10, 1704-1720

Brecht, B., Raabe, A., Bender, M., 2010: Comparison of refractivity profiles derived by Radiosonde soundings and GNSS tomography. *Wiss. Mitteil. Inst. f. Meteorol. Univ. Leipzig*, 48, 13-22

Chen, J., Bender, M., Beyerle, G., Dick, G., Falck, C., Ge, M., Gendt, G., Heise, S., Ramatschi, M., Schmidt, T., Stosius, R. and J. Wickert , 2009: GNSS Activities for Natural Disaster Monitoring and Climate Change Detection at GFZ. Oral presentation at EOGC 2009, Chengdu, China. , 25-29 May 2009, full paper published in the conference proceedings.

Crewell, S., et al. ,2008: The general observation period 2007 within the priority program on quantitative precipitation forecasting: Concept and first results, *Meteorologische Zeitschrift*, 17(6): 849-866

Deng, Z., Bender, M., Zus, F., Ge, M., Dick, G., Ramatschi, M., Wickert, J.. Löhner, U. and S. Schön, 2011. Validation of tropospheric slant path delays derived from single and dual frequency GPS receivers, *Radio Science*, Vol. 46, RS6007.

Deng, Z., Bender, M., Dick, G., Ge, M., Wickert, J., Ramatschi,, M. and X. Zou, 2009: Retrieving Tropospheric Delays from GPS Networks Densified with Single Frequency Receivers, *Geophysical Research Letters*, Vol. 36, L19802

Eichler, K. ,2009: Untersuchung von atmosphärischen Einflüssen auf simulierte GPS-Laufzeitverzögerungen, Diplomarbeit, Universität Leipzig

Eichler, K., M. Bender, M., Raabe A., 2009: Untersuchung des Einflusses atmosphärischer Strukturen auf GPS-Laufzeitverzögerungen, *Wiss. Mitteil. Inst. f. Meteorol. Univ. Leipzig*, 45, 99-113

Progress Report, 2009: Development of a tomographic water vapour sounding system based on GNSS data; Universität Leipzig Institut für Meteorologie; Helmholtz Centre Potsdam German Research Centre for Geosciences, 18p.

Van Baelen, J., Reverdy, M., Tridon, F., Labbouz, L., Dick, G., Bender, M. and M.. Hagen, 2011: On the relationship between water vapour field evolution and the life cycle of precipitation systems, *Quarterly Journal of the Royal Meteorological Society*, Vol. 137, 204-223

Shangguan, M., Bender, M., Ramatschi, M., Dick, G., Wickert, J., Raabe A., R. Galas, R., 2013: GPS Tomography: Validation of Reconstructed 3D Humidity fields with Radiosonde Profiles, *Annales Geophysicae*, submitted

Spänkuch, D., Güldner, J., Steinhagen, H. and M. Bender, 2011: Analysis of a dryline-like feature in northern Germany detected by ground-based microwave profiling, *Meteorologische Zeitschrift*, Vol. 20, 409-421

Zus, F., Grzeschik, M., Bauer, H.-S., Wulfmeyer, , V., Dick, G. and M. Bender, 2008: Development and optimization of the IPM MM5 GPS slant path 4DVAR system, *Meteorologische Zeitschrift*, 17(6): 867-885

Zus, F., Bender, M., Deng, Z.,Dick, G., Heise S., Shangguan M. and J. Wickert, 2012: A methodology to compute GPS slant total delays in a numerical weather model, *Radio Science*, Vol. 47, RS2018.

References

- Bevis, M., Businger, S., Chiswell, S., Herring, T.A., Anthes, R.A., Rocken, R., Ware, R. H., 1994: GPS Meteorology: Mapping Zenith Wet Delays onto Precipitable Water, *Journal of Applied Meteorology*, 33(3), 379-386
- Boehm, J., Niell, A., Tregoning, P. and H. Schuh, 2006: Global Mapping Function (GMF): A new empirical mapping function based on numerical weather model data, *Geophysical Research Letters*, 33, L07304
- Ge, M., Gendt, G., Dick, G., Zhang, F.P. and C. Reigber, 2005: Impact of GPS satellite antenna offsets on scale changes in global network solutions, *Geophysical Research Letters*, 32, L06310
- Gendt, G.; Dick, G.; Reigber, C.; Tomassini, M.; Liu, Y., and M. Ramatschi, 2004: Near Real Time GPS Water Vapor Monitoring for Numerical Weather Prediction in Germany, *Journ. Met.Soc. Jap.*, 82, 361-370
- Ha, S.-Y., Kuo, Y.-H., Guo, Y.-R. and G.-H. Lim, (2003): Variational Assimilation of Slant-Path Wet Delay Measurements from a Hypothetical Ground-Based GPS Network. Part I: Comparison with Precipitable Water Assimilation, *Monthly Weather Review*, 131(11), 2635-2655
- Runge, T.F., Bar-Sever, Y., Franklin, G.W., Kroger, P.M. and U. J. Lindqwister, 1996: Data, Site, and Network Requirements for GPS-based Sensing of Precipitable Water Vapor, *JPL*, 1996, 6p. (<http://hdl.handle.net/2014/24750>)
- Subbarao, P. M. V., Munshi, P. and K. Muralidhar, 1997: Performance of iterative tomographic algorithms applied to non-destructive evaluation with limited data, *NDT & E International*, 30, 359-370
- Tarantola, A., 2005: Inverse Problem Theory and Methods for Model Parameter Estimation, Siam, 358P.
- M. Troller, M., A. Geiger, A., E. Brockmann, E., Bettems, J.-M., Bürki, B. and H.-J. Kahle, 2006: Tomographic determination of the spatial distribution of water vapour using GPS observations, *Advances in Space Research*, 37, 2211-2217
- Van der Marel, H., Gündlich, B., 2006: Slant Delay Retrieval and Multipath Mapping Software, *TOUGH Deliverable D33*, Delft University of Technology, <http://web.dmi.dk/pub/tough/>
- Vedel, H., (ed.), 2006: Targeting Optimal Use of GPS Humidity Measurements in Meteorology, *TOUGH Final Report*, <http://web.dmi.dk/pub/tough/>

Retrieval of Cirrus Optical Thickness and Assessment of Crystal Shape from Ground-Based Imaging Spectrometry

M. Schäfer, E. Bierwirth, A. Ehrlich, F. Heyner and M. Wendisch

Abstract

An imaging spectrometer (AisaEAGLE) is applied for ground-based measurements of downward spectral radiance fields with high spatial (1024 spatial pixels within 36.7° field of view), spectral (488 spectral pixels, 400-970 nm, 1.25 nm full width at half maximum) and temporal (4-30 Hz) resolution. The calibration, measurement, and data evaluation procedures are introduced. A method is presented that retrieves the cirrus optical thickness τ_{ci} using the spectral radiance data collected by AisaEAGLE. On the basis of four measurement cases during the second campaign of the Cloud Aerosol Radiation and tuRbulence of trade wInd cumuli over BArbados (CARRIBA) project in 2011 the spatial inhomogeneity of the investigated cirrus is characterized by the standard deviation of the retrieved τ_{ci} , as well as the width of the frequency distribution of the retrieved τ_{ci} . By comparing measured and simulated downward solar radiances as a function of scattering angle, a first estimation of the detected cirrus ice crystal shape is given and used in the retrieval of τ_{ci} .

Zusammenfassung

Ein abbildendes Spektrometer (AisaEAGLE) wurde bodengebunden zur Messung von Feldern abwärts gerichteter spektraler Strahldichten mit hoher räumlicher (1024 Raumpixel auf 36.7° FOV), spektraler (488 spektrale Pixel, 400-970 nm, 1.25 nm FWHM) und zeitlicher (4-30 Hz) Auflösung verwendet. Die Kalibrierungsprozedur, das Messverfahren sowie die Datenauswertung werden hier vorgestellt. Weiter wird eine Methode zur Ableitung der Zirrus optischen Dicke τ_{ci} unter Verwendung dieser bodengebundenen spektralen Strahldichtedaten vorgestellt. Auf der Grundlage von vier Messzeiträumen während der zweiten Kampagne des Cloud Aerosol Radiation and tuRbulence of trade wInd cumuli over BArbados (CARRIBA) Projektes in 2011 wird die räumliche Inhomogenität der untersuchten Zirren durch die Standardabweichung der abgeleiteten τ_{ci} , wie auch der Breite ihrer Häufigkeitsverteilungen charakterisiert. Vergleiche der gemessenen Strahldichten mit Simulationen abwärts gerichteter solarer Strahldichten als Funktion der Streuwinkel ermöglichen eine erste Abschätzung der Eiskristallform im detektierten Zirrus und gehen in die Ableitung der τ_{ci} ein.

1. Introduction

Satellite-derived cirrus cloud climatology includes cloud cover, optical thickness, and crystal effective radius. Changing either of those parameters may change the magnitude of their radiative forcing. For example, in current global circulation models a standard value of 25 µm for ice crystal effective radius is assumed. For slightly smaller crystals, cirrus clouds would have a stronger cooling effect (Garrett et al., 2003). However, cirrus clouds often show a high spatial and temporal variability and in addition might be optically thin. This partly makes it hard to detect cirrus by common remote sensing techniques. The microphysical composition adds a further complication. Depending on crystal shape, the cloud radiative properties may vary substantially and cause biases in both satellite retrievals (based on reflected radiance, Eichler et al., 2009) and the energy budget (related to irradiance, Wendisch et al., 2005, 2007).

Passive satellite imaging spectroradiometers used for cloud retrievals measure the radiance field emerging from clouds. The applicability of those data for remote sensing is limited by radiative smoothing and other 3D effects, but also by the limited number of wavelength bands and spatial resolution of the sensor. A second source of uncertainty in cirrus retrievals arises from the forward simulation applied within the retrieval algorithm. In the special case of ice clouds, assumptions about the crystal shape and the corresponding scattering properties are made. Eichler et al. (2009) showed that these assumptions can add an uncertainty of up to 70% and 20% in optical thickness and effective radius, respectively. A way to check the retrieval algorithms with respect to both horizontal cloud heterogeneity and resolution and to crystal shape is provided by flying airborne versions of spectroradiometers above cirrus clouds, such as the MAS (MODIS Airborne Simulator).

Along with extensive microphysical and solar radiation instruments as well as radiative transfer simulations Schmidt et al. (2007) and Eichler et al. (2009) investigated the differences between retrieved and measured microphysical cloud properties. Schmidt et al. (2007) revealed large gaps between retrieved effective radius from MAS and simultaneous in situ measurements. This disagreement is probably related to the often discussed enhanced absorption and has not been resolved yet, partly because it has been extremely difficult to collocate remote sensing above the clouds and concurrent in-cloud microphysical measurements. Such experiments are extremely important to link satellite cloud observations of coarse resolution to spatially highly resolved measurements of cloud properties. Unfortunately, such experiments are rare, partly because instruments like MAS are very complex and expensive and are not available for frequent cloud experiments.

Furthermore, the modeling of cirrus inhomogeneities has to be improved. There are only very few cloud-resolving model studies on cirrus inhomogeneities, with regard to the radiative impact on the structure of cirrus clouds (Dobbie and Jonas, 2001), turbulence effects (Liu et al., 2003), or shear instabilities (Marsham and Dobbie, 2003). For a realistic simulation a high spatial and temporal resolution is required to represent the small scale features of cirrus inhomogeneities. In this regard, ground-based imaging spectrometers are a helpful tool to provide information on the cirrus heterogeneity in terms of field of radiance and cirrus optical thickness.

Within this study a ground-based spectral imager (AisaEAGLE Hanus et al., 2008) is applied to measure downward spectral radiance fields with high spatial (1024 spatial pixels within 36.7° field of view, FOV), spectral (488 spectral pixels, 400-970 nm, 1.25 nm full width at half maximum, FWHM) and temporal (4-30 Hz) resolution. Commonly AisaEAGLE is used for airborne observations of the Earth's surface and upward spectral radiance. In this paper AisaEAGLE is applied on the ground to measure downward solar radiances. In Section 2 the AisaEAGLE is technically characterized and its calibration and data evaluation procedures are described and exemplified. Section 3 introduces a new method to retrieve the cirrus optical thickness (τ_{ci}) from spectral radiance data, which also uses angular sampling of the phase function to obtain information about the particle shape. Its application to measurements is presented in Section 4.

2. Measurements of Spectral Radiance Fields

2.1 Campaign and Measurement Site

In April 2011, directional and spectral measurements of downward solar radiance were performed with the spectral imager AisaEAGLE on Barbados during the second campaign of the Cloud Aerosol Radiation and tuRbulence of trade wInd cumuli over BArbados (CARRIBA) project (Siebert et al., 2012). The aim of CARRIBA was to investigate microphysical and radiative processes within and next to shallow trade wind cumuli by helicopter-borne and ground-based observations (e.g., Werner et al., 2012). However, also cirrus clouds have frequently been observed by the ground-based instrumentation.

During the CARRIBA project in 2011, the imaging spectrometer AisaEAGLE was located in the Barbados Cloud Observatory (BCO) of the Max Planck Institute for Meteorology (Hamburg, Germany) at Deebles Point (13.15° N, 59.42° W), a cape at the east coast of Barbados.

Additionally, measurements with a Raman LIDAR and a cloud RADAR as well as radiosonde launches are available. See Siebert et al. (2012) for a more detailed description of the BCO. In parallel to the AisaEAGLE radiance measurements, all-sky images were collected every 15 seconds to receive information about the cloud situation (cloud coverage, cloud type, heading).

Downward spectral radiance was measured under inhomogeneous cloud cover on 14 different days. Each day, two hours of data were collected coordinated with the helicopter-borne measurements. In the following, four cases with measurements below cirrus and without low cumuli clouds were evaluated.

2.2 Imaging Spectrometer AisaEAGLE

The AisaEAGLE is a commercial imaging spectrometer which is manufactured by Specim Ltd. in Finland (Hanus et al., 2008). It is a single-line sensor with 1024 spatial pixels. The instrument measures radiances in three dimensions: space, time, and wavelength. The spatial and spectral dimensions are resolved by a special set of optics that displays the image onto a two-dimensional (2D) sensor chip. The third dimension, time, corresponds to the motion of the clouds passing over the sensor. An optical

schematic for the path of the electromagnetic radiation detected by the center spatial pixel is shown in Figure 1.

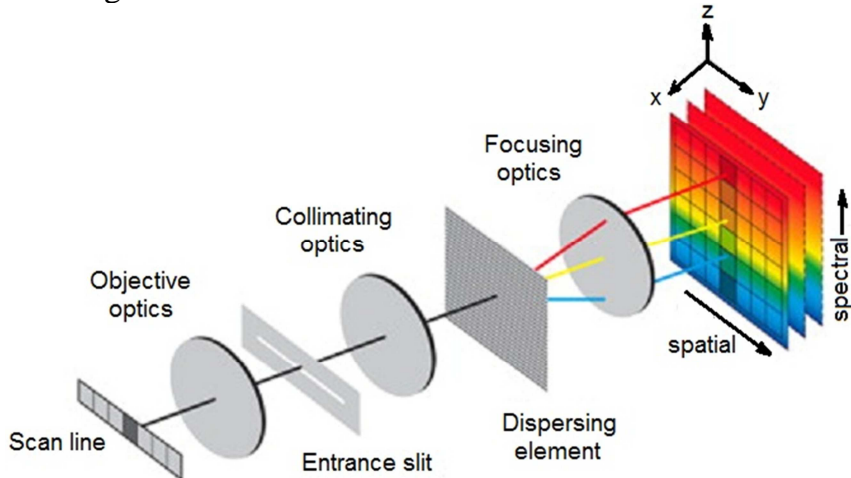


Fig. 1: Optical scheme of an imaging spectrometer. The figure is adapted from DellEndice et al. (2009).

The incoming solar radiation within the field of view (FOV) of AisaEAGLE is collected by a lens and an entrance slit. A collimating optics direct the radiation to a grating (dispersing element) where it is split into its spectral components. The spectral components are focused on the detector which consists of a charge-coupled device (CCD) element for the spatial and spectral dimensions.

In contrast to airborne measurements (Bierwirth et al., 2012), the 2D image evolves from the cloud movement and not from the sensor movement. The sensor was aligned perpendicularly to the direction of the cloud movement, thus 2D images of clouds with high spatial resolution are obtained. The FOV of the AisaEAGLE depends on the lens that is used for the measurements. During the CARRIBA project in 2011, a lens with an opening angle of about 36.7° was mounted.

While the swath increases with distance to the cloud by the tangent of the opening angle, the pixel size depends on its position on the sensor line. The FOV of a pixel (pixel width) in the center (viewing zenith) is smaller than that of a pixel at the edge. The "time" dimension of the spectral data set also translates to a spatial quantity: the length l_{pixel} of the FOV of a pixel is the product of the perpendicular cloud velocity v_{cloud} and the selected integration time t_{int} for the measurement. Considering additionally for a non-perfect perpendicular orientation with the angle α between the flow direction of the cirrus and the orientation of the sensor line, l_{pixel} is then given by:

$$l_{\text{pixel}} = |\sin \alpha| \cdot v_{\text{cloud}} \cdot t_{\text{int}} \quad (1)$$

Figure 2 illustrates the measurement geometry which is needed to derive the detected scattering angles ϑ for each spatial pixel. The scattering angle ϑ is derived by the scalar product between the vector of the incoming solar radiation (SC) and the vector of the radiation scattered into the sensor direction (CD):

$$\cos \vartheta = \frac{\overrightarrow{CD} \cdot \overrightarrow{SC}}{|\overrightarrow{CD}| \cdot |\overrightarrow{SC}|} = \cos \varphi_0 \sin \theta_0 \sin \beta_i + \cos \theta_0 \cos \beta_i \quad (2)$$

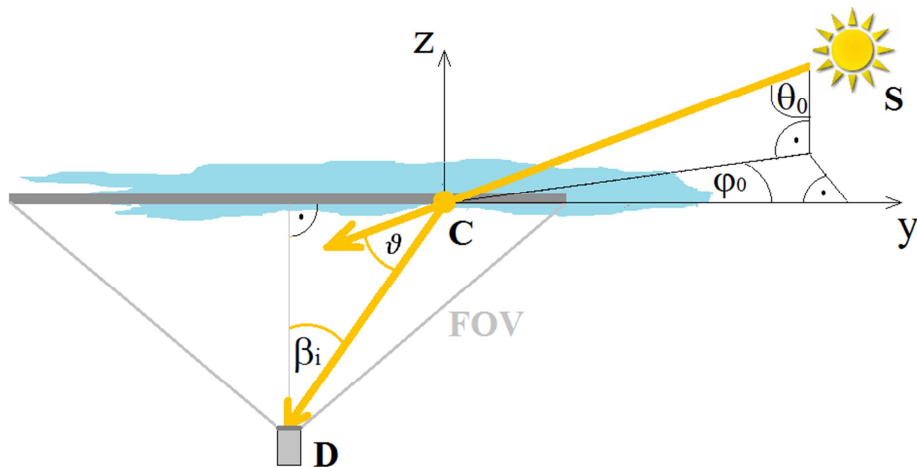


Fig. 2: Illustration of the AisaEAGLE measurement geometry in a Cartesian coordinate system (x , y , z) with position of the Sun (S), a scattering cloud particle (C) and the AisaEAGLE detector (D). θ_0 is the solar zenith angle, φ_0 the solar azimuth angle, ϑ the scattering angle, and β_i the viewing angle of the corresponding pixel.

For the calculations the solar azimuth angle φ is considered relatively to the azimuth angle of the AisaEAGLE sensor line. Therefore, φ is cancelled out in the above given equation for the scattering angle ϑ .

For each spatial pixel the radiance is measured spectrally between 400 nm and 970 nm with 488 wavelength pixels. The spectral resolution is 1.25 nm FWHM. During the CARRIBA project in 2011 a frame rate of 4 Hz was used. The integration time was chosen between 10 ms and 30 ms, depending on the illumination of the cloud scene.

2.3 Calibration, Corrections, and Data Handling

The data collected by the AisaEAGLE are given in counts per integration time. A calibration to obtain radiances I in units of $\text{W m}^{-2} \text{nm}^{-1} \text{sr}^{-1}$ is performed with an integrating sphere and the software AisaTools (provided by the manufacturer). The dark current is determined separately with a shutter. The calibration factors for each pixel are calculated from the calibration measurements using a certified radiance standard (integrating sphere) traceable to the U. S. National Institute of Standards and Technology.

Since the AisaEAGLE detector is based on CCD technique, it is necessary to correct for the smear effect in calibration and measurement data. The smear effect occurs during the read-out process of the collected photo-electrons which are shifted step by step from one spectral pixel to the neighboring one into the direction of the read-out unit. The read-out process is not infinitely fast. Due to the fact that radiation still can reach the sensor during the read-out, the pixels are contaminated by an additional signal. The read-out process for the longer wavelengths ends earlier than the read-out for the shorter wavelengths. Therefore, the additional signal (smear effect) is larger for shorter wavelengths which are longer illuminated during the read-out. The whole procedure for correcting the measurements for the smear effect can be found in Schäfer et al. (2013).

3. Retrieval of Cirrus Optical Thickness

For the retrieval of the cirrus optical thickness τ_{ci} from the measured downward spectral radiance I^{\downarrow} transmitted through the cirrus, radiative transfer calculations were performed. The radiative transfer solver DISORT 2 (Discrete Ordinate Radiative Transfer) was applied. Input parameters, such as cloud optical properties, aerosol content and spectral surface albedo are provided by the library for radiative transfer calculations (libRadtran, Mayer and Kylling, 2005). The so called HEY (Hong, Emde, Yang) parameterization was used to describe the scattering properties of ice crystals. It uses pre-calculated ice cloud optical properties including full phase matrices generated with the models by Yang et al. (2000)

The simulations were performed for 530 nm wavelength, which allows a comparison with the available LIDAR data. Since the BCO is located at the far end of this cape, the measurement site is surrounded by half water and half rocks and grass. For simplification the surface albedo in the radiative transfer simulations was assumed to be only water, as derived by Wendisch et al. (2004) providing a value of 0.068. A maritime aerosol type, provided by libRadtran was used. The cloud altitude and cloud vertical extend was determined by LIDAR measurements of BCO. On the basis of the MODIS data collection 5, a fixed effective radius (r_{eff}) of 20 μm was assumed as no direct retrieval from AisaEAGLE is possible. Downward solar radiance I^{\downarrow}_{cal} was calculated as a function of τ_{ci} . By fitting the measured downward solar radiance I^{\downarrow}_{meas} to the simulation, the corresponding τ_{ci} is interpolated.

The imaging measurements require an accurate description of the sensor geometry in the simulations as shown in Figure 2. The sensor was aligned horizontally. The viewing zenith angle is given by the sensor FOV ($\beta = \pm 18^\circ$). Related to this range, the downward solar radiance I^{\downarrow}_{cal} was calculated in steps of 0.3° .

4. Measurements

4.1 Measurement Cases

Four datasets of different days were evaluated: 9, 16, 18, and 23 April 2011. Figure 3a to 3d show all-sky images from the beginning of the four cases. These days showed persistent cirrus with no other clouds below. An overview of the main characteristics of the evaluated measurement periods can be found in Table 1.

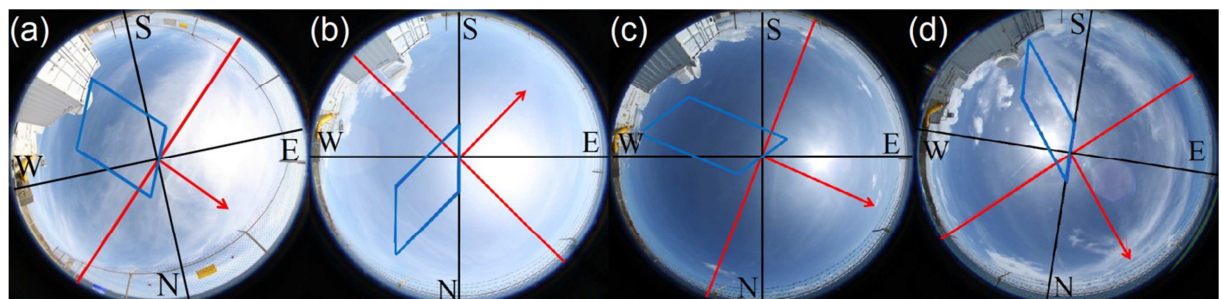
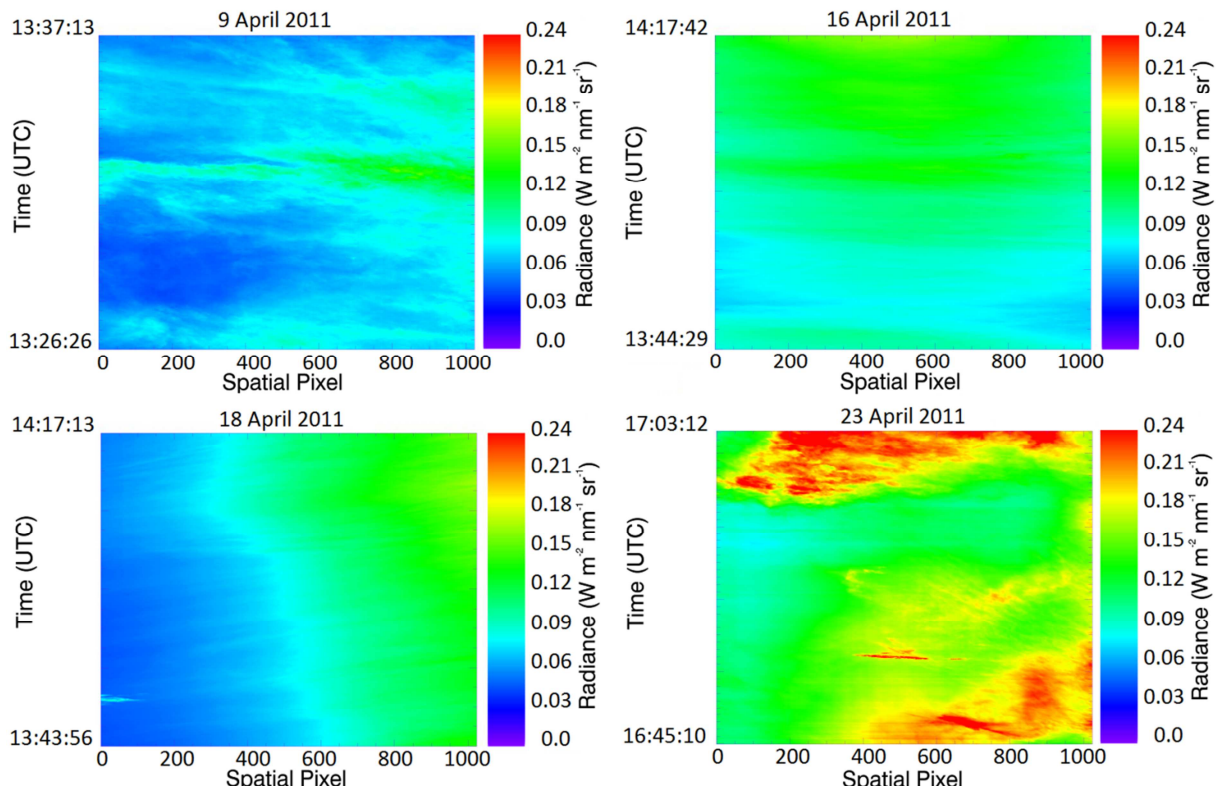


Fig. 3: All-sky image from the beginning of the evaluated AisaEAGLE radiance measurements for (a) 9 April 2011 (b) 16 April 2011 (c) 18 April 2011 (d) 23 April 2011. In each image the arrow indicates the heading of the cirrus and the rhomb indicates the FOV of the AisaEAGLE radiance measurement.

Tab. 1: Characteristics of the evaluated measurement periods

	9 th April	16 th April	18 th April	23 rd April
start time (UTC)	13:26	13:43	13:43	16:45
average Θ_0 (°)	36.7	28.6	28.5	14.5
heading	SW → NW	NW → SW	WSW → ESE	SSW → NNE
appearance	inhomog.	homog.	homog.	inhomog.
cloud height (km)	11 – 15	12 – 15	13 – 15	11 – 14
\bar{I}^{\downarrow} (W m ⁻² nm ⁻¹ sr ⁻¹) ± σ	0.08 ± 0.02	0.11 ± 0.02	0.10 ± 0.03	0.16 ± 0.03
$\tau_{ci} \pm \sigma$	0.41 ± 0.17	0.28 ± 0.09	0.20 ± 0.03	0.05 ± 0.04
covered theta range	35.1 – 47.1	32.6 – 37.9	21.2 – 48.2	12.2 – 36.3

The heading was derived by comparing the position of clouds in the sequence of all-sky images (15 s time resolution). The blue box indicates the area covered by the AisaEAGLE radiance measurements, the area of cirrus which is heading across the sensor line during the measurement period. Due to the fact that the AisaEAGLE was not orientated perfectly in perpendicular direction of the cirrus heading, the covered area is not a rectangle in most cases.

*Fig. 4: 2D images of the evaluated AisaEAGLE radiance measurements at 530 nm with the measured I^{\downarrow} (W m⁻² nm⁻¹ sr⁻¹) given in colour scales.*

The cirrus for 16 and 18 April 2011 were quite homogeneous. On 9 and 23 April 2011, rather inhomogeneous cirrus was observed. On the 23 April 2011, a 22° halo was identified on the all-sky images but did not range into the FOV of AisaEAGLE.

Fields of transmitted downward radiance I^{\downarrow} as measured by AisaEAGLE for the four cases are presented in Figure 4. The radiance is given for 530 nm in two-dimensional colour scale images for all 1024 spatial pixels on the abscissa and the time

of measurement on the ordinate. The cloud structure seen in the all-sky images in Figures 3a to 3d is clearly imprinted in the radiance field. The average values \bar{I}^\downarrow of the measured radiance I^\downarrow are given in Table 1. The highest value of \bar{I}^\downarrow was observed for 23 April 2011 and the lowest for 9 April 2011.

Especially for 18 April 2011 it is evident that the image is getting brighter from the left to the right side. During this day the sensor line of AisaEAGLE was orientated from north-west (pixel 1) to south-east (pixel 1024) while the solar azimuth position was in the East at the same time. This brightening is caused by enhanced scattering for small scattering angles, corresponding to the shape of the scattering phase function of ice crystals. Therefore, while performing the radiative transfer calculations to retrieve τ_{ci} it is necessary to know the exact alignment of the sensor line and the exact position of the Sun. If the sensor orientation is carefully considered, the retrieval will account for this brightness effect caused by enhanced forward scattering of ice crystals. Using the calculated scattering angles derived for each spatial pixel from Equation 2, Figure 4 can be displayed as a function of scattering angle as shown in Figure 5.

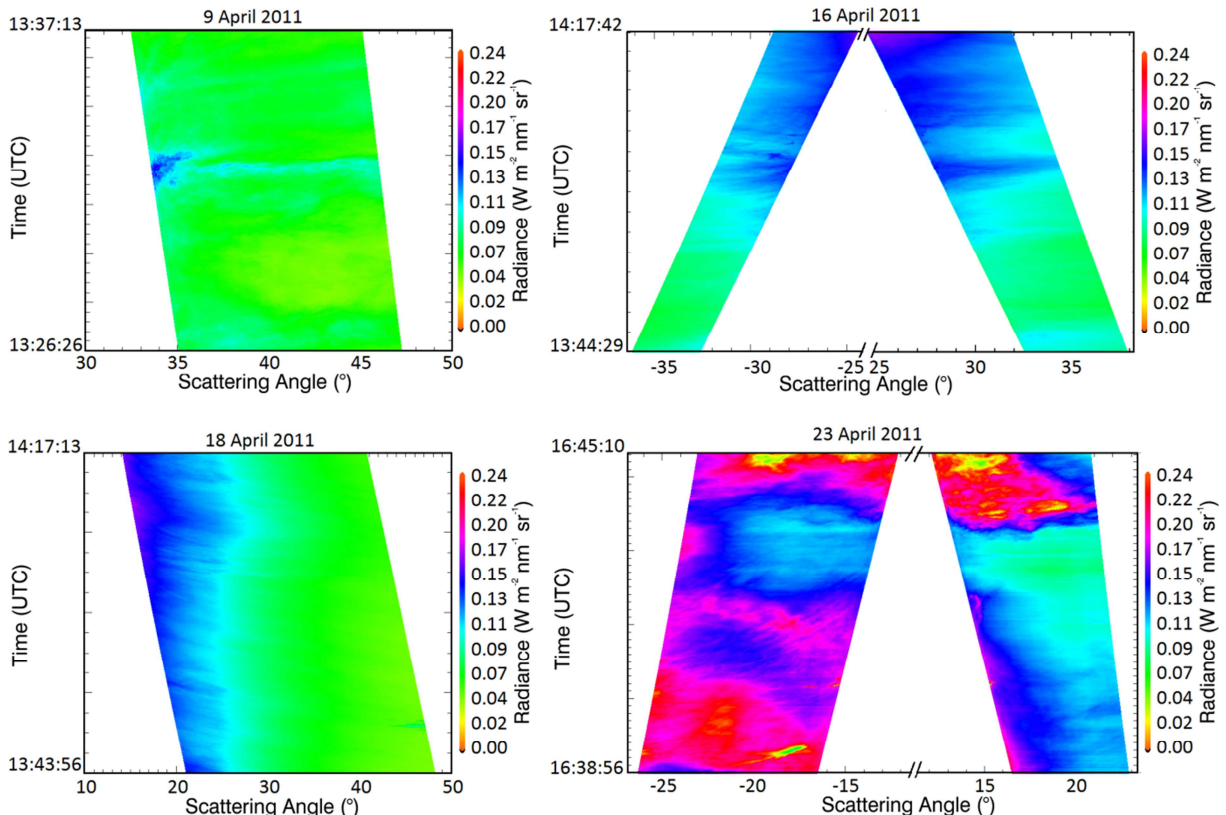


Fig. 5: Time series of the measured downward solar radiance I^\downarrow during the four measurement cases as a function of scattering angles. The range of the abscissa of each image is fitted to the corresponding range of covered scattering angles.

The scattering angles are symmetrical for each pixel to the pixel closest to the Sun. If the Sun's azimuthal position is almost perpendicular to the sensor line, a minimum appears in the detected scattering angles per spatial pixel. In such cases, the plot of I^\downarrow as a function of the scattering angle would have overlapping sections. For clarity, one of those sections is assigned a negative sign in Figure 5. Furthermore, because of the Sun's movement during the measurement period, the images are not rectangular any more. The advantage of the illustration using scattering angles is that structures in the

image related to scattering features of the ice crystals occur now in a fixed position throughout the time series as can be seen for 18 April 2011. The radiance always increases with decreasing scattering angle which is a typical characteristic of the forward scattering of ice crystals.

4.2 Retrieved Ice Crystal Shape

With regard to the all-sky image in Figure 3c (18 April 2011), the best estimation for the ice crystal shape should be the assumption of rough aggregates, since no halo can be figured out in this image. Figure 6 shows the averaged downward solar radiance I^{\downarrow} as a function of scattering angles for 18 April. Additionally included are simulations of the downward solar radiance for different values of τ_{ci} .

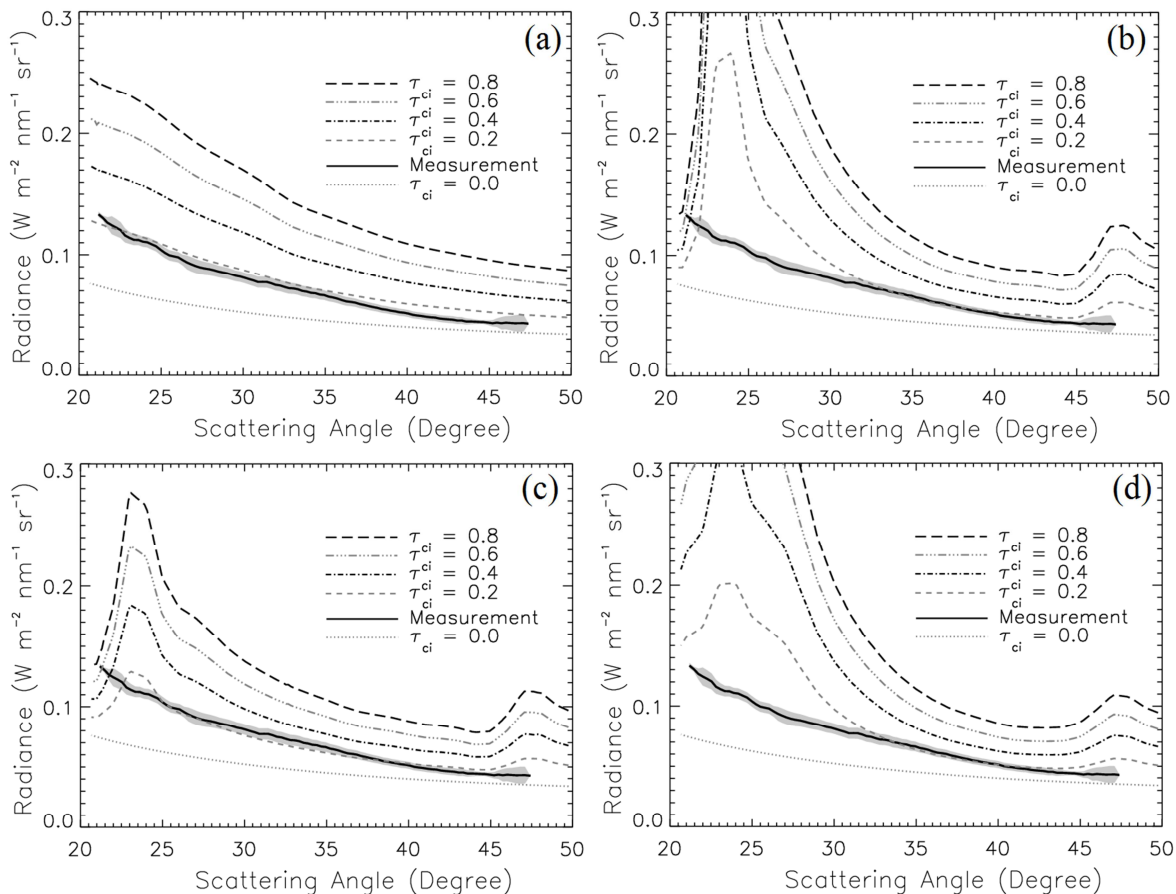


Fig. 6: Measured and simulated I^{\downarrow} as a function of scattering angles. Measurement from 18 April 2011. The standard deviation of the measurement is given as a grey shade. The simulations were performed for different τ_{ci} and assumed ice crystal shapes of a) rough aggregates, b) solid columns, c) plates, and d) mixture.

As can be seen, by performing the simulations for rough aggregates no halo appears in the calculated radiance. However, for the calculations with solid columns, plates, as well as a mixture of ice crystals, the two halo regions are well defined in the simulation results. By comparing the measured downward solar radiance I^{\downarrow} to the simulated ones, the best agreement can be found for rough aggregates. For this reason, in Section 4.3, the τ_{ci} for 18 April 2011 were retrieved by assuming rough aggregates for the ice crystal shape.

As mentioned before, on 23 April 2011 a halo was observed as it can be seen in the all-sky image in Figure 3d. Therefore, in comparison to 18 April 2011 another ice crystal shape than rough aggregates can be expected. Although it is not shown here, between the measured radiance I^* and the simulated one for rough aggregates, only less agreement can be found. For solid columns, plates, and mixed ice crystals it looks more comparable. Since the cloud inhomogeneities during this day were rather high, unfortunately it becomes difficult to figure out the exact ice crystal shape for this case. Therefore, in the following retrieval of the τ_{ci} for 23 April 2011, ice crystals in the shape of solid columns (default setting in libRadtran) were assumed.

Using this method, for 9 April 2011 and 16 April 2011 it is more difficult to estimate the most likely cirrus crystal shape. This is due to the only narrow range of detected scattering angles (halo region is not covered) and the rather high cirrus inhomogeneity on 9 April 2011. Therefore, the radiative transfer calculations to retrieve τ_{ci} were also performed for solid columns.

4.3 Retrieved τ_{ci}

The τ_{ci} retrieved by the presented method are displayed in Figure 7. The unit of the abscissa and ordinate are converted into distances to the swath width and heading distance of the cirrus, respectively. For this, the altitude of the cloud base was used to derive the values for the abscissa. The average wind velocity in the same altitude, derived from the U. S. National Oceanic and Atmospheric Administration (NOAA), was used to convert the ordinate into a distance.

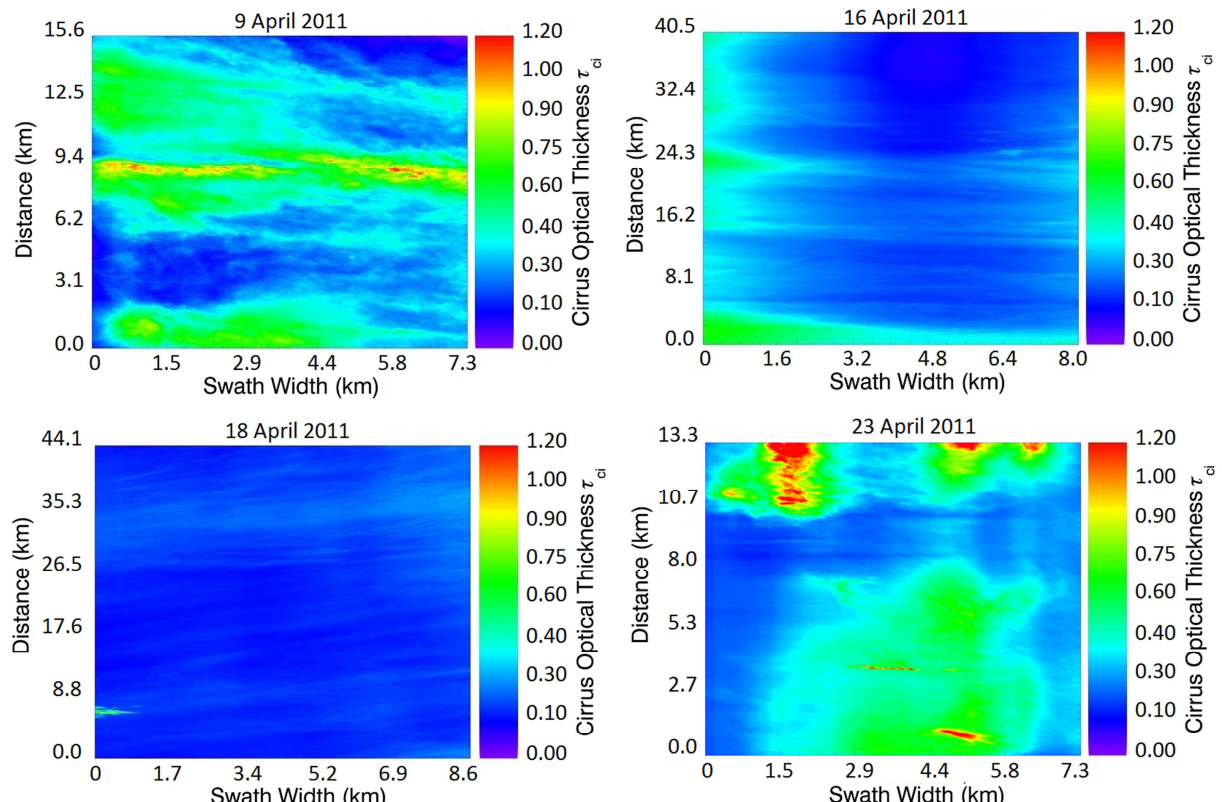


Fig. 7: Time series of the retrieved τ_{ci} during the four measurement case. Abscissa and ordinate values are different due to different measurement conditions.

For 18 April 2011 the retrieved τ_{ci} indicates that the cloud is very homogeneous. This confirms that the observed increase in radiance (Figure 4 and 5) results from enhanced forward scattering of ice crystals and has been considered correctly by the model. For 23 April 2011 it can be found that quite inhomogeneous cirrus was observed with large areas of clear-sky regions in between.

Frequency distributions of the retrieved τ_{ci} for each measurement day are shown in Figure 8. The histograms are normalized by the total of the retrieved τ_{ci} with a bin size of 0.01 in τ_{ci} .

The average values and the standard deviation of the retrieved τ_{ci} for each dataset are listed in Table 1. High standard deviations compared to the average values are a further measure for the inhomogeneities of the detected cirrus. Thus, the AisaEAGLE measurements confirm that the cirrus on 16 and 18 April 2011 was more homogeneous than on 9 and 23 April 2011.

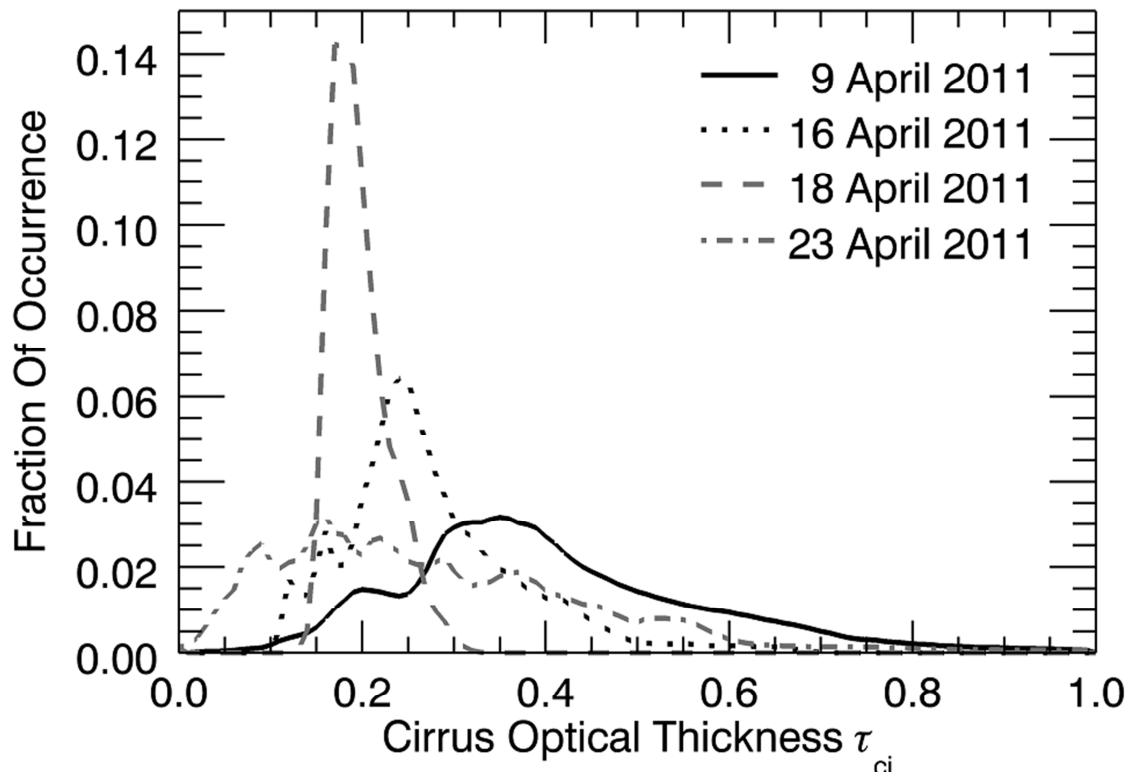


Fig. 8: Normalized histograms of τ_{ci} for each of the four considered measurement days. Bin size is 0.01 in cirrus optical thickness τ_{ci} .

5. Summary and Conclusions

Downward solar radiance fields were measured with high spatial, spectral, and temporal resolution using the imaging spectrometer AisaEAGLE. The procedure of data evaluation (dark current correction, smear correction) was described briefly.

The cirrus optical thickness τ_{ci} is retrieved from the radiance measurements. On the basis of four measurement cases collected during the CARRIBA project in 2011 on Barbados, the feasibility of retrieving cirrus optical thickness at high spatial resolution and characterizing the cirrus heterogeneity was demonstrated. The cirrus on 16 and 18 April 2011 was quite homogeneous with mean τ_{ci} of 0.28 and 0.20 and coefficients of

variation of 0.09 and 0.03. Therefore, the 16 and 18 April 2011 showed quite homogeneous cirrus, while on 9 and 23 April 2011 rather inhomogeneous cirrus with mean τ_{ci} of 0.41 and 0.05 and coefficients of variation of 0.17 and 0.04 was observed. It was found that the inhomogeneity of the investigated cirrus is represented by the standard deviation of the retrieved τ_{ci} .

The determination of the ice crystal shape is complicated without in situ measurements inside the cirrus. Due to the fact that AisaEAGLE is able to measure radiance as a function of a wide range of calculable scattering angle, it gives the opportunity to receive information about the scattering phase function from the radiance measurements. A first feasibility study on this topic was given during this work by comparing measured and simulated radiance as a function of scattering angles. By this, it was already possible to distinguish between halo producing and non-halo producing ice crystal shapes. This topic will be further investigated in future studies by increasing the detected scattering angle range, using a scanning version of the AisaEAGLE, as well as by parameterizing the cirrus inhomogeneities. The results will then be implemented in the retrieval algorithm to allow cirrus retrieval independent on any assumption of ice crystal shape.

To adjust the measurement set up for this purpose, the best way to operate AisaEAGLE in a ground-based application is to adjust the sensor line into the azimuthal direction of the Sun, with the clouds heading perpendicularly across the sensor line. Performing the measurements like this, the maximum possible range of the scattering phase function as well as the maximum possible range of the cloud field can be detected without a spatial distortion of the cloud shape.

6. Outlook

It has been shown that radiance measurements, collected with the imaging spectrometer AisaEAGLE can be used to retrieve the ice crystal shape of the detected cirrus. This holds for measurements where the range of the detected scattering angles is wide enough and reaches into the halo range.

On the basis of this study, the assessment of the ice crystal shape from angular measurements of the solar spectral radiance will be applied to airborne measurements of the AisaEAGLE system. Furthermore, the data analysis will be extended to separate between water and ice clouds. Since the scattering phase functions of cloud droplets and ice crystals are quite different to each other, this will help to identify the cloud particles phase (droplets, ice crystal).

Measurements to test this approach were already performed in April 2012 during the Vertical Distribution of ice in Arctic Clouds (VERDI) project in Canada. Figure 9 shows such airborne measurements. The variable shape of the detected scattering angle range arises from the measurement geometry. Where the detected scattering angle range is wide, the flight direction was perpendicular to the azimuthal position of the Sun. In contrast to this, the detected scattering angle range narrows, when the flight direction was into the direction of the azimuthal position of the Sun or away from it.

For the selected case the range of the scattering angles reaches from 90° to almost 140° . Unfortunately due to this range the halo region (22° , 46°) as well as the cloud-bow region ($\approx 138^\circ$) is not covered. The cloud-bow is a backscatter feature,

which is typically for scattering by liquid water droplets. If this cloud-bow appears in the data it would indicate the detected cloud as a liquid water cloud.

During the upcoming Radiative Closure Experiment for Arctic Clouds (RACEPAC) campaign in April/ May 2014 the fly pattern will be adjusted to cover also the missing scattering angle range. This will be done by a perpendicular flight pattern relative to the Sun's azimuthal position. This flight pattern and additional roll manoeuvres will increase the attitude angles of the airplane, which enlarges the range of detectable scattering angles.

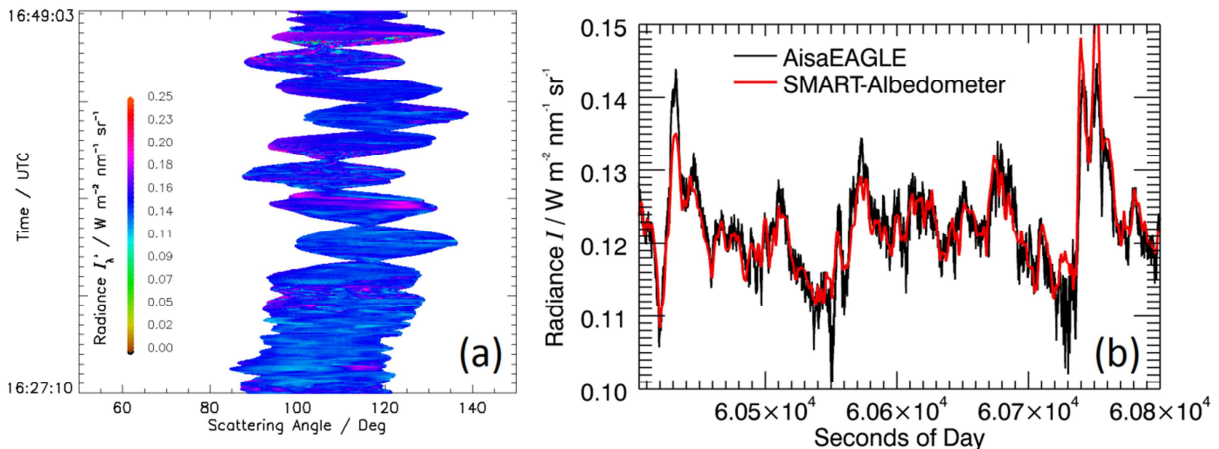


Fig. 9: a) Example time series of radiance measured by AisaEAGLE as a function of scattering angles. b) Example time series of the radiance measured by the center spatial pixel of AisaEAGLE and the SMART-Albedometer.

The results derived by this method will be validated against retrieval results of measurements performed with the Spectral Modular Airborne Radiation measurement sysTem (SMART-) Albedometer (Wendisch et al., 2001). With the SMART-Albedometer cloud microphysical properties such as optical thickness, effective radius, and cloud particle phase can be retrieved. A first comparison of the radiance (at 530 nm wavelength), collected by the AisaEAGLE (center spatial pixel) and the SMART-Albedometer during the VERDI project is given in Figure 9b. The collected radiance given in this time series can be found as well matched.

This new method will extend the information about microphysical properties of the observed two dimensional cloud field while the SMART-Albedometer measures only in Nadir direction. It will allow further investigations concerning the effects of cloud inhomogeneities.

Acknowledgements

We are grateful for funding of project SI 1534/3-1 and WE 1900/18-1 by the German Research Foundation (Deutsche Forschungsgemeinschaft, DFG) within the framework of CARRIBA. The authors thank the Institute for Tropospheric Research, Leipzig, and the Max Planck Institute for Meteorology, Hamburg for organising the campaign and the logistic support at BCO.

References

- Bierwirth, E., Ehrlich, A., Wendisch, M., Gayet, J.-F., Gourbeyre, C., Dupuy, R., Herber, A., Neuber, R., and Lampert, A. (2013). Optical thickness and effective radius of Arctic boundary-layer clouds retrieved from airborne nadir and imaging spectrometry. *Atmos. Meas. Tech.*, 6, 1189–1200.
- DellEndice, F., Nieke, J., Koetz, B., Schaepman, M. E., and Itten, K. (2009). Improving radiometry of imaging spectrometers by using programmable spectral regions of interest. *ISPRS J. Photogramm.*, 64(6):632 – 639.
- Dobbie, S. and Jonas, P. (2001). Radiative influences on the structure and lifetime of cirrus clouds. *Q. J. R. Meteorol. Soc.*, 127:2663–2682.
- Eichler, H., Ehrlich, A., Wendisch, M., Mioche, G., Gayet, J.-F., Wirth, M., Emde, C., and Minikin, A. (2009). Influence of ice crystal shape on retrieval of cirrus optical thickness and effective radius: A case study. *J. Geophys. Res.*, 114:D19203, doi:10.1029/2009JD012215.
- Garrett, T. J., Gerber, H., Baumgardner, D. G., Twohy, C. H., and Weinstock, E. M. (2003). Small, highly reflective ice crystals in low-latitude cirrus. *Geophys. Res. Lett.*, 30:doi:10.1029/2003GL018153.
- Hanus, J., Malenovsky, Z., Homolova, L., Veroslav, K., Petr, L., and Pavel, C. (2008). Potentials of the VNIR Airborne hyperspectral system AISA Eagle. In *Symposium GIS Ostrava*, (CZ).
- Liu, H.-C., Wang, P., and Schlesinger, R. (2003). A numerical study of cirrus clouds. Part II: Effects of ambient temperature, stability, radiation, ice microphysics, and microdynamics on cirrus evolution. *J. Atmos. Sci.*, 60:1097–1119.
- Marsham, J. and Dobbie, S. (2003). The effects of wind shear on cirrus: A large-eddy model and radar case-study. *Q. J. R. Meteorol. Soc.*, 131:2937–2955.
- Mayer, B. and Kylling, A. (2005). Technical note: The libRadtran software package for radiative transfer calculations - description and examples of use. *Atmos. Chem. Phys.*, 5:1855–1877.
- Schäfer, M., Bierwirth, E., Ehrlich, A., Heyner, F., and Wendisch, M. (2013), Application of ground-based hyperspectral imaging to retrieve ice crystal shape and fields of cirrus optical thickness, *Atmos. Meas. Tech. Discuss.*, 6, 1201–1238.
- Schmidt, K. S., Pilewskie, P., Platnick, S., Wind, G., Yang, P., and Wendisch, M. (2007). Comparing irradiance fields derived from Moderate Resolution Imaging Spectroradiometer airborne simulator cirrus cloud retrievals with solar spectral flux radiometer measurements. *J. Geophys. Res.*, 112:D24206, doi:10.1029/2007JD008711.
- Siebert, H., Bethke, J., Conrath, T., Ditas, F., Hartmann, S., Katzwinkel, J., Schmeissner, T., Stratmann, F., Wehner, B., Wex, H., Shaw, R., Roberts, G., Nuijens, L., Stevens, B., Serikov, I., Ehrlich, A., Bierwirth, E., Schäfer, M., Wendisch, M., Werner, F., Izaguirre, M. A., and Farrell, D. (2012). The Fine-Scale Structure of the Trade Wind Cumuli over Barbados – An Introduction to the CARRIBA Project. *Atmos. Chem. Phys. Discuss.*, 12, 28609–28660.
- Wendisch, M., Müller, D., Schell, D., and Heintzenberg, J.: An airborne spectral Albedometer with active horizontal stabilization, *J. Atmos. Ocean. Tech.*, 18, 1856–1866, 7757.
- Wendisch, M., Pilewskie, P., Jäkel, E., Schmidt, S., Pommier, J., Howard, S., Jonsson, H. H., Guan, H., Schröder, M., and Mayer, B. (2004). Airborne measurements of areal spectral surface albedo over different sea and land surfaces. *J. Geophys. Res.*, 109:D08203, doi:10.1029/2003JD004392.
- Wendisch, M., Pilewskie, P., Pommier, J., Howard, S., Yang, P., Heymsfield, A. J., Schmitt, C. G., Baumgardner, D., and Mayer, B. (2005). Impact of cirrus crystal shape on solar spectral irradiance: A case study for subtropical cirrus. *J. Geophys. Res.*, 110:D03202, doi:10.1029/2004JD005294.
- Wendisch, M., Yang, P., and Pilewskie, P. (2007). Effects of ice crystal habit on thermal infrared radiative properties and forcing of cirrus. *J. Geophys. Res.*, 112:D08201, doi:10.1029/2006JD007899.
- Werner, F., Siebert, H., Pilewskie, P., Schmeissner, T., Shaw, R. A., and Wendisch, M. (2013), New airborne retrieval approach for trade wind cumulus properties under overlying cirrus, *J. Geophys. Res.*, 118, doi:10.1002/jgrd.50334.

Studies of sound attenuation depending on meteorological conditions

M. Wilsdorf, A. Bischoff, A. Ziemann and A. Raabe

Abstract

Previously used standardized calculation methods for sound propagation contain the influence of meteorological parameters just in a very simplified way. But the propagation of acoustic signals over a distance of several kilometers is essentially dependent on the distribution of temperature and wind.

The sound level attenuation maps shown in this work have been calculated with the use of the sound ray model SMART (Sound propagation Model of the Atmosphere using Ray-Tracing). They demonstrate the meteorological influence on the sound attenuation in a distance of up to 15 km from the sound source. SMART takes the current or the predicted state of the atmosphere into account to depict the distribution of sound attenuation near the ground surface. Therefore it is an instrument which is able to estimate sound immission for a current or future moment (sound weather). Applied to meteorological data of longer time periods typical mean sound immissions for individual regions can be derived, which is referred as sound climate. On the one hand these attenuation maps firstly clarify the difference between these two terms. On the other hand they show the dependence of sound propagation on atmospheric conditions on several timescales. Radiosonde data from the years 1990 – 2009 were used for this analysis.

A second part of this study deals with the question whether observational data (radiosonde) can be replaced by model data (COSMO-EU). For this purpose data of the station of Bergen was used for the year 2009.

Zusammenfassung

Bisher verwendete standardisierte Berechnungsverfahren für die Schallausbreitung beinhalten meteorologische Einflüsse nur in stark vereinfachter Weise. Die Ausbreitung akustischer Signale über mehrere Kilometer Entfernung hängt jedoch wesentlich von der Temperatur- und Windverteilung im Gebiet des Emissionsortes ab.

In der Umgebung einer Schallquelle bis hin zu einer Entfernung von 15 km wird in dieser Studie der meteorologische Einfluss auf Schallpegeldämpfungskarten dargestellt, die mit Hilfe des Schallstrahlenmodells SMART (Sound propagation Model of the Atmosphere using Ray-Tracing) berechnet wurden. Das Modell SMART bezieht dabei die beobachteten bzw. prognostizierten meteorologischen Verhältnisse in die Darstellung der bodennahen Schalldämpfungsverteilung ein. Es ist damit ein Instrument für die Abschätzung der Schallimmission zu einem aktuellen oder zukünftigen

Zeitpunkt (Schallwetter). Angewendet auf meteorologische Daten aus längeren Zeittab- schnitten sind mittlere, für einzelne Regionen typische Schallimmissionsaussagen ab- leitbar, was hier als Schallklima bezeichnet wird. Diese Dämpfungskarten sollen zum einen den Unterschied dieser beiden Begriffe verdeutlichen, auf der anderen Seite aber auch die Abhängigkeit beider Zeitrahmen von der Meteorologie aufzeigen. In die Auswertungen gehen Radiosondenbeobachtungen aus den Jahren 1990 – 2009 ein. Ein zweiter Teil dieser Arbeit befasst sich mit der Frage der Ersetzbarkeit von Beobachtungsdaten (Radiosonde) durch Modelldaten (COSMO-EU). Diese Analyse erfolgt beispielhaft für die Station Bergen für das Jahr 2009.

1 Motivation and Background

Noise is still one of the largest environmental impacts in today's time. Sound is called noise if the immission is perceived as annoying. The monitoring and forecast of sound immission is thus an important issue in environmental protection.

The background for the following investigations is an assessment of meteorological sound immission conditions near training areas of the Bundeswehr (German armed forces). The Bundeswehr Geoinformation Office (AGeoBw) is requested to make statements about the sound exposure of the population in vicinity of firing ranges. On the one hand an evaluation of the current sound propagation conditions on the basis of the current meteorological conditions (sound weather) must be prepared to protect the population against noise. On the other hand the mean sound immission in a climatological way in areas near those sound sources has to be investigated (sound climate). The sound immission can be derived in general by standardized calculation methods (e.g. ISO 9613-2) which describe the sound level in a distinct distance from the sound source by the sound power level of the sound source and several additive attenuation factors like geometrical attenuation and atmospheric absorption (SALOMONS, 2001). For propagation distances of up to 15 km, atmospheric refraction has large effects on the sound level (PIERCE, 1989). This effect is only partly included into the standardized methods. Therefore, one aim of this study is to demonstrate the meteorological effect on the extended sound propagation using an operationally applicable model (BALOGH ET AL., 2006; ZIEMANN ET AL., 2007).

The calculations for different conditions of sound attenuation are often based on data from radiosonde. To ensure a higher temporal and spatial flexibility it was investigated in this study whether the measurement data can be replaced by model data. To minimize topographic effects first of all, the lowland radiosonde station ‘Bergen’ and its closest model grid point were chosen for this data comparison.

2 Determination of sound attenuation by the model SMART

There are several kinds of acoustical models to investigate outdoor sound propagation (overview e.g. by SALOMONS, 2001). FFP (Fast Field Program, e.g. NIJS and WAPENAAR, 1990) or PE (Parabolic Equation, e.g. GILBERT and WHITE, 1989) meth-

ods yield a solution of the wave equation. The computing time increases with increasing frequencies, so the computing time for a complete spectrum is for many cases considerable (SALOMONS, 2001). The most complex models are at present the Euler models, also referred to finite-difference, time-domain (FDTD) models (e.g., BLUMRICH and HEIMANN, 2002). A grid-based algorithm in the spatial domain is derived from the linearized Euler equations. The advantage of these models is their ability to deal with phenomena like scattering or to take the effects of buildings and topography into account (HEIMANN and KARLE, 2006). However a high computational effort is necessary so that these models are only applicable at present for studies with a limited area and lower frequencies.

A clear way to model sound propagation is ray tracing using the geometrical acoustics (ATTENBOROUGH et al., 1995). This approximation is applicable if the sound wave length is smaller than the typical length scale of the structures which are influenced by the sound wave. Ray-tracing is also used in acoustic particle models (HEIMANN and GROSS, 1999) which partly overcome difficulties of classical ray models in the vicinity of caustics or in sound shadow zones.

Advantages of ray models are the relative simple incorporation of refraction effects due to an inhomogeneous atmosphere and the very small computational requirements. Therefore, ray-tracing is applicable for the operational use in forecasting the sound weather or to calculate the sound climate of an area based on large meteorological data sets. Thus, the geometrical sound propagation model SMART is used in this study to include on one side the vertical state of the atmosphere adequately and to minimize on the other side the computing time compared with physically and numerically more sophisticated models. Thereby, we turned our main attention to the important influence of refraction (PIERCY et al., 1977) in a stratified atmosphere.

In case of the two-dimensional sound ray model SMART (ZIEMANN ET AL., 2007) sound propagation of a sound ray bundle, which originates of a sound source at the surface, is traced using a refraction law for moving media (OSTASHEV, 1997). The version of the sound ray model SMART applied for this work (BALOGH ET AL., 2006) simulates the propagation of sound with a sound-reflecting surface. This leads to a worst case assumption regarding noise protection, i.e. a maximum amplification of sound intensity for multiple surface reflections.

Input data for SMART are radiosonde observations of wind (amount and direction) and air temperature profiles up to a height of 750 m. Provided that the radiosonde for a distinct time observed at least 5 values within this air layer, the data were used for the further sound immission propagation. Prior to the calculations of sound propagation a linear interpolation between the measured values was carried out. Based on this interpolation, the model SMART uses a very high vertical and an adequate horizontal resolution to show the influence of a vertical inhomogeneous structure of the atmosphere on the sound propagation (WILSDORF ET AL., 2009).

From the place of a monopole sound source sound rays with different elevation angles from 17.8° to 89.998° (with increasing resolution from 0.1° to 0.001°) are traced and their propagation throughout the atmosphere is calculated. If the rays reach the surface

they also can be reflected back to the atmosphere. The sound rays contribute to the sound immission at a specific location, if they pass through a height level of 2 m above the ground. The geometrical parameters of all sound ray paths that reach this place are used to determine the sound attenuation in the immission level and for a distinct horizontal range (ZIEMANN ET AL., 2007). The sound rays in this model are emitted in 36 different directions to create a horizontal map of sound pressure attenuation level (with respect to a sound pressure level in distance of 1 m to the sound source).

If a corresponding input data set of meteorological data is used, SMART is able to numerically reproduce the analytical solution of ray-tracing equations for simple vertical profiles (WILSDORF ET AL., 2009; FISCHER AND ZIEMANN, 2009). But the sound ray model has also the ability to simulate the sound propagation and calculate sound attenuation for several distances from the sound source, if complex vertical profiles of temperature and wind vector are used. The sound attenuation is derived for several horizontal intervals. Thereby, SMART uses an arithmetic mean of all attenuation values for one distance interval. This leads to a realistic smoothing of the attenuation and approximates the effect of sound scattering. Finally an assumption for the sound attenuation within the sound shadow was used, based on the distance-dependent attenuation due to divergence of spherical waves and an additional constant attenuation of 20 dB, to generate a more realistic sound attenuation in the geometrical sound shadow zone (SALOMONS, 2001).

3 Classification of sound propagation conditions

The use of meteorological data from different regions with a climatologically relevant time span, offers the possibility to separate a widespread area into smaller, sound climatologically 'similar' regions (i.e. regionalization, see WILSDORF ET AL., 2010). In each of those individual regions the same data basis is used to make statements about sound weather for an area of immission. The reason for this regionalization is the incomplete overlap of radiosonde stations (Germany: only 13 – 15 stations). Often there is no corresponding station near the location where the meteorological profiles are needed to calculate the sound immission. The use of measurement data would be obsolete if the radiosonde data could be replaced by data of a weather model. But this replacement cannot be made without an appropriate proof that both data sets (radiosonde and model) result in a comparable distribution of sound immission at a corresponding time.

Radiosonde has the advantage that they can capture the real atmospheric state at the place of investigation. But their disadvantage is the incomplete temporal availability of data and the horizontal offset with increasing height in comparison to the starting point. A further, even more essential disadvantage is the small amount of stations which are gathering radiosonde data. This leads to difficulties in a spatial analysis of atmospheric states and sound immissions. A possibility to overcome these problems would be the use of model data as data basis. The advantage of model data is a homogenous distribution of grid points, small distances between the grid points and a

temporal completeness of data. The remaining uncertainty relates to the advantage of radiosonde data: How accurate describe the model data the real atmospheric state especially of the atmospheric boundary layer near the ground surface.

To compare the two different data sets a classification scheme of meteorological profiles, developed at the Leipziger Institute for Meteorology (LIM), is used to classify meteorological sound propagation conditions (see e.g. ZIEMANN ET AL., 2001). This classification is based on the assumption that every possible vertical wind and temperature profile within specified limits can be related to a specific profile class. Afterwards a sound immission distribution, calculated by the model SMART, can be related to the respective profile class. Different profile classes are separated according their sound attenuation distributions. Each point of one sound attenuation map (for one profile class) was compared with the same point for another sound attenuation map (for another profile class). Two profile classes are different from each other when 30% of all points of a sound attenuation distribution for one profile class differ from another one whereby the points must differ numerically by a value of at least 3 dB. In this way the sensitivity of the chosen classification scheme was studied and adapted.

As a result of the sensitivity study a classification was made, based on the gradients of air temperature (5 classes), wind speed (13 classes) and wind direction (24 classes).

The classification of temperature profiles is carried out by using different vertical gradients in three different height layers (0 m – 50 m, 50 m – 250 m, 250 m – 500 m or 750 m for temperature inversion). For the definition of the wind speed classes the increasing wind speed with height was taken into account. Wind speed classes were also related to the wind speed near the surface. Usually higher wind speed gradients can be expected at higher wind speeds. The profiles of wind direction classes were defined according to the corresponding prevalent wind direction at the surface and the turning of the wind (change in wind direction) in the 2nd layer (50 m – 250 m).

With this subdivision one is able to relate all imaginable and plausible distributions of the meteorological parameters temperature, wind speed and wind direction over a certain height level to the entirety of the developed classes: 1551 profile classes. Until now all the currently determined profiles (either radiosonde observations or model data) could be brought in agreement with one specific class (see WILSDORF et al., 2010).

4 Results

4.1 Sound attenuation as sound climate and sound weather based on radiosonde observations

The calculation of sound attenuation was conducted with the model SMART. A calculation of sound attenuation for a discrete time is shown in Fig.1 (the radiosonde observation is taken into account up to a height of 750 m above the surface). This and further figures have to be interpreted in the following manner: at a certain time or over a time span the sound level is attenuated (in comparison to a sound level in a distance of 1 m away from the sound source which is located in the middle of the figure) by a certain value (dB). Thereby the sound attenuation includes the effects of spherical wave

divergence, atmospheric refraction as well as sound reflection at the hard ground surface into account. If sound attenuation would be calculated according to spherical wave divergence alone, concentric circles of sound attenuation contour lines would be visible in the figure. Deviations of the circularity can be traced back to a meteorological influence (change of wind speed, wind direction and temperature with increasing height). Unfortunately, the resulting attenuation maps have not yet been validated by measured values due to dimensions of the investigated area. The model SMART was however compared with measured data (BALOGH et al., 2006, ZIEMANN et al., 2007) The sound attenuation calculated at a specific time can be taken as a snapshot of the atmosphere. This can also be referred to as sound weather. Outgoing from a data set of radiosonde ascents at 0 UTC and 12 UTC for different radiosonde stations in Germany within the period of many years a data base of sound attenuation maps was calculated describing the meteorological influence for single situation (sound weather) but also the averaged situation for a longer time period (sound climate).

In Fig. 1 (left side) such a meteorological situation is shown. The dependence of the thermal stratification and especially the mean wind direction (MWD) result in different sound attenuation maps from time to time and from location to location.

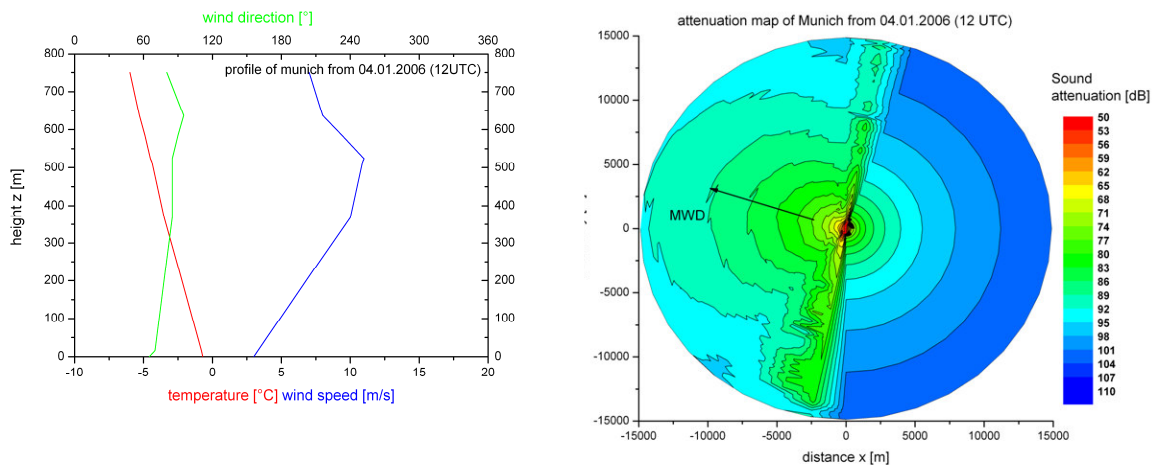


Figure 1: Meteorological profiles of one individual radiosonde ascent for the station Munich on 01.04.2006 at 12 UTC (left) and the corresponding sound level attenuation map at a height level of 2 m (right).

In an upward refracting atmosphere (Fig. 1, sound attenuation map, right side, upwind direction) a so called sound shadow zone develops where no sound rays arrive (see section 2). The sound attenuation in this geometrical shadow zone is high but due to the effects of diffraction and scattering it is finite (SALOMONS, 2001). The sound shadow in upwind direction is therefore approximated by using of sound attenuation due to spherical wave divergence plus a constant value of 20 dB.

A major finding of this study is the fact that the influence of meteorology on both, sound weather, i.e. on current forecast situations, as well as on sound climate (long-term average statements) can be found.

This discrete (current) situation at the example of Munich (Fig.1, right side) describes the so called 'sound weather'. This term can be interpreted as a specific sound propagation situation based on the current measured or forecasted weather data, like this special sound propagation situation on 04.01.2006 at 12 UTC.

This situation is characterized by a distinctive sound shadow east of the sound source and by an area with a lower sound attenuation (mean wind region) west to the sound source in the middle of the picture. This area is the noise pollution area due to increased sound immission based on the influence of the atmosphere state in this specific case.

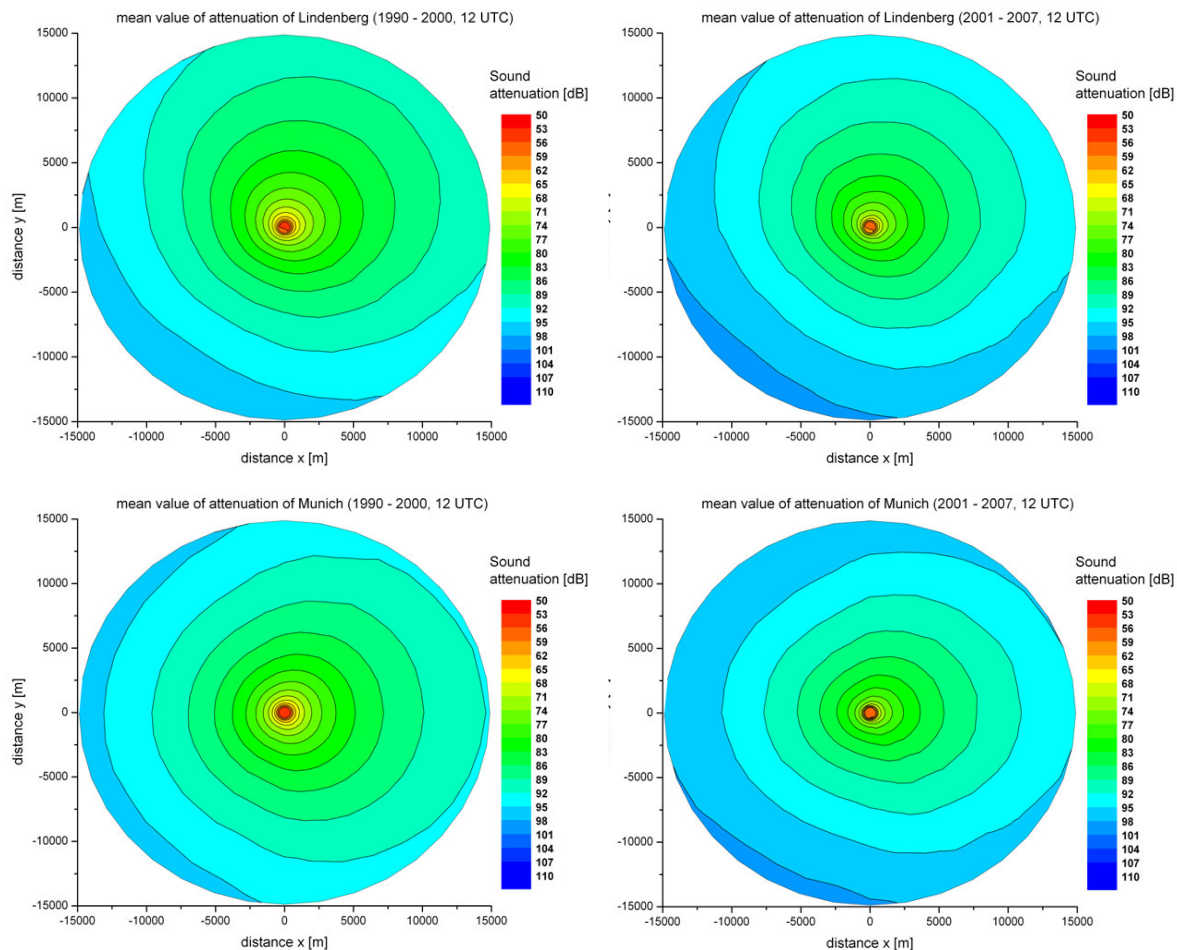


Figure 2: Sound level attenuation of the station Lindenberg (above) and Munich (below) averaged over different periods (1990-2000: left and 2001-2007: right).

In addition to the term sound weather the term 'sound climate' can be defined when different sound propagation situations over a climatologically relevant time span are averaged. In Figure 2 Two examples for different geographical and climatologically sites: a station of the North-east German Plain (Lindenberg) and a station in Alpine Foothills (Munich). Therefore, the sound climate can be interpreted as a mean sound propagation situation at a specific location over a long time.

Even if the averaging time span expands over years, there are still meteorological influences on the sound immission. The mean wind direction has a formative impact on

the sound propagation over long averaging periods and leads to the deviations of the attenuation maps of the circular form of contour lines due to spherical wave divergence. First recognize the main wind direction in Figure 2 (southwest for Lindenberg and west for Munich). Furthermore, a slight increase in attenuation in long-term means is to determine.

These maps still differ from location to location. A classification of the areas with respect to different climatologically sound conditions can be conducted based on the local specifications (see WILSDORF ET AL., 2010).

4.2 Substitutability of radiosonde by model data for the presentation of sound immission distributions

In a first approach, the question of replace ability was investigated with help of radiosonde observations from Bergen because the topographic influence on profile data is relatively low. Therefore the radiosonde measurements of this station were compared to model data of the nearest grid point of the weather model COSMO-EU. The regional model COSMO-EU forms the core of DWD's (German Weather Service) numerical weather prediction system. It is based on the full Euler equations without any scale-dependent approximations, i.e. it belongs to the non-hydrostatic models which solve a prognostic equation for the vertical velocity. The grid resolution of COSMO-EU amounts to 7 km and is significantly higher than that one of radiosonde stations.



Figure 3: Comparison of determined classes of temperature (blue) and temperature inversion (red) between the simulation (model COSMO-EU) and measurement (radiosonde - RSO) of

station Bergen for 12 months in 2009 (radiosonde ascents at 12 UTC): Fraction of coincident profile classes of temperature and temperature inversion depending on the month.

The classification scheme (see section 3) for meteorological profiles developed by the LIM (see RAABE et al., 2000 and ZIEMANN et al., 2002) was used to classify the wind and temperature profiles.

Then, every profile (from radiosonde observations or model data) that has been recorded at 0 UTC and 12 UTC has been classified and analyzed. Due to the character of the profile an assignment to temperature-, inversion-, wind speed-, wind profile- as well as wind direction class was made. Finally all sub classes result in their entirety in a meteorological class which describes the profile (total: 1551 classes).

The main result was basically that there are only small differences between radiosonde and model by the sub-classification according to temperature gradients and a possible inversion. The COSMO-model is able to reproduce the temperature distribution and the occurrence of inversions that can be measured in a real atmosphere. This is depicted in Figure 3.

Small differences are visible in the winter months where inversions occur more often. But even here, the agreement ratio is not lower than 79%.

The assignment to the wind direction classes, with a class width of 30° , was more difficult. The model was just able to reproduce the conditions measured by radiosonde in 25% - 50% of all cases (Fig. 4, blue).

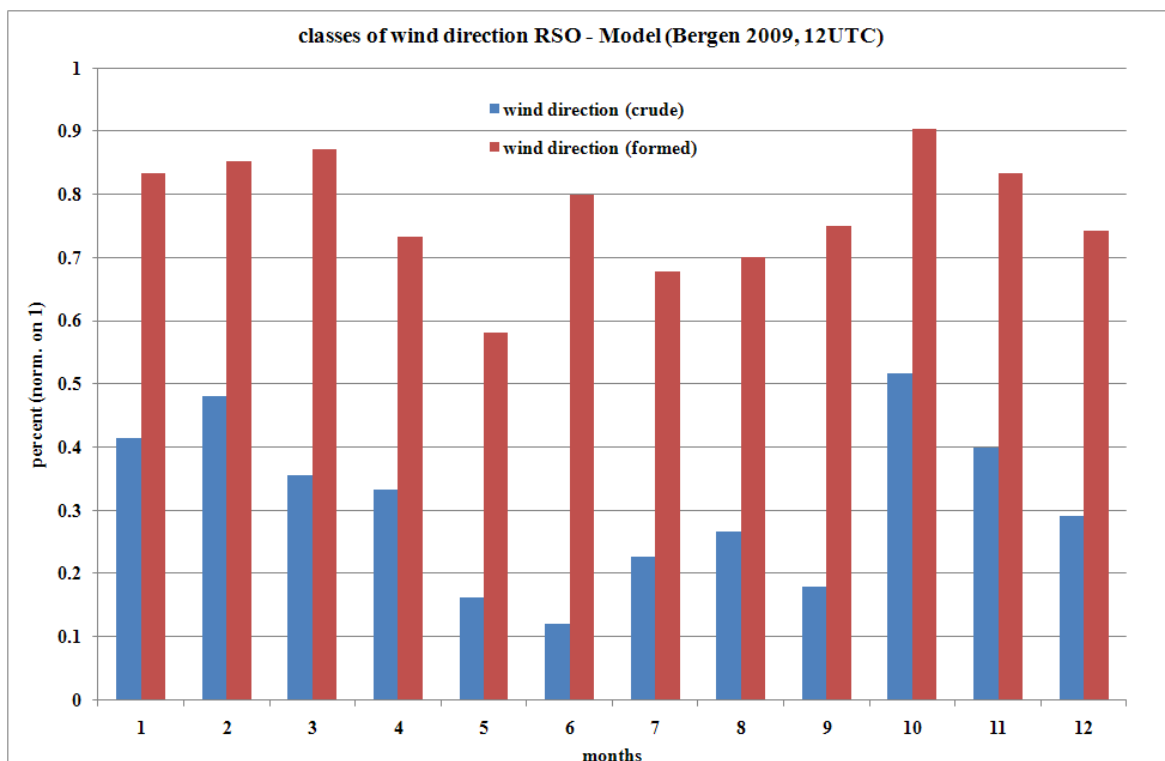


Figure 4: Comparison of determined classes of wind direction between model and RSO of station Bergen 2009 (12 UTC) for original classification (blue) and for formed classification (red).

On the base of the low success rate, the direction class width was enlarged to 90° , so that not only the main sector, but also the sectors left and right of the main sector lead to an agreement. If the model produces a wind direction class, which is one class higher or lower than the original one, this is treated as an agreement. Cause could be that the wind direction class is indeed formed at the ground, and there the influence of the local conditions (difference between RSO station and grid point) are greatest.

The achieved agreement increased from a former average of 30% to an average of 70%. This can be taken as a hint that a substitutability of radiosonde by model data could be possible.

The problems for the wind speed class assignment (Fig. 5) were comparable to those of the wind direction assignment. The agreement of radiosonde and model data reached values from 40% to 65% at the given wind speed classification. This is also shown in Fig. 5. The classification was basically denoted by a division in three blocks: 0-3 m/s, 3-7 m/s und > 7 m/s. If this division is reduced from three to two blocks, so that the resulting blocks span from 0 – 5 m/s and > 5 m/s, then the agreement rises to 70% - 80%.

As a first result one can state that an adequate alignment of radiosonde and model is possible for certain characteristic attributes (temperature, wind vector).

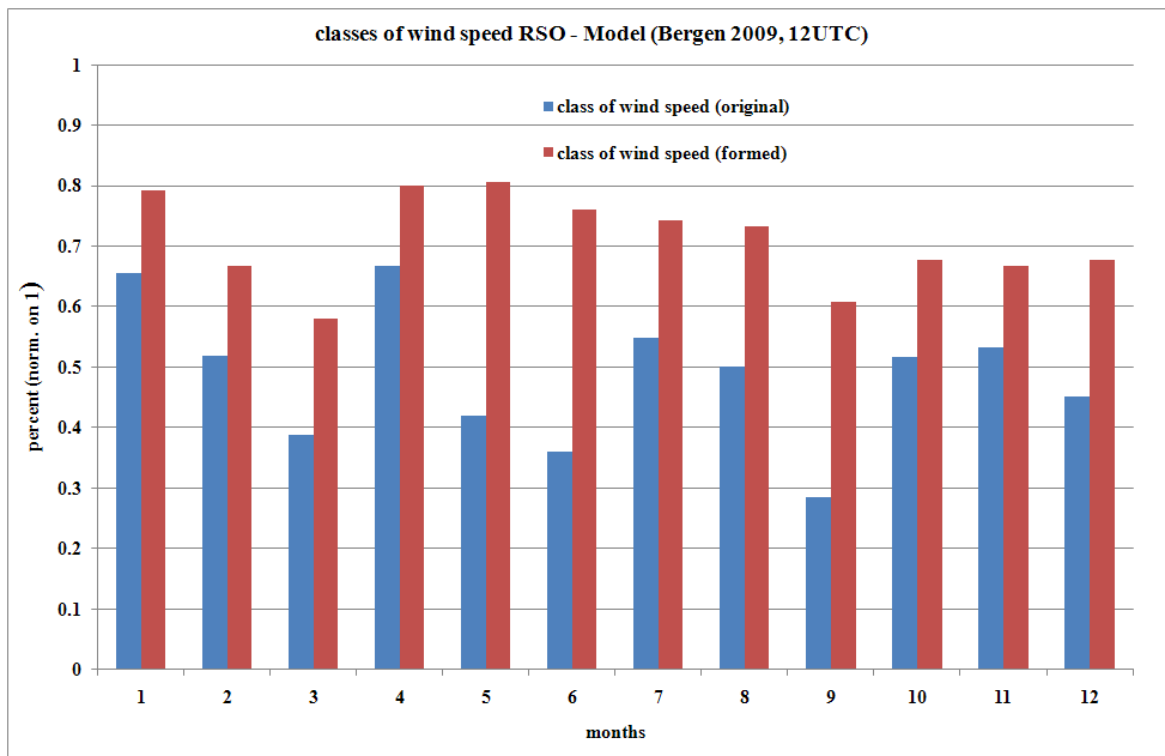


Figure 5: Comparison of determined classes of wind speed between model and RSO of station Bergen 2009 (12 UTC) for original classification (blue) and after treatment (red).

At a high rate of percentage one could replace the radio sonde by COSMO-EU without problems because both profiles are either the same or can be assigned to very similar profile classes. But a full agreement could not yet be determined, especially when the

single attributes (temperature, wind speed, wind direction) were combined into one of the 1551 profile classes.

Supportingly this conclusion, the daily observation and model data were taken as an input for SMART and the particular attenuation distributions were calculated. The comparison (Fig. 6) shows that the sound attenuation distributions are not identical. Both have basically the same mean wind direction, but in general the sound levels using the data of the model are more attenuated than that one using the radiosonde observation.

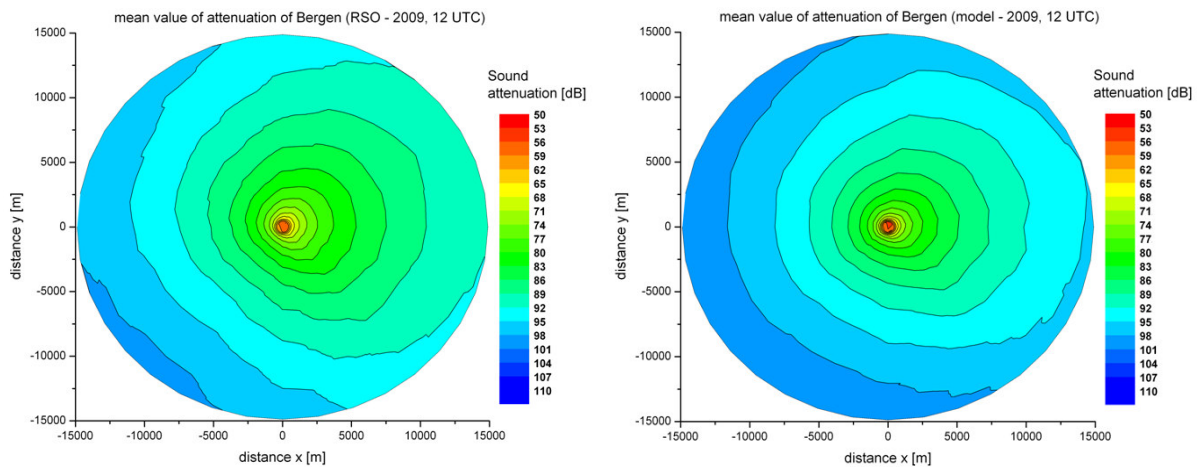


Figure 6: Sound level attenuation in the mountains surrounding the station Bergen as an annual average based on radiosonde data (left) and due to model data (right) for 12 UTC.

A mean deviation of the model from the radiosonde of about 3 dB can be found in a qualitative consideration of the attenuation calculation. This deviation is approximately distributed uniformly over the whole area.

5 Conclusions

The sound attenuation calculations, related to a specific time, are suited for the evaluation of sound weather and so for the investigation of individual sound events, e.g. annoying or dangerous sound exposure. The averaging method applied here (sound climate) is suitable to determine the longer-term sound propagation at specific areas. However, the relatively small number of radiosonde stations for regional considerations of sound is only suitable entries. If there would be a possibility to replace the radiosonde observations by simulated data of a numerical weather forecast model, then a synthetic, but complete data set would be available. On base of this data set the relevant sound propagation conditions at a dense grid of specific locations could be studied continuously.

In this work a simple comparison between both data sources on the basis of a classification of meteorological parameters was conducted. As a first result one can conclude, that for specific characteristic attributes an agreement between radiosonde and model is possible. In many cases the radiosonde observation could be replaced by COSMO-

EU model data, because both profiles could be assigned to the same or a similar profile class. A total agreement of radiosonde observations and model data could not yet be shown, especially if the single attributes were combined to a meteorological profile class.

6 Acknowledgments

We thank the Federal Ministry for defense for the financial support of this project (order number: M/UR1M/7A180/7A524). In particular we thank Dr. Belitz of the Bundeswehr Geoinformation Office for the supply of the meteorological input data as well as for very good cooperation.

7 References

- ATTENBOROUGH, K., S. TAHERZADEH, H.E. BASS, X. DI, R. RASPET, G.R. BECKER, A. GÜDESEN, A. CHRESTMAN, G.A. DAIGLE, A. L'ESPÉRANCE, Y. GABILLET, K.E. GILBERT, Y.L. LI, M.J. WHITE, P. NAZ, J.M. NOBLE, H.A.J.M. VAN HOOF,** 1995: Benchmark cases for outdoor sound propagation models. – *J. Acoust. Soc. Amer.* 97, 173–191
- BALOGH, K., ZIEMANN, A. and DANIEL, D.,** 2006: Influence of atmospheric refraction on pulse propagation over flat ground surface. *Acta Acustica unidet with Acustica* Vol. 92, p. 848-852
- BLUMRICH R., D. HEIMANN,** 2002: A linearized Euler sound propagation model for studies of complex meteorological effects. – *J. Acoust. Soc. Amer.* 112, 446–455.
- FISCHER, G., ZIEMANN, A.,** 2009: Untersuchung des Einflusses der variierenden urbanen Grenzschicht auf die Schallausbreitung. *Wiss. Mit. aus dem Institut für Meteorologie der Universität Leipzig*, 45, S. 57-68
- GILBERT, K.E., M.J. WHITE,** 1989: Application of the parabolic equation to sound propagation in a refracting atmosphere. – *J. Acoust. Soc. Amer.* 85, 630–637
- HEIMANN, D., G. GROSS,** 1999: Coupled simulation of meteorological parameters and sound level in narrow valley. – *Appl. Acoust.* 56, 7–100
- HEIMANN, D., R. KARLE,** 2006: A linearized Euler finite difference time-domain sound propagation model with terrain-following coordinates. – *J. Acoust. Soc. Amer.* 119, 3813–3821
- ISO 9613-2,** 1996: Acoustics — Attenuation of sound during propagation outdoors — Part 2: General method of calculation
- NIJS, L., C.P.A. WAPENAAR,** 1990: The influence of wind and temperature gradients on sound propagation, calculated with the two-way wave equation. – *J. Acoust. Soc. Amer.* 87, 1987–1998.
- OSTASHEV, V. E.,** 1997: Acoustics in Moving Inhomogeneous Media. E & FN SPON.
- PIERCE, A. D.,** 1989: Acoustics-An Introduction to Its (Physical Principles and Applications. by Acoustical Society of America.

- PIERCY, J.E., T.F.W. EMBLETON, L.C. SUTHERLAND**, 1977: Review of noise propagation in the atmosphere. – *J. Acoust. Soc. Amer.* **61**, 1403–1418.
- RAABE, A., ARNOLD, K. und ZIEMANN, A.**, 2000: Berücksichtigung atmosphärischer Schallausbreitungsbedingungen bei Messungen und Prognose von Schießlärm. Abschlußbericht zum Auftrag E/F360/X5144, 46 S.
- SALOMONS, E. M.**, 2001: Computational atmospheric acoustics. By Kluwer Academic Publishers.
- WILSDORF, M., FISCHER, G. und ZIEMANN, A.**, 2009: Einfluss der vertikalen Auflösung der Eingangsprofile bei einem Schallstrahlenmodell. *Wiss. Mit. aus dem Institut für Meteorologie der Universität Leipzig*, 45, S. 45-56
- WILSDORF, M., ZIEMANN, A., BELITZ, H.-J. und RAABE, A.**, 2010: Ein Bewertungsverfahren für Schallimmissionsprognosen unter Berücksichtigung der Meteorologie, Lärmbekämpfung 5/2010, Springer Verlag.
- ZIEMANN, A., ARNOLD, K. und RAABE, A.**, 2001: Berücksichtigung atmosphärischer Schallausbreitungsbedingungen beim Lärmschutz. *Wiss. Mit. aus dem Institut für Meteorologie der Universität Leipzig* 24, S. 35-49
- Ziemann, A.**, 2002: Zum Einfluss vertikaler Gradienten meteorologischer Größen auf die Laufzeit von akustischen Signalen zwischen Schallquellen und Schallempfängern in der bodennahen Atmosphäre, *Wiss. Mit. aus dem Institut für Meteorologie der Universität Leipzig* 26, S. 31-42
- ZIEMANN, A., ARNOLD, K. und RAABE, A.**, 2002: Berücksichtigung atmosphärischer Schallausbreitungsbedingungen bei Messungen und Prognose von Schießlärm. Zwischenbericht zum Auftrag E/F360/X5144, 74 S.
- Ziemann, A., BALOGH, K. and ARNOLD, K.**, 2007: Modelling and measuring the atmospheric excess attenuation over flat terrain during night time conditions. *Meteorol. Zeitschrift* 16, S. 429-441

Addresses of authors:

- Michael Wilsdorf** (mwils@uni-leipzig.de): Universität Leipzig, Institut for Meteorology, Stephan Str.3, 04103 Leipzig.
- André Bischoff**: Universität Leipzig, Institut for Meteorology, Stephan Str.3, 04103 Leipzig.
- Astrid Ziemann** (astrid.ziemann@tu-dresden.de): Technische Universität Dresden, Chair of Meteorology, PF 1117, 01735 Tharandt.
- Armin Raabe** (raabe@uni-leipzig.de): Universität Leipzig, Institut for Meteorology, Stephan Str.3, 04103 Leipzig.

Wissenschaftliche Mitteilungen aus dem Institut für Meteorologie der Universität Leipzig Bd. 51

ACRIDICON-Zugspitze field campaign

Manfred Wendisch, Dagmar Rosenow, et al.

Summary

From September 17 to October 5, 2012, a field campaign with focus on clouds, aerosols, radiation and dynamics and their interaction in clouds that was coordinated and organized by the Leipzig Institute for Meteorology took place at the Zugspitze mountain.

Zusammenfassung

Vom 17. September bis 5. Oktober wurde vom Leipziger Institut eine Feldkampagne zur Untersuchung der Wechselwirkung von Aerosolen, Niederschlag und Strahlung insbesondere in Hinblick auf konvektive Wolken auf der Zugspitze koordiniert und organisiert.



Fig.1: (left) Distribution of instruments between the Zugspitze summit and the environmental research station Schneefernerhaus. (right) : LIDAR observing clouds at the summit.

Strong precipitation and associated strong wind can create substantial damages. In order to lay the foundation for a better risk assessment, more precise knowledge of the responsible complex processes is necessary. To this end, a detailed investigation of the involved gases, aerosols, cloud particles and radiation needs to be carried out. This was the focus of the field campaign in which the universities Leipzig, Mainz, Cologne, Munich, Frankfurt, Darmstadt, the Leibniz Institute for Tropospheric Research (TROPOS), the Karlsruhe Institute of Technology (KIT), the DLR German Aerospace Center in Oberpfaffenhofen and the Research Center Jülich participated. Together, they provided 45 instruments that complemented one another and to some extend permitted a mutual evaluation.

The chosen deployment: Schneefernerhaus/Zugspitze

For the location of the field campaign, the spacious and well-equipped environmental research station Schneefernerhaus 300 m below the summit as well as the meteorological situation at the Zugspitze mountain characterized by the occurrence of mixed-phase cloud all year round were beneficial. While cloud microphysical in-situ instruments were deployed on the roof of the Eibsee cable car mountain station, the remote sensing instruments that determine microphysical parameters through the use of radiation measurements were installed on the terraces of the Schneefernerhaus. In this way, the instruments complemented each other and made possible a detailed investigation of the



Fig.3: (left) Cloud microphysical instruments on the roof of the mountain station of the Eibsee cable car. (right) One of the desired meteorological situations: the summit is covered in clouds while the Schneefernerhaus is cloud-free.

clouds that occurred at the summit. In addition, inside the Schneefernerhaus and on its terraces instruments investigating trace gases, aerosols and ice nuclei were installed. They allowed to examine cloud properties as well as the properties of cloud-free air in comparison. During the campaign's core time, 5 radiosondes ascents were performed daily from Garmisch-Partenkirchen.

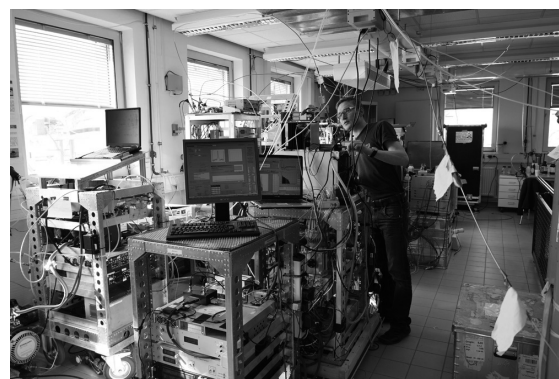


Fig .3: (left) Radiaton measurements on the terrace of the Schneefernerhaus. (right) Aerosol, trace gas- and ice nuclei instruments in the Schneefernerhaus.

This campaign was financed by the Deutsche Forschungsgemeinschaft through the ACRIDICON project (Aerosol, Cloud, Precipitation, and Radiation Interactions and Dynamics of Extra-Tropical Convective Cloud Systems within the framework of the Schwerpunktprogramm HALO.

Jahresbericht des Institutes für Meteorologie der Universität Leipzig 2012

1. Bearbeitete Forschungsprojekte

AG Atmosphärische Strahlung

Hubschraubergetragene Strahlungsmessungen zur Bestimmung des Einflusses von Wolkeninhomogenitäten tropischer Grenzschichtbewölkung auf die Strahlungsbilanz

Helicopter-borne radiation measurements to investigate the influence of cloud heterogeneities of tropical boundary layer clouds on radiative budget

F. Henrich (f.henrich@uni-leipzig.de), M. Wendisch (m.wendisch@uni-leipzig.de)
H. Siebert (siebert@tropos.de)

Die Vernachlässigung von horizontalen Wolkeninhomogenitäten in Modellen zur Berechnung der solaren Strahlungsbilanz von Wolken kann zu erheblichen Diskrepanzen zwischen Modellergebnissen und Messungen führen. In Zusammenarbeit mit dem Leibniz-Institut für Troposphärenforschung wird der Einfluss von Inhomogenitätseffekten von tiefer Cumulusbewölkung in den Tropen auf den Strahlungshaushalt untersucht. Hierfür wird ein neues, kompaktes Messsystem für spektrale Strahlungsmessungen gebaut, welches zusammen mit einer Messplattform für Aerosol-, Turbulenz- und Mikrophysikalischen Wolkenparametern (ACTOS) erstmals die gleichzeitige Beobachtung von Wolkenmikrophysikalischen und Strahlungsgrößen ermöglichen wird. Hierfür wird ein Hubschrauber als Instrumententräger genutzt. Ergänzend sollen dreidimensionale Rechnungen mit einem Strahlungstransfermodell zur Interpretation der Messungen durchgeführt werden.

Das Messgebiet (Barbados) bietet aufgrund seiner Lage zusätzlich die Möglichkeit der Untersuchung von anthropogenen Einflüssen auf den atmosphärischen Strahlungstransfer und die Beeinflussung des solaren Strahlungshaushaltes durch Feuchtigkeits-Halos.

Weiterführung: ja

Finanzierung: Uni Leipzig, DFG WE 1900/18-1, IfT Leipzig

AG Atmosphärische Strahlung

Räumliche Verteilung von Eis- und Flüssigwasser in Arktischen Mischphasenwolken und deren Einfluss auf Energiehaushalt und Fernerkundung

Spatial distribution of ice and liquid water in Arctic mixed-phase clouds and its impact on energy budget and remote sensing

A. Ehrlich (a.ehrlich@uni-leipzig.de), E. Bierwirth (eike.bierwirth@uni-leipzig.de)
M. Wendisch (m.wendisch@uni-leipzig.de)

Mischphasenwolken mit nebeneinander existierendem flüssigem Wasser- und Eisanteil treten häufig in arktischen Regionen auf. Sie können theoretisch in einem Temperaturbereich zwischen -40 °C und 0 °C über längere Zeit hinweg stabil existieren. Wie bekannt ist, unterscheiden sich die optischen Eigenschaften von

reinen Wasser- und Eiswolken und damit auch ihr Einfluss auf die solare Strahlung. Zur Untersuchung der horizontalen Verteilung von Eis- und Flüssigwasser und deren Einfluss auf den Strahlungstransport wird dieses Projekt in Zusammenarbeit mit dem Alfred-Wegener-Institut für Polar- und Meeresforschung (AWI), Bremerhaven, durchgeführt.

Kern des Projektes ist die internationale Messkampagne „Solar Radiation and Phase Discrimination of Arctic Clouds“ (SORPIC), die vom 30.April bis zum 20.Mai 2010 auf Svalbard (Norwegen) stattfand (Projekt-Webseite <http://www.uni-leipzig.de/~sorpic/>). Dabei wurden erfolgreich spektrale solare Strahlungsmessungen an Bord des Forschungsflugzeuges Polar-5 des AWI durchgeführt. Die gemessenen Strahlungsdaten sind vollständig korrigiert und kalibriert und stehen den Projektpartnern zur Verfügung.

Simultan wurden Messungen mit der hyperspektralen Kamera AISA Eagle des AWI durchgeführt; die Auswertung erfolgt in Zusammenhang mit den Strahlungsdaten des SMART-Albedometers am LIM. AISA Eagle wurde im Labor des LIM spektral und radiometrisch kalibriert.

Am 15.November 2010 hat das LIM einen Daten-Workshop mit den beteiligten Projektpartnern (AWI Potsdam/Bremerhaven, LaMP Clermont-Ferrand (Frankreich), Freie Universität Berlin) veranstaltet, bei dem der Fortgang der Datenauswertung und das Publikationskonzept für 2011 abgesprochen wurden.

Weiterführung: ja

Finanzierung: DFG WE 1900/17-1

AG Atmosphärische Strahlung

Eine neue Methode zur bodengebundenen Fernerkundung von Profilen mikrophysikalischer Eigenschaften von Wolken mittels abtastender Radiometrie und Lidar

A novel method for ground-based remote sensing of profiles of cloud microphysical properties using scanning radiometry supplemented by Lidar

E. Jäkel (e.jaekel@uni-leipzig.de), J. Walter (jwalter@uni-leipzig.de), M.Wendisch (m.wendisch@uni-leipzig.de)

Mit Hilfe einer neuen bodengebundenen aktiven und passiven Fernerkundungsmethode soll die vertikale Entwicklung der Wolkenmikrostruktur und das Tropfenwachstum in konvektiven Wolken untersucht werden. Für diesen Zweck werden Strahldichtemessungen (passiv) der an den Wolkenrändern reflektierten solaren Strahlung mit Lidarmessungen (aktiv) kombiniert. Die Wolkenseite wird mit beiden Geräten sowohl zeitlich als auch örtlich synchronisiert vermessen. Diese Messungen werden mit neuen Algorithmen zur Gewinnung von wolkenmikrophysikalischen Parametern kombiniert. Aus den analysierten Messungen kann dann ein Vertikalprofil der thermodynamischen Phase, sowie der effektive Wolkenpartikelradius abgeleitet werden. Dabei werden die drei-dimensionalen Strahlungseffekte der räumlich und zeitlich inhomogenen konvektiven Wolke berücksichtigt, was bei dieser Beobachtungsgeometrie unabdingbar ist.

Weiterführung: ja

Finanzierung: DFG JA 2023/2-1

AG Atmosphärische Strahlung

Megacities - Hochauflöste spektrale Albedo-Karten von Megastädten und ihre Anwendung in Aerosol-Satelliten Datengewinnung

Megacities - High-resolution spectral albedo maps of megacities and its application in aerosol retrievals from satellite data

B. Mey (b.mey@uni-leipzig.de), M. Wendisch (m.wendisch@uni-leipzig.de)
 H. Jahn (heiko.jahn@uni-bielefeld.de), A. Krämer (alexander.kraemer@uni-bielefeld.de)
 , Chen Xingfeng (chenxf@irsa.ac.cn) , Gu Xingfa (guxingfa@irsa.ac.cn)

Megastädte sind eines der größten Quellgebiete anthropogenen Aerosols. Sie fungieren daher als Punktquellen für Aerosole im globalen Kontext und beeinflussen lokal die Gesundheit der Menschen. Daher ist es wichtig den Aerosolgehalt der Atmosphäre in Megastadt-Regionen möglichst genau zu bestimmen. In Regionen ohne dichtes Messnetz für Spurenstoffe, ist die Satelliten-Fernerkundung ein geeignetes Mittel, um Spurenstoffe regelmäßig zu messen. Zur Ableitung der Aerosoloptischen Dicke aus Satellitendaten muss das empfangene Signal der reflektierten Strahlung in einen atmosphärischen Anteil und den Bodenanteil getrennt werden. Der Bodenanteil ist durch die Boden-Albedo oder –Reflektivität gegeben, welcher schwierig aus Satellitenmessungen bestimmt werden kann.

Spektral und räumlich hochauflöste Messungen der Bodenalbedo wurden mit der Kombination aus den flugzeuggetragenen Messsystemen SMART-Albedometer (400-2100 nm) und einer Kamera (Geospatial Systems, MS 4100) mit 3 spektralen Kanälen gemessen. Der erste Datensatz wurde in Leipzig im Jahr 2007 aufgenommen, der zweite Datensatz konnte im Dezember 2009 in Zhongshan, China, gemeinsam mit unseren chinesischen Kooperationspartnern des Institute of Remote Sensing Applications erfasst werden.

Das Satelliten-Tool IMAPP der Universität Wisconsin wurde auf Computern des Instituts für Meteorologie installiert und steht nun für wissenschaftliche Zwecke in diesem, sowie anderen Projekten bereit.

Es wird erwartet, dass durch Verwendung der hochauflösten Messdaten der Bodenalbedo im Aerosol-Retrieval der Satellitendaten das Resultat der Aerosol Optischen Dicke verbessert werden kann.

Weiterführung: nein

Finanzierung: DFG, SPP 1233 (WE 1900/16-2)

AG Atmosphärische Strahlung

Räumlich inhomogene Zirren: Einfluss auf die atmosphärische Strahlung

Spatially Inhomogeneous Cirrus: Influence on Atmospheric Radiation

M. Wendisch (m.wendisch@uni-leipzig.de),

F. Finger (f.finger@uni-leipzig.de)

Die Strahlungseffekte durch inhomogene Zirren werden mit Hilfe einer Kombination von Flugzeuggetragenen Messungen (Strahlung und mikrophysikalische Eigenschaften), einem 3D Strahlungsmodell und einem dynamischen wolkenauflösenden Zirrus-Modell untersucht. Ein instrumentiertes Flugzeug (Lear-Jet) misst die spektrale Strahlung über Zirren im Rahmen einer Feldmesskampagne. Daraus werden die mikrophysikalischen Felder der Zirren abgeleitet. Diese werden verglichen mit gleichzeitigen in situ Messungen, welche mit einer Schleppsonde gesammelt werden. Diese wird gleichzeitig vom Flugzeug durch die Zirren gezogen wird. Parallel dazu werden die örtlichen Inhomogenitäten der Zirren Felder mit Hilfe einer abbildenden digitalen CCD Kamera beobachtet. Zusätzlich wird ein wolkenauflösendes Zirren-Modell benutzt zur Berechnung der mikrophysikalischen Zirren-Felder. Die aus den kombinierten in situ und indirekten Messungen abgeleiteten sowie modellierten mikrophysikalischen Zirren-Felder werden als Eingabe für ein 3D Strahlungsmodell benutzt, um die 3D-Effekte inhomogener Zirren zu untersuchen.

Weiterführung: ja

Finanzierung: DFG WE 1900/19-1

AG Atmosphärische Strahlung

Solare Strahlungsmessungen auf HALO

Solar Radiation Measurements on HALO

C. Fricke (fricke@uni-leipzig.de)

M. Wendisch (m.wendisch@uni-leipzig.de)

HALO (High Altitude and LOng Range Research Aircraft) ist das Synonym für das neue deutsche Forschungsflugzeug mit dem es möglich sein wird, eine Vielzahl von verschiedenen atmosphärischen Parametern bis hin in die untere Stratosphäre zu messen. Aufgrund seiner Reichweite, sowohl in vertikaler als auch in horizontaler Richtung bietet HALO die Möglichkeit großräumige Strahlungsfelder zu erfassen. Während zwei HALO Demo-Missionen kommen dabei neu entwickelte Spektrometersysteme zur spektralen Erfassung solarer Strahlung zum Einsatz. Die dabei ermittelten Messgrößen sind zum einen die (i) spektrale Strahlflussdichte, welche den solaren Strahlungshaushalt der Atmosphäre bestimmt, sowie die (ii) spektrale aktinische Flussdichte, welche photolytische Prozesse innerhalb der Atmosphäre kontrolliert. Die solare spektrale Strahldichte in Nadir-Richtung wird für Fernerkundungsuntersuchungen zusätzlich simultan gemessen. Für die Strahlflussdichten ist es dabei entscheidend, die aufwärts- sowie abwärts gerichteten Flussdichten, welche mittels der Kosinusempfänger oberhalb und unterhalb des Flugzeugs empfangen werden, zu unterscheiden. Hierfür sind Stabilisierungsplattformen vorgesehen, die die Bewegungen des Flugzeuges aufzeichnen und die Position der Empfänger mit hinreichender zeitlicher Verzögerung korrigieren. Bezuglich der aktinischen Flussdichte ist die Kombination aus hoher zeitlicher Auflösung und hoher Genauigkeit innerhalb des UV-B Bereiches die größte Herausforderung. Realisiert wird selbige durch eine entsprechende Kombination aus Monochromatoren und Detektoren. Die aus allen Daten gewonnenen Erkenntnisse sollen zur Modellverbesserung verwendet

werden, um sowohl Oxidationsprozesse als auch die mikrophysikalischen Prozesse, welche für die Bildung und zeitlichen Entwicklung von Zirren verantwortlich sind, besser zu verstehen.

Weiterführung: ja

Finanzierung: DFG WE 1900/21-1

AG Atmosphärische Strahlung

HALO Koordination von “Aerosol, Cloud, Precipitation, and Radiation Interactions and Dynamics of Extra-Tropical Convective Cloud Systems” (ACRIDICON)

HALO coordination of ACRIDICON

D. Rosenow (d.rosenow@uni-leipzig.de)

M. Wendisch (m.wendisch@uni-leipzig.de)

Konvektive Wolken können erheblichen ökonomischen Schaden verursachen aufgrund von starken Windböen, heftigen Schauern und Niederschlägen, welche teilweise mit Hagel, Graupel, und Gewittern verbunden sein können. Die Dynamik und Heftigkeit dieser ausgeprägten Wettererscheinungen werden bestimmt durch mikrophysikalische Prozesse bei der Wolken- und Niederschlagsbildung, welche beeinflusst werden können durch Aerosolpartikel und Wechselwirkungen mit atmosphärischer Strahlung. Weiterhin werden durch konvektive Wolken Spurengase und Aerosolpartikel prozessiert und umverteilt durch vertikalen Transport sowie Ein- und Ausmischen der Wolke mit der Umgebungsluft. Um diese Wechselwirkungen zwischen Spurengasen, Aerosolpartikeln und der Wolken- und Niederschlagsbildung sowie atmosphärischer Strahlung in außertropischen, konvektiven Wolken zu untersuchen, wurde die HALO Demo-Mission “Aerosol, Wolken, Niederschlag, und Strahlungswechselwirkungen sowie Dynamik von außertropischen, konvektiven Wolkensystemen (ACRIDICON)” vorgeschlagen. ACRIDICON trägt bei zu zwei Schwerpunkten des SPP 1294 bei: „Wolken und Niederschlag“ und „Transport und Dynamik in der Troposphäre und der unteren Stratosphäre“. Der vorliegende Antrag beinhaltet hauptsächlich die Organisation und das Management von ACRIDICON sowie teilweise einen Beitrag zur Analyse und Auswertung der Strahlungsmessungen, welche bei dieser HALO Demo-Mission gesammelt werden.

Weiterführung: ja

Finanzierung: DFG WE 1900/22-1

AG Atmosphärische Strahlung

Koordination des Schwerpunktsprogramms 1294 "Atmosphären- und Erdsystemforschung mit dem Forschungsflugzeug HALO (High Altitude and Long Range Research Aircraft)"

HALO coordination project

M. Wendisch (m.wendisch@uni-leipzig.de)

D. Rosenow (d.rosenow@uni-leipzig.de)

Das Projekt dient vornehmlich der Kooperation und der Kommunikation unter den Einzelprojekten des Schwerpunktprogramms. Im Rahmen des Projekts werden ein jährliches Statusseminar sowie jährliche Themen-Workshops geplant und durchgeführt. Die drei Koordinatoren vertreten den SPP gegenüber der DFG, dem Wissenschaftlichen Lenkungsausschuss von HALO (WLA), dem HALO Projektteam des Deutschen Zentrums für Luft- und Raumfahrt (DLR) und nach außen. Das Koordinatoren-Team betreibt Maßnahmen zur Nachwuchs- und Gleichstellungsförderung. Zentrale Initiativen wie gemeinsame Sammelveröffentlichungen in einem Sonderband oder die Durchführung von Sitzungen zu Themenschwerpunkten ("special sessions") bei internationalen Konferenzen sowie der Internetauftritt des SPP werden im Rahmen dieses Projekts koordiniert und durchgeführt.

Weiterführung: ja

Finanzierung: DFG WE 1900/24-1

AG Atmosphärische Strahlung

EUFAR - European Facility for Airborne Research in Environmental and Geosciences

M. Wendisch (m.wendisch@uni-leipzig.de)

D. Rosenow (d.rosenow@uni-leipzig.de)

Im Rahmen dieses Projektes werden die Expert Working Groups koordiniert. Workshops werden organisiert, und ein Buch wird geschrieben:
Wendisch, M., and J.-L. Brenguier, Airborne Measurements – Methods and Instruments. In preparation to be published by Wiley & Sons.

Weiterführung: ja

Finanzierung: EU

AG Atmosphärische Strahlung

Spektrale Strahlungsbilanz über dem Atlantik aus Modell und Beobachtung

Spectral radiation budget over the Atlantic Ocean from model and observation

A. Macke (macke@tropos.de)

M. Wendisch (m.wendisch@uni-leipzig.de)

M. Brückner (mbrueck@rz.uni-leipzig.de)

B. Pospichal (bernhard.pospichal@uni-leipzig.de)

Der Stoff- und Energieaustausch zwischen Ozean und Atmosphäre spielt eine entscheidende Rolle für die physikalische, chemische und biologische Entwicklung unseres Klimasystems Erde. Die von den beteiligten Forschungseinrichtungen entwickelten und eingesetzten Technologien zur in-situ Messung im Ozean und zur aktiven/passiven Fernerkundung der Atmosphäre, ermöglichen erstmalig durch eine Kombination dieser Daten eine kontinuierliche Erfassung relevanter Parameter. Im Rahmen des WGL-Verbundprojekts OCEANET wurde in Zusammenarbeit der Forschungseinrichtungen (IFM-GEOMAR, IfT Leipzig,

Universität Leipzig, GKSS Geesthacht, AWI) eine autonome Messplattform entwickelt, die langfristig für den operationellen Betrieb an Bord von Fracht- und Forschungsschiffen vorgesehen ist.

Zum Verstehen des Klimasystems Ozean und Atmosphäre spielen Wolken und Strahlung eine wichtige Rolle. Da die Wolkenstrukturen sehr inhomogen sind und damit für Strahlungsübertragungsprozesse entscheidend sind, müssen diese Prozesse in Strahlungsparametrisierungen berücksichtigt werden. Eine Kombination der Beobachtung von physikalischen Eigenschaften und Strahlungseigenschaften von Wolken sind eine Möglichkeit solche Parametrisierungen anzugeleichen oder zu validieren. Mithilfe der Erweiterung der breitbandigen Strahlungsflussdichtemessungen auf spektrale Strahldichte- und Strahlungsflussdichtemessungen mit einem bodengebundenem Spektrometer (CORAS) können unterschiedliche Wolkentypen zugeordnet werden. Beobachtete Atmosphärenzustände werden in ein 3D-Monte-Carlo Strahlungstransportmodell eingegeben, sodass die Ergebnisse mit den gemessenen Parametern verglichen werden können. Die Messungen finden weitestgehend auf FS Polarstern statt.

Weiterführung: ja

Finanzierung: Leibniz-Institut für Troposphärenforschung

AG Atmosphärische Strahlung

Ein Monte Carlo Modell zur Berechnung spektraler atmosphärischer Strahlungsgrößen unter Berücksichtigung von Polarisationsprozessen

A Monte Carlo Model to calculate atmospheric radiation considering polarization

M. Wendisch (m.wendisch@uni-leipzig.de)

A. Macke (macke@tropos.de)

Hierbei wird ein neues Strahlungsübertragungsmodell aufgebaut welches explizit Polarisationseffekte berücksichtigt. Das Modell soll nach Fertigstellung mit ähnlichen Modellen verglichen und durch entsprechende Messungen validiert werden.

Weiterführung: ja

Finanzierung: Leibniz-Doktorandenschule

AG Wolken und globales Klima

Evaluierung des Einflusses von kurzlebigen Verschmutzungen der Atmosphäre auf Klima und Luftqualität

Evaluating the climate and air quality impacts of short-lived pollutants (ECLIPSE)

Koordinator: A. Stohl, Norwegian Institute for Air Research (ast@nilu.no)

Beitrag der Universität Leipzig: J. Quaas (johannes.quaas@uni-leipzig.de)

Ribu Cherian (ribu.cherian@uni-leipzig.de)

ECLIPSE hat zum Ziel, effektive Emissions-Reduktions-Strategien für kurzlebige, klimarelevante Verschmutzungsstoffe in der Atmosphäre zu entwickeln und zu evaluieren. Gase und Aerosole wie Stickoxide, Kohlenwasserstoffe, Sulfat und Ruß werden derzeit nicht in klimapolitische Maßnahmen einbezogen. Eine Reduktion kann aber der Abmilderung des Klimawandels dienen und gleichzeitig die Luftqualität verbessern. In ECLIPSE trägt die Universität Leipzig gekoppelte Klimasimulationen mit dem Modellsystem ECHAM6-HAM/MPIOM bei und analysiert Beobachtungen der Klimaänderungen in Osteuropa nach der Wende.

Weiterführung: ja

Finanzierung: EU FP7

Monitoring von Zusammensetzung der Atmosphäre und Klima – Interims-Implementierung.

Monitoring atmospheric composition and climate – interim implementation (MACC-II)

Koordinator: V.-H. Peuch, Europäisches Zentrum für Mittelfristige Wettervorhersage (Vincent-Henri.Peuch@ecmwf.int)

Beitrag der Universität Leipzig: J. Quaas (johannes.quaas@uni-leipzig.de)

Johannes Mülmenstädt (johannes.muelmenstaedt@uni-leipzig.de)

Im Rahmen des europäischen Beitrags für das globale Monitoring für Umwelt und Sicherheit (Global Monitoring for Environment and Security, GMES), bildet MACC den Vorläufer des operationellen Dienstes für die Atmosphärenkomponente. Dabei wird durch die Assimilation einer Vielzahl von Beobachtungen der Zusammensetzung der Atmosphäre in einer neuen Version des Wettervorhersagemodells des Europäischen Zentrums für mittelfristige Wettervorhersage (EZMW) ein konsistenter Datensatz geschaffen. Beitrag der Universität Leipzig ist es, den Klimaantrieb durch den anthropogenen Beitrag zur Aerosolbelastung aufgrund ihres Einflusses auf die Wolken zu berechnen. Auf Basis des neuen Datensatzes soll ein verbesserter Ansatz entwickelt werden.

Weiterführung: ja

Finanzierung: EU FP7

High Definition Clouds and Precipitation for Climate Prediction (HD(CP)²) – Teilprojekte

HD(CP)² - O2 Full-domain observations

HD(CP)² - S1 Diagnostics

HD(CP)² - S6 PDF cloud schemes

Koordinator: Bjorn Stevens, Max-Planck-Institut für Meteorologie (bjorn.stevens@zmaw.de)

Beitrag der Universität Leipzig: J. Quaas (johannes.quaas@uni-leipzig.de)

Christine Nam (christine.nam@uni-leipzig.de)

Odran Sourdeval (odran.sourdeval@uni-leipzig.de)
 Heiner Matthias Brück (matthias.brueck@uni-leipzig.de)

Ziel von HD(CP)² ist es, Parametrisierungen von Wolken- und Niederschlagsprozessen in Klimamodellen zu verbessern, und die Verbesserung der simulierten Wolken-Klima-Feedbacks nachzuweisen. Dazu wird in den Teilprojekten zur Modellierung eine hochaufgelöste (100 m horizontal) Simulation für mehrere Monate über Mitteleuropa vorbereitet, die als Referenz dienen kann. In den Teilprojekten zur Beobachtung werden Datensätze erstellt, die der Evaluierung dieses Modells und der Erstellung oder Verbesserung und Evaluierung von Klimamodellparametrisierungen dienen. In O2 werden konkret Messnetze (Niederschlagsradar, GPS, Ceilometer) und Satellitendaten für flächige Informationen über dem gesamten HD(CP)²-Gebiet aufgearbeitet. In den Teilprojekten zur Synthese wird darauf hingearbeitet, die sehr großen Datenmengen der geplanten Simulation sinnvoll zu verarbeiten. Konkret werden in Teilprojekt S1 Diagnostiken entwickelt, die relevante Metriken online während der Simulation berechnen, so dass kein Herausschreiben von sehr großen Datensätzen und Postprocessing nötig ist. Im Beitrag der Universität Leipzig werden hier Joint-PDFs konstruiert, die für Wolkenparametrisierungen relevant sind. In Teilprojekt S6 wird die Nutzung dieser PDFs für die Evaluierung von Wolkenparametrisierungen in Klimamodellen, die auf Wahrscheinlichkeitsdichtefunktionen (probability density functions, PDFs) der subskaligen Verteilung von der Gesamtwasser-spezifischen Feuchte und ggf. anderen Größen basieren, vorbereitet. Dazu werden Sensitivitätssimulationen mit ECHAM6 mit verschiedenen Wolkenparametrisierungen durchgeführt, und eine Evaluierung auf der Basis der HD(CP)²-Beobachtungen vorgenommen.

Weiterführung: ja

Finanzierung: BMBF

Quantifying Aerosol-Cloud-Climate Effects by Regime

Koordinator: Johannes Quaas, Universität Leipzig (johannes.quaas@uni-leipzig.de)
 Beitrag der Universität Leipzig: J. Quaas (johannes.quaas@uni-leipzig.de)

Dipu Sudhakar (dipu.sudhakar@uni-leipzig.de)

Claudia Unglaub (unglaub@rz.uni-leipzig.de)

Karoline Block ([karoline.block@uni-leipzig.de](mailto:karoine.block@uni-leipzig.de))

Ziel von QUAERERE ist die verlässliche Quantifizierung des Strahlungsantriebs von anthropogenen Aerosolen durch ihren Effekt auf Wolken. Aufbauend auf früheren Arbeiten sollen hierzu Satellitendaten verschiedener Instrumente kombiniert und in einem statistischen Ansatz ausgewertet werden. Die Aerosol-Informationen für diese Studie stammen dabei nicht direkt aus Satellitendaten, sondern in wesentlich besserer Qualität aus der Reanalyse des MACC-II-Projekts. Die statistische Analyse soll für einzelne Wolken-Aerosol-Regime durchgeführt werden. Neben dieser beobachtungsbasierten Abschätzung sollen Simulationen mit dem regionalen Aerosol-Klima-Modell COSMO-MUSCAT (in Zusammenarbeit mit dem Leibniz-Institut für Troposphärenforschung) durchgeführt werden, die in Sensitivitätsstudien mit abgeschalteten anthropogenen Emissionen dazu dienen können, in den statistischen Korrelationen aus den Satellitendaten Kausalzusammenhänge nachzuweisen. Schließlich soll in Simulationen mit dem globalen Aerosol-Klima-Modell ECHAM6-HAM2 eine globale

Abschätzung erzielt werden, die konsistent ist mit der beobachtungsgestützten Abschätzung.

Weiterführung: ja

Finanzierung: Europäischer Forschungsrat (ERC)

Auswirkung möglicher Klimaänderung auf das Wasserdargebot in verschiedenen Wassereinzugsgebieten Sachsens

Potential climate change impacts on the water supply in different drainage basins of Saxony

Prof. Dr. G. Tetzlaff (tetzlaff@uni-leipzig.de), Dr. A. Raabe (raabe@uni-leipzig.de), Dr. M. Barth (mbarth@uni-leipzig.de), L. Schenk (ludwig.schenk@uni-leipzig.de)

Klimaveränderungen wirken sich auf das Wasserdargebot im Einzugsgebiet von Talsperren aus. Aus den Langfristvorhersagen unterschiedlicher Klimamodelle, deren Grundlage verschiedene Emissions-Szenarien sind, sollen Wasserdargebotsaussagen für die Region der sächsischen Talsperren abgeschätzt werden.

Weiterführung: Nein

Finanzierung: Landestalsperrenverwaltung des Freistaats Sachsen (LTV)

AG Hochatmosphäre
Upper Atmosphere

Selbstkalibrierende EUV/UV-Spektrophotometer SolACES
Auto-Calibrating EUV/UV Spectrometers SolACES

Prof. Dr. Christoph Jacobi (jacobi @ rz.uni-leipzig.de), Dr. B. Nikutowski, C. Ungleba

Das vom Fraunhofer IPM entwickelte Instrument SolACES (Solar Auto Calibrating EUV / UV Spectrometers), soll die solare Strahlung im Wellenlängenbereich von 17 bis 220 nm spektral aufgelöst mit hoher radiometrischer Absolutgenauigkeit messen. Im Projekt erfolgt neben Unterstützung der Missionsvorbereitung und -begleitung die Aufbereitung der Rohdaten, Datenauswertung, Erstellung empirischer Modelle der EUV-Strahlung, und Analyse der ionosphärischen Reaktion auf EUV-Variabilität.

Weiterführung: ja

Finanzierung: Auftrag (Fraunhofer-Institut für Physikalische Messtechnik)
Wiedereinstiegsstipendium (C. Ungleba)

AG Hochatmosphäre
Upper Atmosphere

Planetare Wellen aus Radiookultationen
Planetary waves derived from radio occultations

Prof. Dr. Christoph Jacobi (jacobi @ rz.uni-leipzig.de), Prof. A.I. Pogoreltsev, E. Chumak, Russian State Hydrometeorological University

Innerhalb des Projekts sollen globale Karten konvektiver Indizes, abgeleitet aus GPS-Radiokkultationsdaten, erstellt werden. Diese werden ergänzt durch Analysen planetarer Wellenaktivität aus MetOffice-Reanalysen. Die Untersuchungen sollen klären, ob die konvektiven Indizes zur Vorhersage rascher Stratosphärenerwärmungen dienen können.

Weiterführung: nein

Finanzierung: DAAD, Leonhard-Euler-.Stipendium

AG Hochatmosphäre
Upper Atmosphere

Ableitung atomaren Sauerstoffs
Vertical profiles of atomic oxygen

Prof. Dr. Christoph Jacobi (jacobi @ rz.uni-leipzig.de), Prof. V. Yankovsky, E. Fodotova, St. Petersburg State University

Innerhalb des Projekts wird ein Modell weiter entwickelt, welches die Raten atomaren Sauerstoffs aus denjenigen molekularen Sauerstoffs bestimmt. Das Modell dient der Messung von atomarem Sauerstoff mit Satelliten.

Weiterführung: nein

Finanzierung: DAAD, Leonhard-Euler-.Stipendium

AG Hochatmosphäre
Upper Atmosphere

Wellen- und Strahlungsprozesse
Waves and radiation processes

Prof. Dr. Christoph Jacobi (jacobi @ rz.uni-leipzig.de), Prof.G. Shved, Prof. V. Yankovsky, K. Martyshenko, T. Beliaev, St. Petersburg State University

Innerhalb des Projekts sollen einerseits Methoden verglichen werden, mit denen stratosphärische Ozonkonzentrationen aus denjenigen molekularen Sauerstoffs abgeleitet werden können. Weiterhin sollen atmosphärische Normalmoden mit kurzen Perioden theoretisch abgeleitet und mit Hilfe bodengebundenener Messungen erfasst werden.

Weiterführung: ja

Finanzierung: DAAD, Leonhard-Euler-.Stipendium

AG Hochatmosphäre
Upper Atmosphere

Dynamik und Chemie der Troposphäre/Stratosphäre
Dynamics and Chemistry of the troposphere/stratosphere

Prof. Dr. Christoph Jacobi ([jacobi @ rz.uni-leipzig.de](mailto:jacobi@rz.uni-leipzig.de)), Prof. A.I. Pogoreltsev, S. Smythlyev, K. Lazareva, E. Drobasheskaya, Russian State Hydrometeorological University

Innerhalb des Projekts sollen einerseits konvektive Indizes auf der Basis von GPS-Radiookkultationsdaten erstellt werden, und andererseits Chemietransport-modellrechnungen zur Simulation stratosphärischen Ozons durchgeführt werden.

Weiterführung: ja

Finanzierung: DAAD, Leonhard-Euler-.Stipendium

AG Akustik
Acoustics

Bestimmung des Energie- und Stoffaustauschs zwischen Bodenoberfläche und Pflanzenbestand, Umgebung und Atmosphäre durch mikrometeorologische Messverfahren der Anemometrie –Thermometrie, Teilprojekt: Akustische Strömungs- und Temperaturmessungen über einer Lysimeterfläche
Determination of the energy and matter exchange between the ground surface and vegetation canopy, environment and atmosphere using micro-meteorological measurement techniques of anemometry and thermometry, sub-project: Acoustic flow and temperature measurements over a lysimeter

Dr. Armin Raabe (raabe@uni-leipzig.de), Dr. Astrid Ziemann (ziemann@uni-leipzig.de), Dr. Manuela Barth (mbarth@uni-leipzig.de), Dipl. Met. Gabi Fischer (gfischer@uni-leipzig.de), Dipl.-Inf. (FH) Falk Kaiser (fkaiser@rz.uni-leipzig.de), Dr. Sascha Reth (sascha.reth@ugt-online.de), Dr. Christian Heerdt (christian.heerdt@ugt-online.de), Rick Friedrich (rick.friedrich@ugt-online.de), Umwelt-Gerätetechnik UGT GmbH Müncheberg, Prof. Dr. Christian Bernhofer (christian.bernhofer@tu-dresden.de), Dipl.-Hydrol. Markus Hehn (markus.hehn@tu-dresden.de), Dipl.-Geogr. David Schaffrath (david.schaffrath@tu-dresden.de), TU Dresden, Professur für Meteorologie

Für die Quantifizierung des Energie- und Gasaustausches am oberen Rand eines Lysimeters existieren bislang keine allseits anerkannten Messmethoden. Derzeit wird die Lysimeteroberfläche mit Sensoren bestückt, die allerdings ihrerseits die Wechselwirkung zwischen Lysimeter und Luftströmung beeinflussen können.

Einen Beitrag zur Quantifizierung dieser Energie- und Stofftransporte können mikrometeorologische Messverfahren leisten, wenn es gelingt, die Sensoren nahe genug über einer Lysimeterfläche zu positionieren, ohne dass die Wechselwirkungsverhältnisse zwischen Lysimeter und Luftströmung gestört werden.

Deshalb wird hier ein über die Messfläche des Lysimeters aufgespanntes akustisches Temperatur- und Strömungsmessverfahren entwickelt, das in einem durch die akustischen Messstrecken begrenzten Volumen über dem Lysimeter die Wechselwirkung zwischen der Oberfläche und den Luftmassen über dem Lysimeter aufzeichnet. Unter Hinzunahme weiterer Sensoren (in erster Ausbaustufe CO₂, H₂O) soll es gelingen, den Energie- und Massenaustausch in diesem Volumen berührungslos zu sondieren. Dieses kontrolliert behandelte Volumen wird hier als "Akustische Kammer" bezeichnet.

Weiterführung: nein

Finanzierung: BMWi, Zentrales Innovationsprogramm Mittelstand (ZIM), Förderkennzeichen KF2709801BN0

AG Akustik
Acoustics

Sensormodul und Dispatcher-System zur intelligenten und autonomen Überwachung von Umgebungsbedingungen in Rechenzentren und Serverräumen (SenDiServ)

Sensor module and dispatcher system for intelligent and autonomous monitoring of environmental conditions in data centers and server rooms (SenDiServ)

Dr. Armin Raabe (raabe@uni-leipzig.de), Manuela Barth (mbarth@uni-leipzig.de),
Dipl. Met. Gabi Fischer (gfisher@uni-leipzig.de),
gemeinsam mit
RÖWAPLAN AG, Brahmsweg 4, 73453 Abtsgmünd
Und
GED Gesellschaft für Elektronik und Design mbH, Pastoratsstraße 3, 53809
Ruppichteroth-Winterscheid

Es wird eine modulare, miniaturisierte Sensorplattform zur Erfassung und Überwachung von über Schallsignalanalysen ermittelte Luftströmungen und Temperaturverteilungen entwickelt. Das Projekt basiert auf Arbeiten zur akustischen Laufzeitomografie, die am LIM durchgeführt wurden. Die Verfahren werden auf Innenräume umgesetzt und sollen so angewendet werden, dass eine Reduzierung des Kühlenergieverbrauchs u.a. von Rechenzentren und Serverräumen möglich wird.

Weiterführung: ja

Finanzierung: BMWi, Zentrales Innovationsprogramm Mittelstand (ZIM), Förderkennzeichen AIF FKZ KF2709802DF2

AG Akustik

Acoustics

Wetterabhängige Schallausbreitung, Lärmschutz an Schießplätzen der Bundeswehr Weather permitting sound propagation, noise protection at artillery range of the Bundeswehr

Dr. Armin Raabe (raabe@uni-leipzig.de),
Jun.-Prof. Dr. Astrid Ziemann (ziemann@uni-leipzig.de)
Dipl. Met. Michael Wilsdorf (mwils@uni-leipzig.de)

Dieses Projekt setzt die langjährige und erfolgreiche Zusammenarbeit des Institutes für Meteorologie der Universität Leipzig mit der Bundeswehr, hier im speziellen mit dem AGeoBw, fort. Anlass waren Artillerieschießen, bei denen die akustische Belastung in der Nachbarschaft von TrÜb-Plätzen derart erhöht war, dass es zu Beschwerden / Klagen von Bürgern und der Kommunen kam. Ein verstärkender Faktor war in den betreffenden Fällen u.a. die Wettersituation, bei der eine ausgeprägte Temperaturinversion zu einer anomalen Schallausbreitung führte. Ziel dieser Studie ist deshalb die weitere Verbesserung der bestehenden Schallimmissionsprognose, sowohl in konzeptioneller Hinsicht, als auch in ihrer Praktikabilität sowie in der statistischen Absicherung der zu Grunde liegenden Auswertungen. Datengrundlagen der schallklimatologischen Untersuchungen sind Radiosondenaufstiege des Deutschen Wetterdienstes und der Bundeswehr, die im Zeitraum 2001 bis mindestens 2007 an 14 Stationen im Bundesgebiet jeweils zu den Terminen 00 UTC und 12 UTC durchgeführt wurden. Damit erweitern diese Daten den untersuchten Datenumfang einschließlich der Vorgängerstudie (von 1990 bis 2000) auf 18 Jahre.

Weiterführung: Nein

Finanzierung: AGeoBw; M/UR1M/7A180/7A524

AG Bodengebundene Fernerkundung
Ground-based remote sensing

HD(CP)²-High definition clouds and precipitation for advancing climate prediction

Jun.-Prof. Dr. Bernhard Pospichal (bernhard.pospichal@uni-leipzig.de)
MSc Andreas Foth (andreas.foth@uni-leipzig.de)

Dieses Projekt beschäftigt sich mit einem sehr relevanten Thema in der aktuellen meteorologischen Forschung, nämlich der Repräsentation von Wolken in Atmosphärenmodellen. Dabei sind noch viele Unsicherheiten, sowohl auf der Beobachtungs- als auch auf der Modellseite zu bemängeln. Im Rahmen von HD(CP)² wird die Expertise zu diesem Themenkomplex deutschlandweit gebündelt. Intensivierte Beobachtungen an verschiedenen Orten, sowie die Kombination verschiedener Messverfahren, soll es u.a. ermöglichen, bessere Parametrisierungen von Wolken in Modellen zu erhalten.

Am LIM soll in diesem Zusammenhang ein neuer Algorithmus zur Bestimmung vertikaler Wasserdampfverteilung aus Fernerkundungsdaten (passive Mikrowellenradiometer und Raman-Lidar) erstellt werden.

Weiterführung: ja

Finanzierung: BMBF, FKZ: 01LK1209D

AG Bodengebundene Fernerkundung
Ground-based remote sensing

Leibniz Graduiertenschule Wolken-Aerosol-Strahlung (*Leibniz Graduate School Clouds-Aerosol-Radiation*)

Jun.-Prof. Dr. Bernhard Pospichal (bernhard.pospichal@uni-leipzig.de)
MSc Daniel Merk (merk@tropos.de)

Im Rahmen der Graduiertenschule Wolken-Aerosol-Strahlung soll im Rahmen von sieben Promotionen der indirekte Aerosoleffekt von verschiedenen Seiten (Mikrophysik, Chemie, Fernerkundung, etc.) betrachtet werden. Die hier vorliegende Arbeit befasst sich mit Fernerkundungsbeobachtungen. Das Besondere daran ist die Verknüpfung von Satellitendaten (SEVIRI sichtbar und nahes Infrarot) und bodengebundener Fernerkundung (Lidar, Radar, Mikrowellenradiometer im Rahmen von LACROS). Daraus soll eine verbesserte Charakterisierung von Flüssigwasserwolken im Hinblick auf deren mikrophysikalischen Eigenschaften (effektiver Radius, optische Dicke) abgeleitet werden.

Weiterführung: ja

Finanzierung: Leibniz-Gesellschaft (Zusammenarbeit mit TROPOS)

2. Wiss. Veröffentlichungen Institut für Meteorologie 2012

Haupt autor	Autoren / Herausgeber	Titel, in: Zeitschrift, Ort; Verlag, Jahr, Seite von – bis
	Arras, C., J. Wickert, Ch. Jacobi, G. Beyerle, S. Heise, and T. Schmidt	Global Sporadic E Layer Characteristics Obtained from GPS Radio Occultation Measurements. In: Lübken, F.-J. (Ed.): Climate and Weather of the Sun-Earth System (CAWSES), Springer, Berlin, 207-222.
	Baumgardner, D., L. Avallone, A. Bansemer, S. Borrman, P. Brown, U. Bundke, P. Y. Chuang, D. Cziczo, P. Field, M. Gallagher, J.-F. Gayet, A. Heymsfield, A. Korolev, M. Krämer, G. McFarquhar, S. Mertes, O. Möhler, S. Lance, P. Lawson, M. Petters, K. Pratt, G. Roberts, D. Rogers, O. Stetzer, J. Stith, W. Strapp, C. Twohy, and M. Wendisch, 2012:	Workshop summary: In situ, airborne instrumentation: Addressing and solving measurement problems in ice clouds. <i>Bull. Amer. Meteorol. Soc.</i> , doi:10.1175/BAMS-D-11-00123.1
	Bierwirth, E., A. Ehrlich, M. Wendisch, J.-F. Gayet, C. Gourbeyre, R. Dupuy, A. Herber, R. Neuber, and A. Lampert, 2012:	Optical thickness and effective radius of Arctic boundary-layer clouds retrieved from airborne spectral and hyperspectral radiance measurements. <i>Atmos. Meas. Tech. Discuss.</i> , 5, 7753-7781, doi:10.5194/amtd-5-7753-2012.
	Cherian, R., C. Venkataraman, S. Ramachandran, J. Quaas, and S. Kedia	Examination of aerosol distributions and radiative effects over the Bay of Bengal and the Arabian Sea region during ICARB using satellite data and a general circulation model, <i>Atmos. Chem. Phys.</i> , 12, 1287–1305, doi 10.5194/acp-12-1287-2012, 2012.
	Devasthale, A., K. Karlsson, J. Quaas, and H. Grassl	Correcting orbital drift signal in the time series of AVHRR derived convective cloud fraction using rotated empirical orthogonal function, <i>Atmos. Meas. Tech.</i> , 5, 267–273, doi 10.5194/amt-5-267-2012, 2012.
	Ehrlich, A., E. Bierwirth, M. Wendisch, A. Herber, and J.-F. Gayet	Airborne hyperspectral observations of surface and cloud directional reflectivity using a commercial digital camera, <i>Atmos. Chem. Phys.</i> , 12, 3493-3510, doi:10.5194/acp-12-3493-2012.
	Ern, M., C. Arras, A. Faber, K. Fröhlich, Ch. Jacobi, S. Kalisch, M. Krebsbach, P. Preusse, T. Schmidt, and J. Wickert	Observations and Ray Tracing of Gravity Waves: Implications for Global Modeling. In: Lübken, F.-J. (Ed.): Climate and Weather of the Sun-Earth System (CAWSES), Springer, Berlin, 383-408.
	Fischer, G., M. Barth, A. Ziemann	Acoustic Tomography of the Atmosphere: Comparison of Different Reconstruction Algorithms. <i>Acta Acustica united with Acustica</i> , 98, 534-545.
	Fricke, C. , A. Ehrlich, M. Wendisch, B. Bohn	Influence of surface albedo inhomogeneities on remote sensing of optical thin cirrus cloud mikrophysics, <i>Wiss. Mitteil Inst. f. Meteorol. Bd. 50</i> , 1-10
	Gehlot, S. and J. Quaas	Convection-climate feedbacks in ECHAM5 general circulation model: A Lagrangian trajectory perspective of cirrus cloud life cycle, <i>J. Clim.</i> , 25, 5241–5259, doi 10.1175/JCLI-D-11-00345.1, 2012.
	Hoffmann, P., and Ch. Jacobi	Simulation of sudden stratospheric warmings with the Middle and Upper Atmosphere Model, <i>Ber. Inst. Meteorol. Univ. Leipzig</i> , 48, 11-23.
	Hoffmann, P., Ch. Jacobi, and C. Borries	A possible planetary wave coupling between the stratosphere and ionosphere by gravity wave modulation, <i>J. Atmos. Sol.-Terr. Phys.</i> , 75-76, 71-80.
	Hoffmann, P., and Ch. Jacobi	Planetary wave characteristics of gravity wave modulation from 30-130 km, <i>Adv. Radio Sci.</i> , 10, 271-277.

	Hoffmann, P., Ch. Jacobi	Simulation of sudden stratospheric warmings with the Middle and Upper Atmosphere Model MUAM, Wiss. Mitteil Inst. f. Meteorol. Bd. 50, 11-25
	Horn,S., A. Raabe, H. Will, O. Tackenberg	TurbSeed—A model for wind dispersal of seeds in turbulent currents based on publicly available climate data, Ecological Modelling 237– 238 (2012) 1– 10
	Jäkel, E., Walter, J., and Wendisch, M	Thermodynamic phase retrieval of convective clouds: impact of sensor viewing geometry and vertical distribution of cloud properties, <i>Atmos. Meas. Tech. Discuss.</i> , 5, 7729-7752, doi:10.5194/amtd-5-7729-2012
	Jacobi, Ch.	Long-term trends and decadal variability of upper mesosphere/lower thermosphere gravity waves at midlatitudes, Wiss. Mitteil Inst. f. Meteorol. Bd. 50, 25-34
	Jacobi, Ch., C. Arras	Enhanced sporadic E occurrence rates during the Geminid meteor showers 2006-2010, Wiss. Mitteil Inst. f. Meteorol. Bd. 50, 35-44
	Jacobi, Ch., and T. Fytterer	The 8-hour tide in the mesosphere and lower thermosphere over Collm (51.3°N; 13.0°E), 2004-2011, <i>Adv. Radio Sci.</i> , 10, 265-270.
	Jacobi, Ch	Long-term trends and decadal variability of upper mesosphere/lower thermosphere gravity waves at midlatitudes, Ber. Inst. Meteorol. Univ. Leipzig, 48, 25-33.
	Jacobi, Ch., and C. Arras	Enhanced sporadic E occurrence rates during the Geminid meteor showers 2006-2010, Ber. Inst. Meteorol. Univ. Leipzig, 48, 35-44.
	Jacobi, Ch	6 year mean prevailing winds and tides measured by VHF meteor radar over Collm (51.3°N, 13.0°E), <i>J. Atmos. Solar-Terr. Phys.</i> , 78–79, 8–18.
	Jacobi, Ch., P. Hoffmann, R.Q. Liu, E.G. Merzlyakov, Yu.I. Portnyagin, A.H. Manson, and C.E. Meek	Long-term trends, their changes, and interannual variability of Northern Hemisphere midlatitude MLT winds, <i>J. Atmos. Solar-Terr. Phys.</i> , 75-76, 81-91.
	Jäkel, E., M. <u>Wendisch</u> , and B. Mayer	Influence of spatial heterogeneity of local surface albedo on the area-averaged surface albedo retrieved from airborne irradiance measurements. <i>Atmos. Meas. Tech. Discuss.</i> , 5, 7457-7487, doi:10.5194/amtd-5-7457-2012, doi:10.5194/amtd-5-7457-2012. Accepted
	Müller,D., K.-H. Lee, J. Gasteiger, M. Tesche, B. Weinzierl, K. Kandler, T. Müller, C. Toledano, S. Otto, D. Althausen, and A. Ansmann	Comparison of optical and microphysical properties of pure Saharan mineral dust observed with AERONET Sun photometer, Raman lidar, and in situ instruments during SAMUM 2006, <i>J. Geophys. Res.</i> 117 (2012), D07211
	Nam, C. and J. Quaas	Evaluation of clouds and precipitation in the ECHAM5 general circulation model using CALIPSO and CloudSat, <i>J. Clim.</i> , 25, 4975–4992, doi 10.1175/JCLI-D-11-00347.1, 2012.
	Peters, K., P. Stier, J. Quaas, and H. Graßl	Aerosol indirect effects from shipping emissions: Sensitivity studies with the global aerosol-climate model ECHAM-HAM, <i>Atmos. Chem. Phys.</i> , 12, 5985–6007, doi 10.5194/acp-12-5985-2012, 2012.
	Quaas, J.	Evaluating the "critical relative humidity" as a measure of subgrid-scale variability of humidity in general circulation model cloud cover parameterizations using satellite data, <i>J. Geophys. Res.</i> , 117, D9, doi 10.1029/2012JD017495, 2012.
	Raabe, A. (ed.)	METTOOLS_VIII Tagungsband. Wiss. Mitteil Inst. f. Meteorol. Bd. 49, 156 S.
	Rennó, N. O., E. Williams, D. Rosenfeld, D. G. Fischer, J. Fischer, T. Kremic, A. Agrawal, M. O. Andreae, R. Bierbaum, R. Blakeslee, A. Boerner, N. Bowles, H.	CHASER: An Innovative Satellite Mission Concept to Measure the Effects of Aerosols on Clouds and Climate, <i>Bull. Am. Meteorol. Soc.</i> , 2012 (in press)

	Christian, J. Dunion, Á. Horváth, X. Huang, A. Khain, S. Kinne, M. C. Lemos, J. Penner, U. Pöschl, J. Quaas, E. Seran, B. Stevens, T. Walati, and T. Wagner	
	Schäfer, K., R. H. Grant, S. Emeis, A. Raabe, C. von der Heide, and H. P. Schmid	Areal-averaged trace gas emission rates from long-range open-path measurements in stable boundary layer conditions; <i>Atmos. Meas. Tech. Discuss.</i> , 5, 1571–1583, 2012
	Sanchez-Lorenzo, A., P. Laux, H.-J. Hendricks-Franssen, A. Georgoulias, J. Calbó, S. Vogl, and J. Quaas	Assessing large-scale weekly cycles in meteorological variables: a review, <i>Atmos. Chem. Phys.</i> , 12, 5755–5771, doi 10.5194/acp-12-5755-2012, 2012
	Schirber, S., D. Klocke, R. Pincus, J. Quaas, and J. Anderson,	Parameter estimation using data assimilation in an atmospheric general circulation model: From a perfect towards the real world, <i>J. Adv. Model. Earth Syst.</i> , p. in press, doi 10.1029/2012MS000167, 2012.
	Siebert, H., J. Bethke, E. Bierwirth, T. Conrath, K. Dieckmann, F. Ditas, A. Ehrlich, D. Farrell, S. Hartmann, M. A. Izaguirre, J. Katzwinkel, L. Nuijens, G. Roberts, M. Schäfer, R. A. Shaw, T. Schmeissner, I. Serikov, B. Stevens, F. Stratmann, B. Wehner, M. Wendisch, F. Werner, and H. Wex, 2012	The fine-scale structure of the trade wind cumuli over Barbados – an introduction to the CARRIBA project. <i>Atmos. Chem. Phys. Discuss.</i> , 12, 28609–28660.
	Stober, G., Ch. Jacobi, V. Matthias, P. Hoffmann, and M. Gerding	Neutral air density variations during strong planetary wave activity in the mesopause region derived from meteor radar observations, <i>J. Atmos. Sol.-Terr. Phys.</i> , 74, 55–63.
	Schönfeldt, H.-J.	Measuring saltation and creep with high spatial and temporal resolution, <i>Wiss. Mitteil Inst. f. Meteorol. Bd.</i> 50, 55–68
	Unglaub, C., Ch. Jacobi, G. Schmidtke, B. Nikutowski, and R. Brunner	Proxies to describe ionospheric variability and heating rates of the upper atmosphere: current progress, <i>Ber. Inst. Meteorol. Univ. Leipzig</i> , 48, 45–54.
	Unglaub, C., Ch. Jacobi, G. Schmidtke, B. Nikutowski, and R. Brunner	EUV-TEC proxy to describe ionospheric variability using satellite-borne solar EUV measurements, <i>Adv. Radio Sci.</i> , 10, 259–263.
	Unglaub, C., Ch. Jacobi, G. Schmidtke, B. Nikutowski, R. Brunner	Proxies to describe ionospheric variability and heating rates of the upper atmosphere: current progress, <i>Wiss. Mitteil Inst. f. Meteorol. Bd.</i> 50, 45–54
	Weber, T. and J. Quaas	Incorporating the subgrid-scale variability of clouds in the autoconversion parameterization, <i>J. Adv. Model. Earth Syst.</i> , (4), M11003, doi 10.1029/2012MS000156, 2012.
	Wendisch, M., and P. Yang,	Theory of Atmospheric Radiative Transfer – A Comprehensive Introduction. <i>Wiley-VCH Verlag GmbH & Co. KGaA, Weinheim, Germany</i> , 2012. ISBN: 978-3-527-40836-8.
	Werner, F., H. Siebert, P. Pilewskie, and M. Wendisch, 2012	Helicopter-borne passive remote sensing and collocated in situ observations of microphysical and optical properties of trade wind cumuli under overlying cirrus, Submitted to <i>J. Geophys. Res</i>
	Xu, X., A.H. Manson, C.E. Meek, D.M. Riggin, Ch. Jacobi, and J.R. Drummond	Mesospheric wind diurnal tides within the Canadian Middle Atmosphere Model Data Assimilation System, <i>J. Atmos. Sol.-Terr. Phys.</i> , 74, 24–43.
	Zhang, K., D. O'Donnell, J. Kazil, P. Stier, S. Kinne, U. Lohmann, S. Ferrachat, B. Croft, J. Quaas, H. Wan, S. Rast, and J. Feichter	The global aerosol-climate model ECHAM5-HAM, version 2: sensitivity to improvements in process representations, <i>Atmos. Chem. Phys.</i> , 12, 8911–8949, doi 10.5194/acp-12-8911-2012, 2012.
	Zygmuntowska, M., T. Mauritsen, J. Quaas, and L. Kaleschke	Artic clouds and surface radiation - a critical comparison of satellite retrievals and the ERA-INTERIM reanalysis, <i>Atmos. Chem. Phys.</i> , 12, 6667–6677, doi 10.5194/acp-12-6667-2012,

3. Wissenschaftliche und technische Mitarbeiter am LIM 2012

Name		E-Mail-Adresse
Barth	Manuela	mbarth@uni-leipzig.de
Bender	Michael	bender@gfz-potsdam.de
Bierwirth	Eike	eike.bierwirth@uni-leipzig.de
Brückner	Marlen	m.brueckner@uni-leipzig.de
Ehrlich	Andre	a.ehrlich@uni-leipzig.de
Feck-Yao	Wolfgang	feckyao@uni-leipzig.de
Finger	Fanny	fanny.finger@uni-leipzig.de
Fischer	Gabi	gfischer@rz.uni-leipzig.de
Fricke	Clemens	fricke@uni-leipzig.de
Hirsch	Kerstin	khirsch@uni-leipzig.de
Jacobi	Christoph	jacobi@rz.uni-leipzig.de
Jäkel	Evelin	e.jaekel@uni-leipzig.de
Kaiser	Falk	fkaiser@rz.uni-leipzig.de
Kundisch	Marcus	marcus.kundisch@studserv.uni-leipzig.de
Nikutowski	Bernd	bernd.nikutowski@ipm.fraunhofer.de
Pospichal	Bernhard	bernhard.pospichal@uni-leipzig.de
Quaas	Johannes	johannes.quaas@uni-leipzig.de
Raabe	Armin	raabe@uni-leipzig.de
Rehnert	Jutta	rehnert@uni-leipzig.de
Rosenow	Dagmar	d.rosenow@uni-leipzig.de
Salzmann	Marc	marc.salzmann@uni-leipzig.de
Schäfer	Michael	michael.schaefer@uni-leipzig.de
Schönfeldt	Hans-Jürgen	schoenfeldt@uni-leipzig.de
Staake	Karin	staake@uni-leipzig.de
Unglaub	Claudia	unglaub@uni-leipzig.de
Weiße	Frank	weisse@uni-leipzig.de
Wendisch	Manfred	m.wendisch@uni-leipzig.de
Werner	Frank	f.henrich@uni-leipzig.de
Wilsdorf	Michael	mwils@uni-leipzig.de

Immatrikulationen am Institut f. Meteorologie

Diplom Meteorologie													
Datum	Semester	1.FS	2. FS	3.FS	4.FS	5.FS	6. FS	7.FS	8.FS	9. FS	10.FS	>10.FS	Meteo_D
17.10.2012	WS 12/13											3	3
16.10.2011	WS 11/12											3	3
15.10.2010	WS 10/11											14	14
15.10.2009	WS 09/10								0	14	0	7	21
15.10.2008	WS 08/09						0	14	0	23	1	25	63
15.10.2007	WS 07/08			0	22	0	26	1	18	2	19	88	
13.12.2006	WS 06/07	0	40	0	36	0	24	2	14	1	17	175	
15.10.2005	WS 05/06	109	0	49	0	30	2	16	1	17	1	13	237
08.12.2004	WS 04/05	97	0	35	1	20	0	19	0	12	1	15	200
03.12.2003	WS 03/04	68	1	25	0	20	1	13	1	12	1	13	155
14.10.2002	WS 02/03	45	0	19	0	16	0	15	1	12	1	9	118
06.12.2001	WS 01/02	43	0	21	0	16	0	13	0	7	0	5	105
07.12.2000	WS 00/01	41	1	27	0	22	0	8	0	6	1	6	112
01.12.1999	WS 99/00	40	0	24	0	9	0	9	0	6	1	6	95
16.12.1998	WS 98/99	36	0	11	0	17	1	9	1	5	0	8	88
10.11.1997	WS 97/98	29	0	17	0	10	1	8	0	7	0	4	76

BSC Meteorologie													
Datum	Semester	1.FS	2. FS	3.FS	4.FS	5.FS	6. FS	7.FS	8.FS	9. FS	10.FS	>10.FS	Meteo_BSC
Datum	Semester	BSC_FSI	BSC_FSI	BSC_FS3	BSC_FS4	BSC_FS5	BSC_FS6	BSC_FS7	BSC_FS8	BSC_FS9			Meteo_BSC
15.10.2012	WS 12/13	60		29	1	22	2	16	1	2			133
15.10.2011	WS 11/12	60		27		26	1	19		1			134
15.10.2010	WS 10/11	64		34		20							118
15.10.2009	WS 09/10	67	0	21	0	20	0						108
15.10.2008	WS 08/09	71	0	28	0	12							111
15.10.2007	WS 07/08	98	0	15									113
13.12.2006	WS 06/07	31											31
15.10.2005	WS 05/06												0

MSC Meteorologie													
Datum	Semester	1.FS	2. FS	3.FS	4.FS	5.FS	6. FS						
Datum	Semester	MSC_FSI	MSC_FSI	MSC_FS3	MSC_FS4	>MSC_FS5							
15.10.2012	WS 12/13	18		20	1	15							54
15.10.2011	WS 11/12	21		17			10						48
15.10.2010	WS 10/11	20		9			5						34
15.10.2009	WS 09/10	11											11
15.10.2008	WS 08/09												0
15.10.2007	WS 07/08												0
13.12.2006	WS 06/07												0

4. Abschlussarbeiten Institut für Meteorologie 2012

Promotionen

Sebastian Otto

Optische Eigenschaften nichtkugelförmiger Saharamineralstaubpartikel und deren Einfluss auf den Strahlungstransport in der Erdatmosphäre

Holger Baars

Aerosol profiling with lidar in the Amazon Basin during the wet and dry season 2008

Katrin Dieckmann (geb. Mildenberger)

Hygroscopic Growth and Activation Measurements of Aerosol Particles in Lab and Field

Dennis Niedermeier

Heterogeneous ice nucleation in droplets containing mineral dust particles: An experimental and theoretical study

MSC-Abschlüsse 2012

Augustin, Stefanie	Immersionsgefrierverhalten biologischer Partikel am Leipzig Aerosol Cloud Interaction Simulator (LACIS)
Bley, Sebastian	Vergleich zweier Schwellwertalgorithmen zur Wolkendetektion in solaren METEOSAT SEVIRI Bildern und Anwendung auf den hochauflösten sichtbaren Kanal
Fischer, Stephan	WRF-Simulation zur Quantifizierung der Invarianzeigenschaften der Ertel'schen potentiellen Vortizität während der Entwicklung einer Zyklone bei einer Vb Wetterlage
Foth, Andreas	Bestimmung der vertikalen Aerosolverteilung über Punta Arenas, Chile (53.2°S, 70.9°W)
Fytterer, Tilo	Analyse solarer Gezeiten und sporadischer E-Schichten
Heyner, Frank	Bestimmung der räumlich aufgelösten optischen Dicke von inhomogenen Zirren durch Messungen mit einem abbildenden Spektrometer
Hoff, Michael	Ein Laborexperiment für meteorologische Anwendungen: Optimale Störungen für reguläre und irreguläre barokline Strömungen
Höpner, Friederike	Messung des hygrokopischen Wachstums von submikronen Aerosolpartikeln in der marinen Grenzschicht des Atlantischen Ozeans
Junghänel, Thomas	Konzeptuelle Grundlagen einer Hagelklimatologie für den Freistaat Sachsen
Oelsner, Peter	Aufbau eines High-Spectral-Resolution-Kanals und Vergleich mit dem Raman-Kanal eines Aerosol-Lidars
Pfitzenmaier, Lukas	Determination of microphysical properties of cloud and drizzle droplets based on observations with radar, microwave radiometer, and lidar
Wagner, Janet	Microphysical aerosol properties retrieved from combined lidar and sun photometer measurements
Wenzel, Julia	Optische Eigenschaften des Aerosols in der atlantischen maritimen Grenzschicht. Ein Querschnitt von Kapstadt bis Bremerhaven
Wolf, Veronika	Überblick über 5 Jahre schiffsgebundener Fernerkundungsbeobachtungen der Atmosphäre über dem Atlantischen Ozean

BSC-Abschlüsse 2012

Name / Vorname	Thema
Bär, Jewgenia	Charakterisierung der synoptischen Situation während der Meskampagne VERD1 (April / Mai 2012)
Bechler, Josephine	Entwicklung eines agrarmeteorologischen Wachstumsindex als Baustein zur Abschätzung von Ertragsrisiken in der pflanzlichen Erzeugung
Düsing, Sebastian	Beschreibung des ionosphärischen Elektronengehalts mit EUV-Indizes
Grawe, Sarah	Häufigkeitsverteilung von Cirrus-Wolken über der Nordsee
Hellner, Lisa	Indirektes CO ₂ -Forcing im Multi-Modell-Ensemble des CMIP5
Hertel, Daniel	Auswertung von Zeitreihen verschiedener Klimaszenarien - Schneemengen im Großraum Sachsen
Hoffmann, Erik	Troposphärische Multiphasen-Halogenchemie in Küstengebieten
Kilian, Philipp	Vertikale Verteilung des Flüssigwassers in Wolken
Kühne, Philipp	Robuste Strukturen in Klima-Wolken-Feedbacks im Multi-Model-Ensemble des CMIP5
Luttkus, Marie Luise	Parametrisierung von biogenen Emissionen in atmosphärischen Chemie-Transport-Modellen
Rau, Andrea	Bestimmung kurzketiger Dicarbonsäuren in troposphärischen Partikeln
Särchinger, Martin	Relevanz der Topographie auf den Strahlungstransport in der Ätna-Region
Szodry, Kai-Erik	Analyse des Einflusses der Änderung der Wolkentropfenanzahlkonzentration auf die planetare Albedo
Thalheim, Christoph	Vergleich von alter und neuer LIM Wetterstation
Wagner, Robert	Prognosegüte der Wind- und Solarstromerzeugung am Beispiel ausgewählter Wind- und Solarparks in Norddeutschland
Walther, Jonas	Fernerkundung von Wolkeneigenschaften bei Verwendung zweier separater Spektrometer

**Wissenschaftliche Mitteilungen aus dem Institut für Meteorologie der
Universität Leipzig**

- Band 1 *A. Raabe, G. Tetzlaff und W. Metz* (Edn.), 1995: Meteorologische Arbeiten aus Leipzig I
- Band 2 *R. Devantier*, 1995: Wolkenbildungsprozesse über der südwestlichen Ostsee - Anwendungen eines neuen Wolkenschemas in einem mesoskaligen Modell
- Band 3 *J. Laubach*, 1996: Charakterisierung des turbulenten Austausches von Wärme, Wasserdampf und Kohlendioxid über niedriger Vegetation anhand von Eddy-Korrelations-Messungen
- Band 4 *A. Raabe und J. Heintzenberg* (Edn.), 1996: Meteorologische Arbeiten aus Leipzig II
- Band 5 Wind- und Seegangsatlas für das Gebiet um Darß und Zingst
- Band 6 *D. Hinneburg, A. Raabe und G. Tetzlaff*, 1997: Teil I: Windatlas
W. von Hoyningen-Huene und G. Tetzlaff (Edn.), 1997: Sediment and Aerosol
Teil I: Beiträge zur Alfred-Wegener-Konferenz, Leipzig 1997
Teil II: Aktuelle Beiträge aus dem Institut für Meteorologie
- Band 7 *B.-R. Beckmann*, 1997: Veränderungen in der Windklimatologie und in der Häufigkeit von Sturmhochwassern an der Ostseeküste Mecklenburg-Vorpommerns
- Band 8 *P. Posse*, 1997: Bestimmung klimarelevanter Parameter des maritimen Aerosols unter besonderer Berücksichtigung der Nichtkugelform realer Aerosolteilchen
- Band 9 *A. Raabe, K. Arnold und J. Heintzenberg* (Edn.), 1998: Meteorologische Arbeiten aus Leipzig III
- Band 10 Wind- und Seegangsatlas für das Gebiet um Darß und Zingst, Teil II, 1998:
D. Hinneburg, A. Raabe und G. Tetzlaff: Vergleich Windatlas –Beobachtungsdaten; *M. Börngen, H.-J. Schönfeldt, R. Riechmann, G. Panin und G. Tetzlaff*: Seegangsatlas; *M. Stephan und H.-J. Schönfeldt*: Sedimenttransportatlas
- Band 11** ***J. Rissmann, 1998:*** Der Einfluss langwelliger Strahlungsprozesse auf das bodennahe Temperaturprofil
- Band 12 *A. Raabe, K. Arnold und J. Heintzenberg* (Edn.), 1999: Meteorologische Arbeiten aus Leipzig IV
- Band 13 *U. Müller, W. Kuttler und G. Tetzlaff* (Edn.), 1999: Workshop Stadtclima 17. / 18. 02. 1999 in Leipzig
- Band 14 *R. Surkow*, 1999: Optimierung der Leistungsverfügbarkeit von Windenergie durch ihre Integration in Wind-Biogas-Hybridanlagen
- Band 15 *N. Mölders*, 1999: Einfache und akkumulierte Landnutzungsänderungen und ihre Auswirkungen auf Evapotranspiration, Wolken- und Niederschlagsbildung
- Band 16 *G. Tetzlaff und U. Grünwald* (Edn.), 1999:
2. Tagung des Fachausschusses Hydrometeorologie 15./16. 11. 1999 in Leipzig
- Band 17 *A. Raabe und K. Arnold* (Edn.), 2000: Meteorologische Arbeiten aus Leipzig V
- Band 18 *K. Arnold*, 2000: Ein experimentelles Verfahren zur Akustischen Tomographie im Bereich der atmosphärischen Grenzschicht
- Band 19 *A. Ziemann*, 2000: Eine theoretische Studie zur akustischen Tomographie in der atmosphärischen Grenzschicht
- Band 20 *Ch. Jacobi*, 2000: Midlatitude mesopause region dynamics and its coupling with lower and middle atmospheric processes
- Band 21 *M. Klingspohn*, 2000: Interdekadische Klimavariabilität über dem Nordatlantik – Statistische Analysen und Modellstudien –
- Band 22 *A. Raabe und K. Arnold* (Edn.), 2001: Meteorologische Arbeiten aus Leipzig VI
- Band 23 *K. Arnold, A. Ziemann, G. Tetzlaff, V. Mellert und A. Raabe* (Edn.), 2001: International Workshop Tomography and Acoustics: Recent developments and methods 06. - 07.03.2001 in Leipzig
- Band 24 *O. Fanenbruck*, 2001: Ein thermophysiolgisches Bewertungsmodell mit Anwendung auf das Leipziger Stadtgebiet
- Band 25 *M. Lange*, 2001: Modellstudien zum CO₂-Anstieg und O₃-Abbau in der mittleren Atmosphäre und Einfluß des Polarwirbels auf die zonale Symmetrie des Windfeldes in der Mesopausenregion
- Band 26 *A. Raabe und K. Arnold* (Edn.), 2002: Meteorologische Arbeiten aus Leipzig VII
- Band 27 *M. Simmel*, 2002: Ein Modul zur spektralen Beschreibung von Wolken und Niederschlag in einem Mesoskalenmodell zur Verwendung auf Parallelrechnern

- Band 28 *H. Siebert*, 2002: Tethered-Balloon Borne Turbulence Measurements in the Cloudy Boundary Layer
- Sonderband *G. Tetzlaff* (Hrsg.), 2002: Atmosphäre - Aktuelle Beiträge zu Luft, Ozon, Sturm, Starkregen und Klima
- Band 29 *U. Harlander*, 2003: On Rossby wave propagation in atmosphere and ocean
- Band 30 *A. Raabe und K. Arnold* (Edn.), 2003: Meteorologische Arbeiten aus Leipzig VIII
- Band 31 *M. Wendisch*, 2003: Absorption of Solar Radiation in the Cloudless and Cloudy Atmosphere
- Band 32 *U. Schlink*, 2003: Longitudinal Models in Biometeorology: Effect Assessment and Forecasting of Ground-level Ozone
- Band 33 *H. Heinrich*, 2004: Finite barotrope Instabilität unter synoptischem Antrieb
- Band 34 *A. Raabe und K. Arnold* (Edn.), 2004: Meteorologische Arbeiten aus Leipzig IX
- Band 35 *C. Stolle*, 2004: Three-dimensional imaging of ionospheric electron density fields using GPS observations at the ground and onboard the CHAMP satellite
- Band 36 *A. Raabe und K. Arnold* (Edn.), 2005: Meteorologische Arbeiten (X) und Jahresbericht 2004 des Institutes für Meteorologie der Universität Leipzig
- Band 37 *A. Raabe und K. Arnold* (Edn.), 2006: Meteorologische Arbeiten (XI) und Jahresbericht 2005 des Institutes für Meteorologie der Universität Leipzig
- Band 38 *K. Fröhlich*, 2006: The Quasi Two-Day Wave – its impact on zonal mean circulation and wave-wave interactions in the middle atmosphere
- Band 39 *K. Radtke*, 2006: Zur Sensitivität von Starkwindfeldern gegenüber verschiedenen meteorologischen Parametern im Mesoskalenmodell LM
- Band 40 *K. Hungershöfer*, 2007: Optical Properties of Aerosol Particles and Radiative Transfer in Connection with Biomass Burning
- Band 41 *A. Raabe* (Hrsg.), 2007: Meteorologische Arbeiten (XII) und Jahresbericht 2006 des Institutes für Meteorologie der Universität Leipzig
- Band 42 *A. Raabe* (Hrsg.), 2008: Meteorologische Arbeiten (XIII) und Jahresbericht 2007 des Institutes für Meteorologie der Universität Leipzig
- Band 43 *A. Kniffka*, 2008: Einfluss der Inhomogenitäten von Aerosol, Bodenalbedo und Wolken auf das aktinische Strahlungsfeld der Atmosphäre
- Band 44 *M. Barth*, 2009: Akustische Tomographie zur zeitgleichen Erfassung von Temperatur- und Strömungsfeldern
- Band 45 *A. Raabe* (Hrsg.), 2009: Meteorologische Arbeiten (XIV) und Jahresbericht 2008 des Institutes für Meteorologie der Universität Leipzig
- Band 46 *G. Stober*, 2009: Astrophysical Studies on Meteors using a SKiYMET All-Sky Meteor Radar
- Band 47 *A. Raabe* (Hrsg.), 2010: Meteorologische Arbeiten (XV) und Jahresbericht 2009 des Institutes für Meteorologie der Universität Leipzig
- Band 48 *A. Raabe* (Hrsg.), 2011: Meteorologische Arbeiten (XVI) und Jahresbericht 2010 des Institutes für Meteorologie der Universität Leipzig
- Band 49 *A. Raabe* (Hrsg.), 2012: METTOOLS_VIII Tagungsband
- Band 50 *A. Raabe* (Hrsg.), 2012: Meteorologische Arbeiten (XVII) und Jahresbericht 2011 des Institutes für Meteorologie der Universität Leipzig
- Band 51 *A. Raabe* (Hrsg.), 2013: Meteorologische Arbeiten (XVIII) und Jahresbericht 2012 des Institutes für Meteorologie der Universität Leipzig